2022

PERMEABILITY, STRUCTURAL CHANGES, FLOW REGIME TRANSITIONS IN FUEL CELL CATALYST LAYERS AND A MODEL FOR PREDICTING TRAPPED SATURATION FOR TWO-PHASE FLOW IN POROUS MEDIA

Karrar Takleef Alofari
Michigan Technological University, ktalofar@mtu.edu

PERMEABILITY, STRUCTURAL CHANGES, FLOW REGIME TRANSITIONS IN FUEL CELL CATALYST LAYERS AND A MODEL FOR PREDICTING TRAPPED SATURATION FOR TWO-PHASE FLOW IN POROUS MEDIA

By

Karrar T. Alofari

A DISSERTATION

Submitted in partial fulfillment of the requirements for the degree of

DOCTOR OF PHILOSOPHY

In Mechanical Engineering-Engineering Mechanics

MICHIGAN TECHNOLOGICAL UNIVERSITY

2022

This dissertation has been approved in partial fulfillment of the requirements for the Degree of DOCTOR OF PHILOSOPHY in Mechanical Engineering-Engineering Mechanics.

Department of Mechanical Engineering – Engineering Mechanics

Dissertation Co-advisor: *Dr. Jeffrey S. Allen*

Dissertation Co-advisor: *Dr. Ezequiel F. Médici*

Committee Member: *Dr. Kazuya M. Tajiri*

Committee Member: *Dr. Aimy Bazylak*

Committee Member: *Dr. Sajjad Bigham*

Department Chair: *Dr. William W. Predebon*

Dedication

To my parents, who always believing in me, supporting me; their prayers that help me survive during difficult times.

To my brothers who are supportive and encouraging in any step in my life.

To my family: My wife, for her patience, support and encouragement. You are the one who has made this journey so much easier, enjoyable and memorable. My son "Ahmed" and my daughters "Amenah" and "Narjis" who motivate me, and make me stronger. I love you to the Mars and back.

Contents

List of Figures

List of Tables

Preface

Scholarly contributions are as follows:

A peer-reviewed conference proceeding papers.

- † Using Fractional Flow Function to Extrapolate Trapped Saturation in Two-Phase Flow in Porous Media, ICOGPC, Ottawa, Canada, 28th - 29th January, 2022.
- † Ionomer Films Impact on The Structure, Flow Regime, and The Wettability of The Catalyst Layer of PEMFC, European Fuel Cells and Hydrogen 2021, December 15-17.
- † Percolation Behavior in Catalytic Porous Material, ECS Transactions, 92 (8) 71-76 (2019).

A peer-reviewed journal papers.

- † Capillary Penetration Method for Measuring Wetting Properties of Carbon Ionomer Films for Proton Exchange Membrane Fuel Cell (PEMFC). Applications, J. Electrochemical Soc., 166 (7) F3227-F3233 (2019). (co-author)
- † Ex-Situ Examination of Mass Transport Resistance in a Fuel Cell Catalyst Layer (will be submitted to Journal of Electrochemical Society).
- † Structure and Wettability of Catalyst Layer of PEMFC (will be submitted to Journal of Hydrogen and Energy).
- † Computationally Efficient Model to Calculate Trapped Saturations in Porous Materials (will be submitted to Journal of Transport in Porous Media).

Other Contributions:

- † A New Method to Predict Trapped Saturation and Pressure Drop in Two-Phase Flow in Low-Gravity Packed Beds Based on PBRE ISS Data, NASA Proposal submitted for NASA Early Stage Innovations (ESI) NRA (NNH20ZDA014N), 1/2022.

† Dispersed Nanostructured Thin Film (dNSTF) Catalyst, Album of Porous Media, Inaugural collection of imaging/visualization techniques applied to porous media. Album is sponsored by the International Society of Porous Media as part of the 2021 INTERPORE conference.

Acknowledgments

Praise be to Allah, the Most Gracious, the Most Merciful.

First, I would like to thank my advisor Prof. Jeffrey S. Allen. With all the effort that has been put into this dissertation, its completion would not have been possible without his unlimited support, patience and guidance. It has been a great opportunity to work with him, and a pleasure to be part of his research team.

I would like also to thank my co-advisor Dr. Ezequeil F. Médici for his support and patience. His guidance was so helpful at the earlier stages of this research.

I would like to thank Prof. Kazuya Tajiri for all the help that he provided, his door was always open for any question.

Special Thanks to my friends and colleagues: Dr. Vinaykumar Konduru, Dr. Fei Long, Behrouz Khoshbakht, Dr. Behdad Afkhami, Rachel Store, Dr. Anjana Asthana, and others for their help, support and advice in various stages.

I would like to acknowledge the support from the Higher Committee of Education Development in Iraq (HCED) for providing the financial support for my study (Thanks to all staff administering the award), the Department of Energy, Office of Energy Efficiency and Renewable Energy (EERE) under award number DE-EE0007650, the Department of Mechanical Engineering-Engineering Mechanics at Michigan Tech, and funds from the John F. and Joan M. Calder Professorship. Finally, I would like to thank Dr. Andrew Haug for supplying the test samples and Dr. Kevin Cooper of Scribner Associates, Inc. for providing a gas humidifier for sample conditioning.

List of Abbreviations

PEMFC	Proton Exchange Membrane Fuel Cell
CL	Catalyst Layer
RH	Relative Humidity
FFT	Fractional Flow Theory
NSTF	Nano Structure Thin Film
dNSTF	Dispersed Nano Structure Thin Films
SEM	Scanning Electron Microscopy
TEM	Transition Electron Microscopy
STEM	Scanning-Transition Electron Microscopy
BF	Bright Field
HAADF	High Angle Annular Dark Field
EDX	Energy-Dispersive X-ray
I/C	Ionomer Weight to Carbon Ratio
Wh/C	Whisker to Carbon Ratio
EW	Equivalent Weight
PTL	Porous Transport Layer
HOR	Hydrogen Oxidation Reaction
ORR	Oxygen Reduction Reaction
GDL	Gas Diffusion Layer
CCM	Catalyst Coated Membrane
CCD	Charge-Coupled Device
PMMA	Polyethylmethacrylate
PTFE	PolyTetraFluoroEthylene
BOP	Beginning-of-Percolation
EOP	End-of-Percolation
CA	Contact Angle
PEM	Proton Exchange Membrane
NALP	Non-Aqueous Liquid Phase

Abstract

Proper water management in Proton Exchange Membrane (PEM) fuel cell is important to achieve high performance. Understanding the percolation of the produced water at the cathode catalyst layer (CL) is critical for any robust water management technique. In this study, an ex-situ experimental setup is used to study percolation in the CL at different injection rates and relative humidity (RH) conditions. The results show that increasing the flow rate force the liquid to flow through the bulk of the pores due to the dominant viscous effect. On the other hand, at low injection rates, the capillary becomes dominant and liquid flow along the roughness of pores surfaces. At low flow rates, a big wetted area is captured, compared to high flow rates tests, but the liquid saturation is lower. Another set of testing was done at a fixed flow rate and a varied RH conditions, where permeability is calculated based on the steady percolation pressure. The permeability of the CL for both gas and liquid decreases as RH increases, and that more likely related to ionomer swelling. A correlation between the permeability and water content is derived. A sharp decrease in the permeability is observed at low water content ($\lambda < 3$), beyond that there are no significant changes. Moreover, low and high RH condition shows a significant effects on the structure of CL and flow regime. Static contact angle measurements at a range of RH also indicate possible morphological changes in the CL.

In addition, fractional flow theory (FFT) model is adapted to study immiscible displacement of two-phase flow in a porous medium. The resulting model accurately predicts trapped saturation that occurs during imbibition and drainage of incompressible fluids for any capillary number. It also accurately predicts the fluid-fluid front displacement and critical capillary number at which trapped saturation begins to decrease. The unique aspect of this model is incorporation of a scaling factor, suggested by Médici and Allen [12], that captures the propensity for gas or liquid holdup for any porous media and fluid pair.

Chapter 1

Introduction

Immiscible displacement in porous media is found in applications such as oil recovery [13, 14], subsurface and groundwater contamination [15–17], water management in proton exchange membrane (PEM) fuel cell [18, 19], multiphase flow in packed bed reactor under normal and low gravity [20, 21], and many other applications. During the immiscible displacement, different forces exist. At the pore level, a force at the fluid-fluid interface is the capillary force [22]. Viscous effect is another force that is a measure of the resistance to flow. At a low flow rate, capillarity becomes dominant and part of the displaced fluid may remain trapped in the porous media due to preferential percolation path of the injected phase [23–25], while at high flow rates viscous effects are dominant and the injected fluid invades most of the pores.

A Proton Exchange Membrane (PEM) fuel cell is an electrochemical device in which hydrogen and oxygen react to produce electricity, water, and heat. A fuel cell consists of an anode and cathode separated by PEM. The anode and cathode are thin porous

materials, a few microns in thickness consisting of carbon supports where platinum dispersed and thin ionomer films. The chemical structure of ionomer films consists of an ionic domain of a hydrophilic sulfonic acid group, which is connected by a side chain to a hydrophobic fluorocarbon backbone. The ionic domains in the ionomer retain water and swell and that adds complexity to the structure and morphology of the catalyst layer.

Water presence in the catalyst layer has a double rule. It is necessary to hydrate ionomer films in the catalyst layer and PEM, and that increases proton conductivity. On the other hand, an excessive amount of water as vapor or liquid results in high resistance to mass transport [26–28]. This is could be related to the reduction in the mean pore size of the catalyst layer due to ionomer swelling, which decreases as the relative humidity (RH) increases [4, 29], or the presence of liquid water (trapped) preventing the reactants to reach the reaction sites. Moreover, the absorption/release of water to/from ionomer films due to RH cycling leads to structural stresses and potential defect growth [30]. As the ionomer films interact with vapor this alters the orientation of sulfonic acid side chains [31, 32], and that could change the wettability of the catalyst layer.

1.1 Outline

The scope of the dissertation starts with a general introduction related to the porous media and two-phase flow. Then, the experimental part includes SEM and TEM

imaging for fuel cell catalyst layers (CL), adapting a Hele-Shaw setup to study two-phase flow in a thin porous media, and a sessile drop method to measure the wettability on the surface. Then, fractional flow theory (FFT) is revised and used to calculate trapped saturation in two-phase flow in porous media. The dissertation ends with a conclusion and recommendations.

The main focus of this research was to study liquid/gas transport in the catalyst layer of PEM fuel cell. Proper water management at the cathode side is crucial to hold the performance at an acceptable level in the fuel cell. Mass transport in a CL is not well understood, due to the complex structure of the CL and the swelling of ionomer as RH is varied. Therefore, a Hele-Shaw setup was adapted to study the liquid/gas transport in the CL at a range of flow rates and RH conditions. The sessile drop method is used to characterize the wettability of the CL at a range of RH conditions.

In addition, the FFT model was developed by including the viscous and capillary effects in the formulation. The capillary term is simplified using a unique length scale [12], which results in a model that can be used to calculate trapped saturation for any two-phase flow and porous medium.

The research parts are elaborated in seven chapters as follows:

Chapter 1: Introduction: The motivations and the objectives of the project are listed.

Chapter 2: Porous Media Properties and Concepts: A general introduction to defining the properties and concepts related to the porous media.

Chapter 3: Catalyst Layer Structure: This chapter studies the structure and morphology of the catalyst layer using SEM and TEM in conjunction with

EDX.

Chapter 4: Ex-Situ Examination of Mass Transport Resistance in a Fuel Cell Catalyst Layer: Using the Hele-Shaw setup to characterize the permeability of Catalyst Layer.

Chapter 5: Ionomer Impact on Structure and Wettability of PEM Fuel Cell Catalyst Layer: Using the sessile drop method together with the Hele-Shaw setup to study the structure and wettability of the catalyst layer.

Chapter 6: Computationally Efficient Model to Calculate Trapped Saturation in Porous Materials: This chapter details the FFT model and how to use it to study and estimate trapped saturation of two-phase flow in porous media.

Chapter 7: Conclusion and Recommendations: Includes the conclusion, contribution and future work.

Chapter 2

Porous Media Properties and Concepts

A porous medium can be defined as a solid matrix with voids of interconnected pores in a regular or random manner that enables fluid flow [25]. The porous media can be as big as a petroleum reservoir, or as small as a catalyst layer ($< 15\mu$m) of proton exchange membrane fuel cell [33]. This study focused on immiscible displacement of fluids in porous media which are found in many applications, such as oil recovery [25, 34] and water management in proton exchange membrane fuel cell [27, 35, 36]. The displacement process in porous media encounters a direct contact between fluids and the pore surface, which leads to unique interactions defined by many concepts that can be affected by different properties. Therefore, it is necessary to introduce these properties and concepts before starting with the details of this study.

2.1 Porous Media Properties

There are many properties that are used to characterize porous media. In this study, porous media properties are divided into morphological properties and dynamic property (permeability).

2.1.1 Morphological Properties

An important property used to describe a porous medium is porosity, which refers to the total pore space that can store or conduct fluids. Porosity is defined as the ratio of the pore volume to the bulk volume [25].

$$\varepsilon = \frac{\text{pore volume}}{\text{bulk volume}} \tag{2.1}$$

The pores in porous media can be classified into three types: interconnected pores, dead-end pores and isolated (closed) pores in Figure 2.1. Interconnected pores have the essential contribution to the liquid movements throughout the porous media. A porous medium could have a high porosity, but low conductivity to fluids due to insufficient inter-connectivity. If considering only interconnected pores that can be occupied by mobile fluids, then equation 2.1 is the effective porosity. Porous media consist of three volumes, bulk volume, solid volume and pore volume, where the porosity can be estimated by determining any two of these three volumes [24].

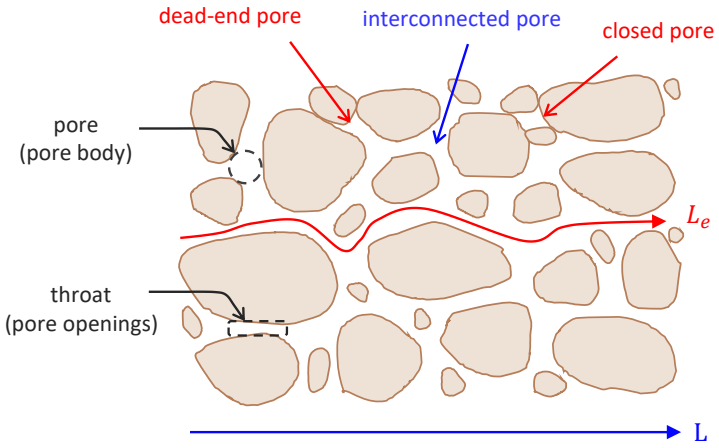

Figure 2.1: A general sketch of a porous medium.

Another important property is the tortuosity, which is defined as the ratio of the average flow path length (L_e) to the length of the porous medium (L) as shown in Figure 2.1 [37]. Tortuosity is used to adjust and correct the calculated permeability and obtain a good agreement with experimental data [38, 39].

$$\tau = \frac{L_e}{L} \tag{2.2}$$

Changes in the radius of a pore is another factor that affects the permeability of a porous medium which is known as the constrictivity. This is the ratio between the maximum and minimum cross section areas of a pore [40].

$$\delta = \frac{A_{\text{pore}} \times A_{\text{throat}}}{\frac{1}{2}(A_{\text{pore}} + A_{\text{throat}})} \tag{2.3}$$

Pore size distribution is another factor that characterizes the porous media with

more details than the porosity in terms of classifying the pore sizes (big, medium and small). Estimating pore size distribution is important for consolidated porous material, since grain size distribution can not be obtained. A popular method to measure the pore size distribution is the mercury intrusion porosimetry, nevertheless, many other measurements techniques can be used, such as photomicrography [41] or x-ray computed tomography [42]. Pore size distribution gives information about the relative abundance of each pore [43]. The first moment of this distribution is the mean pore size [41]. Pore size distribution indicates the complexity of the structure, where it can relates pore sizes to the particle sizes, for example, large pores are associated to large particles. An important feature of the pore size distribution is the significance to affect the porous media efficiency to transmit fluids [44], which make it an important parameter to characterize any porous media.

2.1.2 Permeability

Permeability is the ability of a porous media to allow fluids to pass through. It is a dynamic property that is characterized by flow experiments [45]. There is a parallel relationship between permeability and porosity, where increases in porosity generally increases the permeability. Other morphological parameters, like tortuosity, constrictivity, and pore size distribution can also have a significant effect on the permeability. Thus, permeability is an important property for any porous media. Permeability can be determined in uni-directional or radial flow using the Darcy form of conservation of momentum. For uni-directional flow, a Darcy formulation is written as:

$$q = -\frac{\kappa\, A}{\mu}\frac{\Delta P}{\Delta x} \tag{2.4}$$

where q is the flow rate, κ is the permeability, A is the corss section area, μ is the viscosity of the fluid, and $\Delta P/\Delta x$ is the pressure drop. The unit of the permeability is the Darcy (D). A $1\,cm^3/s$ flow rate with a viscosity of $1\,cP$ producing a pressure drop of $1\,atm$ through a cubic porous material of $1\,cm$ side length, has a permeability is $1\,Darcy$. The conversion of $1\,Darcy$ to m^2 is:

$$1\,Darcy = \frac{1\,\frac{cm^3}{s}\,.\,1\,cP(10^{-7}\frac{N}{cm^2}s)}{1\,cm^2\,.\,\frac{1\,atm}{1\,cm}(10.132\frac{N/cm^2}{atm})} = 9.8697\cdot 10^{-9}\,m^2 \tag{2.5}$$

Equations are derived to relate permeability to various physical properties of a porous medium, such as porosity and average particle or fiber diameter [46, 47]. The Kozeny-Carman equation is a method to estimate permeability from the pressure drop of fluid across a packed bed under laminar flow conditions [37].

$$-\frac{\Delta P}{L} = \frac{9\,b\,\mu\,q''}{4\,D_p^2}\,\frac{(1-\varepsilon)^2}{\varepsilon^3}\left(\frac{L_e}{L}\right)^2 \tag{2.6}$$

where b is the capillary shape factor, and D_p is the average diameter of the particles. The values of b and L_e/L are taken to be 40 and $\sqrt{2}$ [37, 48], respectively, and equation 2.6 becomes:

$$-\frac{\Delta P}{L} = \frac{180\,\mu\,q''}{4\,D_p^2}\,\frac{(1-\varepsilon)^2}{\varepsilon^3} \tag{2.7}$$

Based on experimental results, Ergun and Orning [20] suggested 150 instead of 180. Combining equations 2.4 and 2.7 gives an estimate of absolute permeability based on particle diameter and porosity for uni-directional flow [49].

$$\kappa = \frac{D_p^2}{180} \frac{\varepsilon^3}{(1-\varepsilon^2)} \tag{2.8}$$

In case of radial flow, Darcy's equation can be written as:

$$q = -\frac{\kappa A}{\mu} \frac{dP}{dr} \tag{2.9}$$

For a constant injection rate, q, through a cross section area, $A = 2\pi rh$. Integrating between $(r_1 - r_2)$ with respect to $(P_1 - P_2)$ gives [24]:

$$q = -\frac{2\,\pi\,h\,\kappa}{\mu\,ln(r_2/r_1)}(\Delta P) \tag{2.10}$$

where r_1 and r_2 are the inner and outer radius of the sample at which the pressures, P_1 and P_2 are measured, respectively, and h is the thickness of the porous medium.

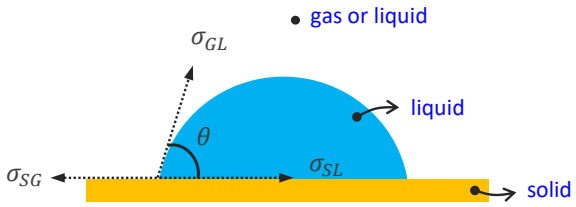

Figure 2.2: Forces at the fluid-fluid-solid interface and the contact angle.

2.2 Surface Tension, Wettability, and Capillary Pressure

In immiscible fluid displacement, the existence of the forces at the fluid-fluid-solid interfaces gives rise to what is known as surface tension. Figure 2.2 shows a drop of a liquid and the forces at the interfaces are combined in equation 2.11, which is known as Young's equation. σ_{LG}, σ_{SL} and σ_{SG} are the interfacial forces at the liquid-gas, solid-liquid, and solid-gas, respectively. θ is the contact angle, which is a macroscopic manifestation of microscopic forces. θ is used to characterize the wettability of a fluid. If θ is greater than 90° then the surface is characterized as a nonwetting surface. For $\theta < 90°$, it is a wetting surface.

$$\cos(\theta)\,\sigma_{LG} + \sigma_{SL} - \sigma SG \tag{2.11}$$

Due to surface tension and interface curvature a pressure difference can exist at the fluid-fluid interface. The pressure difference is known as the capillary pressure. Capillary rise is an example to illustrate the capillary pressure as shown in Figure 2.3. Capillary pressure is influenced by surface tension, wettability, and the size of

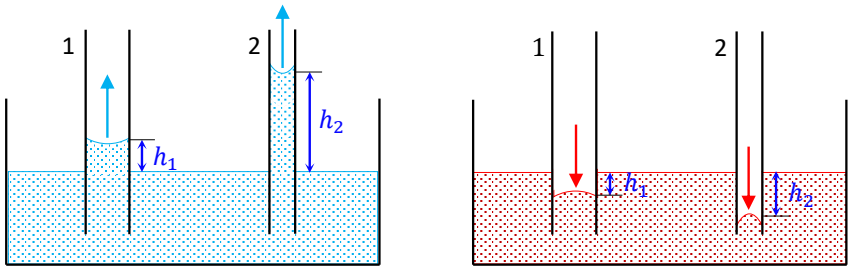

(a) Wetting Liquid (b) Non-wettign Liquid

Figure 2.3: The effect of tube size and fluid wettability on the head and the direction of the capillary pressure respectively.

the capillary tube, which are combined in what is known as Young-Laplace equation.

$$P_g - P_l = P_c = \frac{2\,\sigma\,cos(\theta)}{r} \tag{2.12}$$

where P_g is the gas pressure, P_l is the liquid pressure, P_c is the capillary pressure, σ is the surface tension, r is the pore radius. The combination of fluid-fluid-solid could result in a wetting (as in Figure 2.3(a)) or non-wetting (as in Figure 2.3(b)) configuration, where the capillary action tries to raise or suppress the liquid inside the tube, respectively. The capillary pressure is related to the height (h) as $P_c = \rho\,g\,h$, then equation 2.12 becomes,

$$h = \frac{2\,\sigma\,cos(\theta)}{r\,\rho\,g} \tag{2.13}$$

where g is the gravitational constant and ρ is the density of liquid. A small capillary tube leads to higher h, as $P_c \propto 1/r$.

In immiscible displacement of two-phase flow in porous media, at the pore level, capillary pressure is also exists at fluid-fluid interface. Capillary pressure affects flow behavior and the distribution of the two-phase flow in pores, particularly at low flow rates. By applying a force balance at the fluid-fluid interface, a relationship is obtained between the capillary pressure and the injected-displaced fluids pressures:

$$P_i - P_d + \alpha P_c = 0 \tag{2.14}$$

where the indices i and d refer to the injected and displaced fluids respectively, and α indicates the direction of the injected fluid to specify the flow regime and the capillary pressure direction. In case of wetting injected fluid, $\alpha = +1$, the capillary pressure applies in the same direction of the immsicible flow. This flow is called imbibition. For non-wetting injected fluid, $\alpha = -1$, capillary pressure applies against the imiscible flow and the flow is drainage.

2.3 Fluid Saturation

Fluid saturation is an important parameter related to fluid flow in porous media. As the porosity represents the capacity of the porous medium, fluid saturation specifies the volumes of fluids occupying pores of a porous medium [50, 51]. In two-phase flow, each phase can be calculated on the basis of the volumetric balance of the fluids available in the pores which are written in term of fluid saturation. For example, if phase 1 has a saturation of 25 %, this means 75% of the pores are hold the other phase. Furthermore, the importance of the fluid saturation is also related to the dependency

of the capillary pressure and the relative permeability, which are typically expressed in terms of the wetting phase saturation [2, 45]. Fluid saturation is defined as the ratio of the fluid volume to the pore volume.

$$s_j = \frac{\text{phase volume}}{\text{total pore volume}} \tag{2.15}$$

where the index j refers to the fluid phase. Since each fluid saturation is scaled to the pore volume, the total saturations of all fluids should be equal to 1.

$$\sum_j s_j = 1 \tag{2.16}$$

During immiscible displacement a portion of a fluid phase may become trapped inside the pores. Thus, saturation can refer to both mobile and immobile fluids in the porous medium. The trapped saturation that is related to the wetting phase is called irreducible saturation, and the non-wetting phase is called residual saturation. These saturations are usually refer to water-oil, where water is the wetting phase and oil is the non-wetting phase.

2.4 Capillary Pressure and Saturation

During immiscible displacement capillary pressure also depends on fluid saturation [52, 53]. This is related to the variation in the saturation of the injected-displaced fluids, which cause changes in the pressure across fluid-fluid interfaces. Figure 2.4(a)

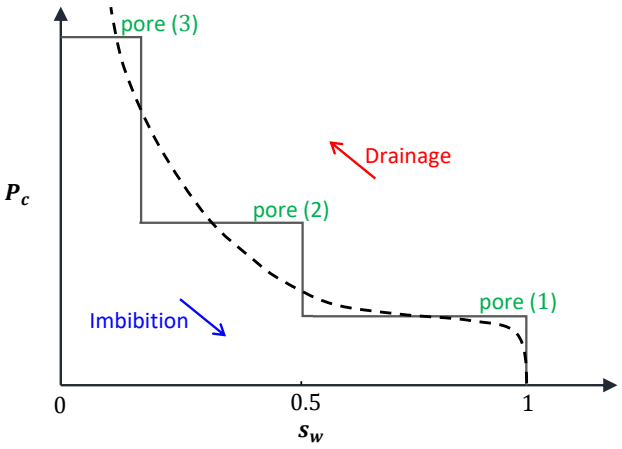

(a) Simple Porous Medium

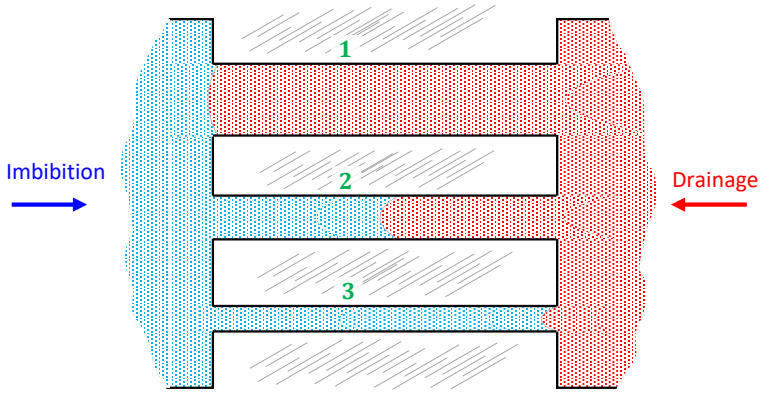

(b) P_c vs Wetting Fluid Saturation

Figure 2.4: (a) A simple sketch of a porous medium containing three pores, where $r_1 > r_2 > r_3$. Figure (b) shows the capillary pressure dependency on wetting fluid saturation.

shows a simple porous medium consisting of a bundle of three capillary tubes, where $r_1 > r_2 > r_3$. In case of imbibition, capillary pressure works as a driving force in the direction of the immiscible displacement ($\alpha = 1$). The smallest pore (r_3) offers highest capillary pressure so it will be invaded first, then pore 2 and 1 are invaded in sequence. Figure 2.4(b) shows the capillary pressure and the respective saturation history of the injected (wetting) fluid for the simple porous medium. At

the beginning, the maximum capillary pressure corresponds to minimum saturation of the fluid inside the smallest pore (r_3). Then capillary pressure decreases as the fluid saturation increases. The dashed line is indicative of an actual porous medium with a distribution of pore sizes. In the case of drainage (non-wetting injedted fluid), capillary pressure counters the direction of the immiscible displacement. The injected fluid starts to invade the pore with the lowest capillary resistance, pore 1. Then in sequence pore 2 and 3 are invaded. The trend for drainage is similar to imbibition, but in the opposite direction. In real porous media there is hysteresis between drainage and imbibition due to trapped saturations of the fluids.

Relationships between the capillary pressure and fluid saturation are based on empirical correlations. Leverett [52] provided a dimensionless function known by Leverett J-function to describe a curvature-saturation relationship for unconsolidated sands. Leverett J-function is obtained using the regression analysis to the interfacial curvature and a correlation is developed in term of fluid saturation. This method attempts to extrapolate capillary pressure-saturation data based on the porosity, permeability of the porous medium, and the interfacial tension of the two immiscible fluids.

$$\mathrm{J}(s_{\mathrm{w}}) = \frac{P_c}{\sigma}\sqrt{\frac{\kappa}{\varepsilon}} \tag{2.17}$$

where s_{w} is the saturation of the wetting phase. Correlations of Leverett J-function [1, 54] are obtained from experimental data of Leverett [52]. Equation 2.18 is the Leverett J-function suggested by Dong and Dullien [1].

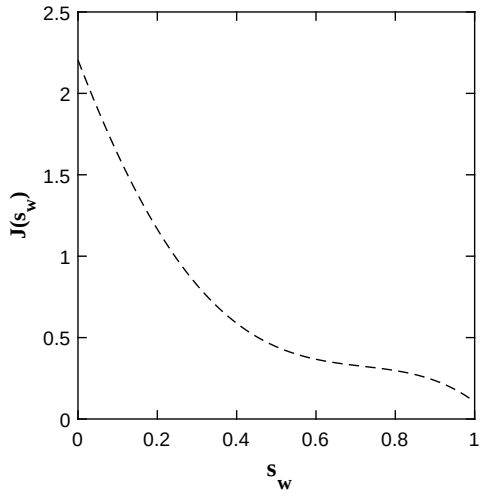

Figure 2.5: The Leverett J-fucntion for $\alpha = 2$, $\beta = 1.05$ and $\gamma = 2.5$ [1].

$$\mathrm{J} = \alpha(\beta - s_{\mathrm{w}})\,(2\,s_{\mathrm{w}}^{\gamma} - 2s_{\mathrm{w}} + \beta) \tag{2.18}$$

where α, β and γ are the fitting coefficients that are equal to 2, 1.05 and 2.5, respectively as shown in Figure 2.5. Capillary pressure is obtained by scaling the Leverett J-function by $1/\sigma \cdot \sqrt{\varepsilon/\kappa}$.

Brooks and Corey [2] also developed correlations for capillary pressure-saturation based on immiscible displacement of water-gas in soil. The correlations depend on two constants related to the porous medium, the pore size distribution index ξ, and the bubbling (bubble point) pressure P_b, which is a measure of the maximum pore size in the interconnected network in the porous medium. These constants characterize the pore size distribution of the porous medium.

$$P_c = P_b\, s_e^{-1/\xi} \tag{2.19}$$

where s_r is the residual saturation and s_e is the effective saturation of the injected fluid which is given by:

$$s_e = \frac{s_{\mathrm{w}} - s_r}{1 - s_r} \tag{2.20}$$

Another model derived by Parker et al. [3] for sand and clay using three fluids non-aqueous phase liquid (NAPL), air and water, where the wettability follows the sequence water > NAPL > air. The correlations are obtained based on the fluids pairs, air-NAPL, air-water, and NAPL-water.

$$P_c = P_b \left(s_e^{-1/m} - 1\right)^{1-m} \tag{2.21}$$

where the parameter m is restricted to the range $0 < m < 1$. Figure 2.6(a) shows the capillary pressure based on both correlations of Brooks and Corey [2] and Parker et al. [3] where the values of ξ, m, s_r and P_b are 1, 0.5, 0, and $0.125\,kPa$, respectively.

2.5 Relative Permeability

Absolute permeability, κ, is for the case of single phase flow in a fully saturated medium. In two-phase flow, the permeability for each phase is called the effective permeability, κ_j. Effective permeability indicates that the medium can have a distinct and measurable conductance to each fluid phase present in the medium. This means,

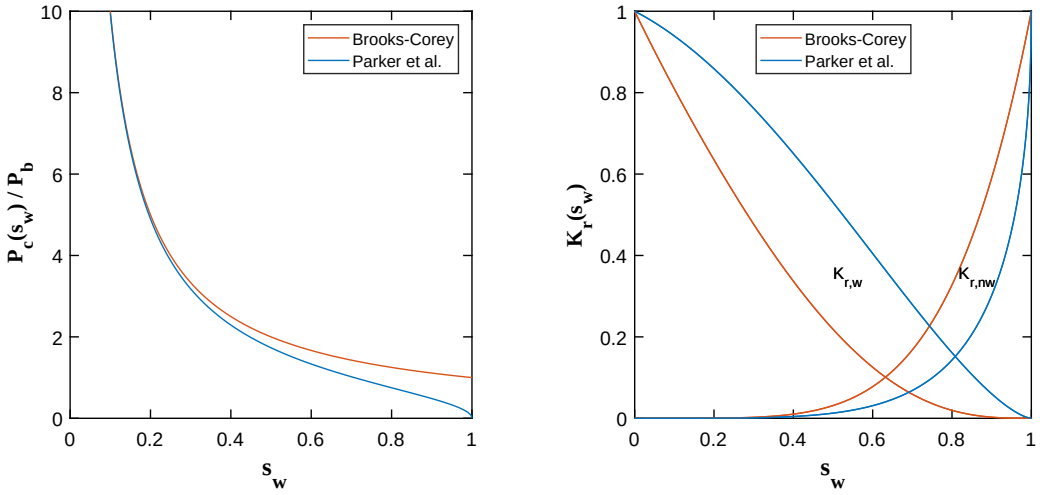

(a) Capillary Pressure

(b) Relative Permeability

Figure 2.6: ((a) Capillary pressure and (b) Relative permeability curves are calculated based on the correlations of [2] and [3]. The assumed values of ξ, m, s_r and P_b are 1, 0.5, 0, and 0.125 kPa, respectively.

as the phase volume in the pores increases, effective permeability also increases. Effective permeability depends on the phase saturation as well as to the morphology of the porous medium. Effective permeability is estimated for each phase using equation 2.22.

$$q_j = -\frac{\kappa_j A}{\mu_j}\frac{\Delta P}{\Delta x} \tag{2.22}$$

In order to quantify the mobility of each phase in porous medium, it is necessary to introduce and define another concept which is relative permeability, K_r. Relative permeability is the ratio of the effective permeability to the absolute permeability, and it is expressed as percentage or fraction [25].

$$K_{rj} = \frac{\kappa_j}{\kappa} \tag{2.23}$$

K_{rj} is phase j relative permeability, κ is absolute permeability (porous media property), and κ_j is the phase j effective permeability.

Two methods are commonly used to measure the relative permeability, steady-state [45, 55] and unsteady-state [24, 56]. In both methods, the porous medium is saturated with the wetting phase. To determine the irreducible trapped saturation, the porous medium is flooded with the non-wetting phase. In case of the steady-state method, volumetric ratios of both phases are tested to obtain sufficient data to cover the whole range of saturation-relative permeability curves. In the unsteady-state method, the fluid is displaced at a constant injection rate while the effluent saturations are measured continuously. Due to the capillary end effect [57] or the associated piston-like displacement with the unsteady-state method [24], the steady-state method is the more common method to measure the relative permeability.

Correlations of relative permeabilities suggested by Brooks and Corey [2] are:

$$Kr_i = {s_e}^{2+3\xi/\xi} \tag{2.24}$$

$$Kr_d = (1 - s_e)^2(1 - {s_i}^{2+\xi/\xi}) \tag{2.25}$$

The correlations of relative permeabilities which are suggested by Parker et al. [3].

are applicable to three-phase flow, and it can be reduced to expressions convenient for two-phase flow [3, 58]:

$$Kr_i = s_e^{1/2}[1 - (1 - s_e^{1/m})^m]^2 \tag{2.26}$$

$$Kr_d = (1 - s_e)^{1/2}(1 - {s_i}^{1/m})^{2m} \tag{2.27}$$

Figure 2.6(b) shows the curves of the relative permeabilities based on both studies, [2] and [3].

2.6 Immiscible Displacement Flow Regimes

The main forces that dominate immiscible displacement are viscous and capillarity. These two forces are quantified in a dimensionless number known by the capillary number, $Ca = (v_i\,\mu_i)/\sigma$, which represents the ratio of viscous effects to capillary effects, where v_i and μ_i are the velocity and the viscosity of the injected fluid respectively, and σ is the surface tension. Another dimensionless number that is used to describe immiscible displacement is the viscosity ratio, $M = \mu_i/\mu_d$, which is the ratio of injected to displaced fluid viscosities [59].

For both drainage and imbibition at high Ca, viscous effects are dominant. For high viscosity ratio ($M > 1$), the displacement pattern of the injected fluid spreads evenly in all directions in a stable displacement pattern, while at low viscosity ratio ($M < 1$),

the immiscible displacement becomes unstable and is known by viscous fingering flow. At low capillary number, capillarity is the dominant effect and immiscible displacement is known as capillary fingering flow [59, 60]. In case of imbibition at a very low capillary number, the pattern is a capillary fingering, but the domain is discontinuous (corner flow) [59]. A comprehensive discussion of immiscible displacement flow patterns in porous media has been published by Primkulov et al. [61].

Chapter 3

Catalyst Layer Structure

Proton exchange membrane (PEM) fuel cells are low temperature ($< 90°C$) electrochemical devices which combine hydrogen and oxygen to produce electricity, heat, and water. A generic fuel cell consists of an anode and cathode separated by an electrolyte layer, known as a proton exchange membrane, and all compressed by two bipolar plates that serve to pass electrical current and heat as shown in Figure 3.1. Each bipolar plate includes channels as a path for the reactants and products for transport to and from the electrodes. The electrodes are porous catalyst layers (CL) located between the PEM and the bi-polar plates. Additional porous layers, such as a porous transport layer (PTL) and/or microporous layer, are often added between the electrodes and the bipolar plates to support the CL and enhance mass transport. At the anode side, hydrogen oxidation reaction (HOR) produces electrons to be collected by bi-polar plates to supply an external load and protons of hydrogen that migrate through the membrane to the cathode side. At the cathode side, the oxygen reduction reaction (ORR) completes the circuit with the protons and electrons to produce

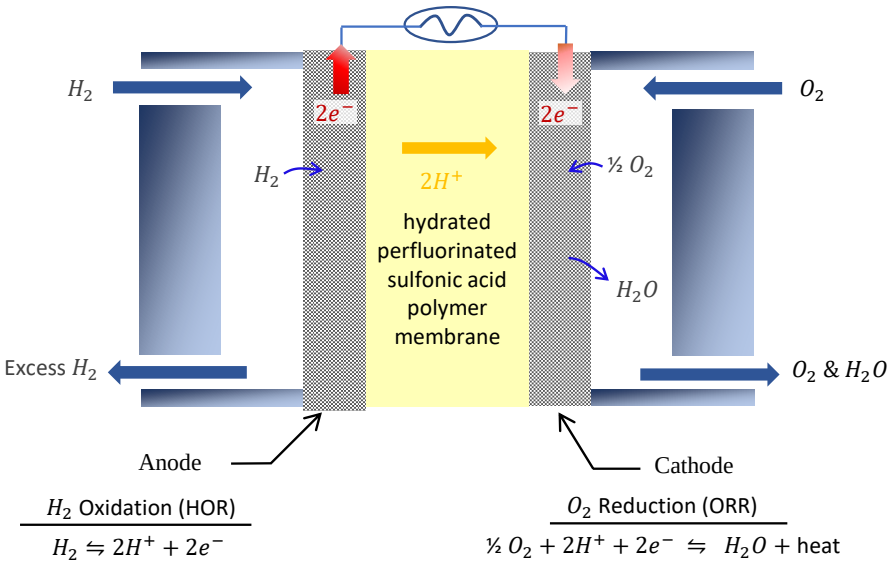

Figure 3.1: A general sketch for the components of fuel cell.

water. An excessive presence of water at the cathode side may significantly lower the PEMFC performance and lifetime [62]. The behavior of liquid water percolating through the porous CLs is still not well understood, where proper water removal is crucial. This chapter and the next two are dedicated to study of the CL.

3.1 Conventional Catalyst Layers

A catalyst layer is a thin porous material ($< 15\mu m$) that is usually coated on both sides of the membrane to form what is known as catalyst coated membrane (CCM) or membrane exchange assembly (MEA). Figure 3.2(a) is an SEM image of the cross-section of a conventional CCM. Figure 3.2(b) is an SEM image of the structure and morphology of the CL surface, in which the spherical-like structure is the aggregation of carbon, ionomer, and the catalyst (typically, platinum (Pt) or platinum alloy) that

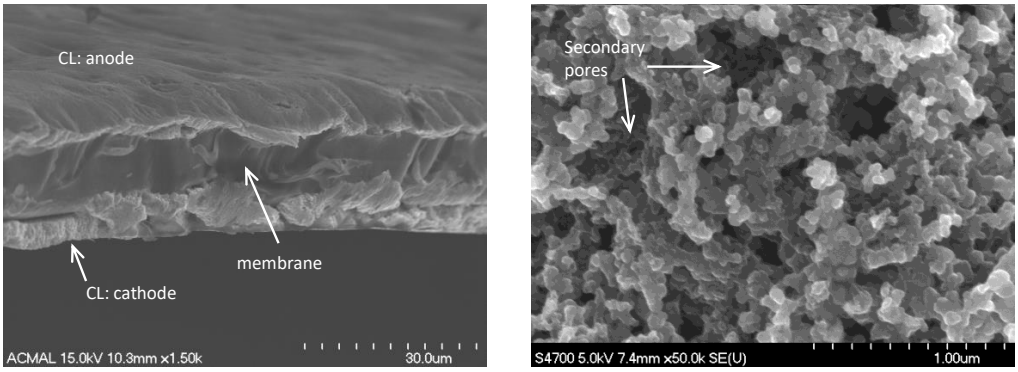

(a) CCM (b) CL

Figure 3.2: (a) Catalyst coated membrane. (b) Catalyst layer structure.

form what is known as agglomerates. The carbon particles are thermally and electrically conductive and serve as a support to the catalyst aprticles of Pt. Nanometer thick ionomer films work as a binder and assure protonic conductivity. Between and withing agglomerates are pores that are a transport path for the reactants and water as a vapor or liquid. The structure of agglomerates were examined using FEI $200kV$ Titan Themis STEM. Figure 3.3 are bright field (BF) images of agglomerates where the carbon is a substrate on which Pt particles are dispersed. Ionomer films are identified at the edges as shown in Figure 3.3(e) and 3.3(f).

Energy-Dispersive X-ray (EDX) spectroscopy was used in the analysis of elemental composition and mapping. Figure 3.4 shows the mapping for each element of the conventional CL. High Angle Annular Dark Field (HAADF) (Figure 3.4(a)) shows part of the conventional CL placed on a grid holder (seen in the background). By disregarding the carbon and sulfur distribution in the grid holder, the distribution of all elements appears to be evenly spread through the entire structure of the CL.

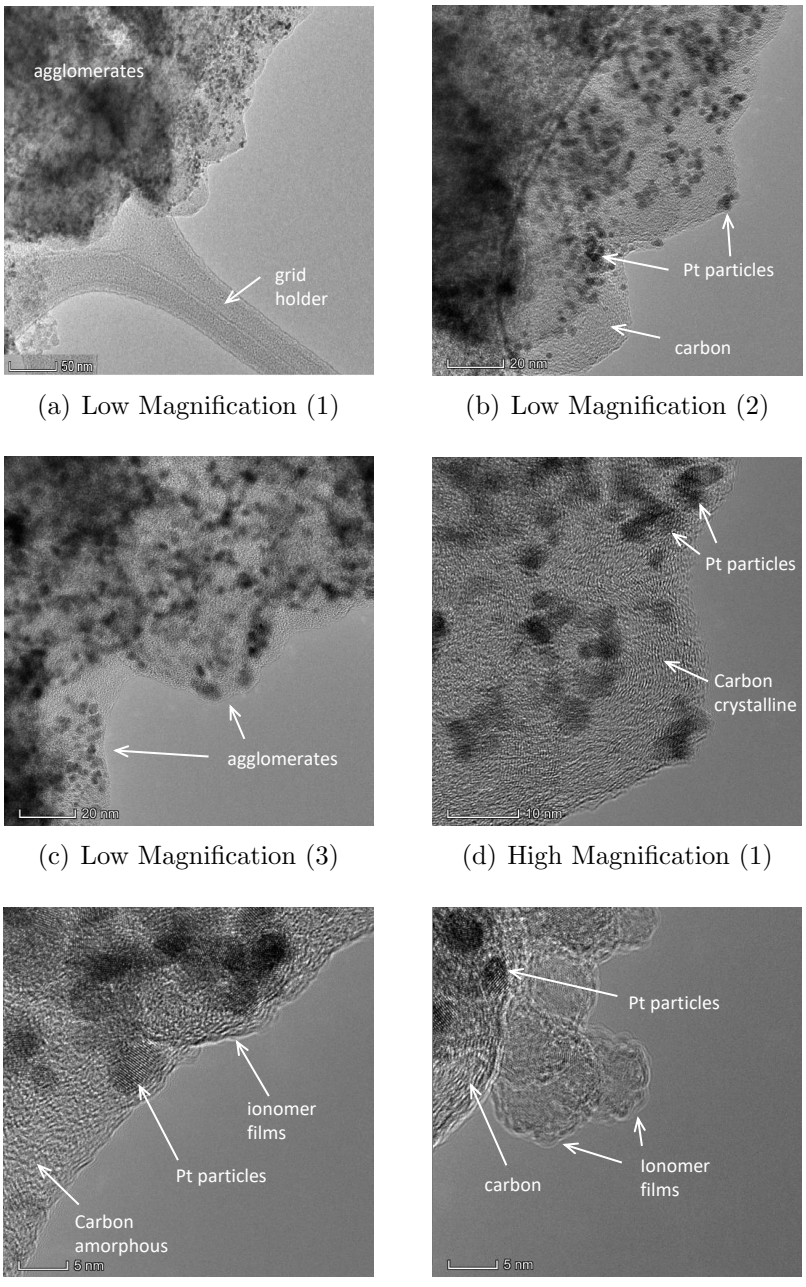

(a) Low Magnification (1)

(b) Low Magnification (2)

(c) Low Magnification (3)

(d) High Magnification (1)

(e) High Magnification (2)

(f) High Magnification (3)

Figure 3.3: BF TEM images showing carbon, catalyst particles (Pt), and ionomer films. CL details are: CL name ($10V50E$); Pt loading ($0.197\,mgPt/cm^2$); EW=PFBI-2; I/C = 0.9.

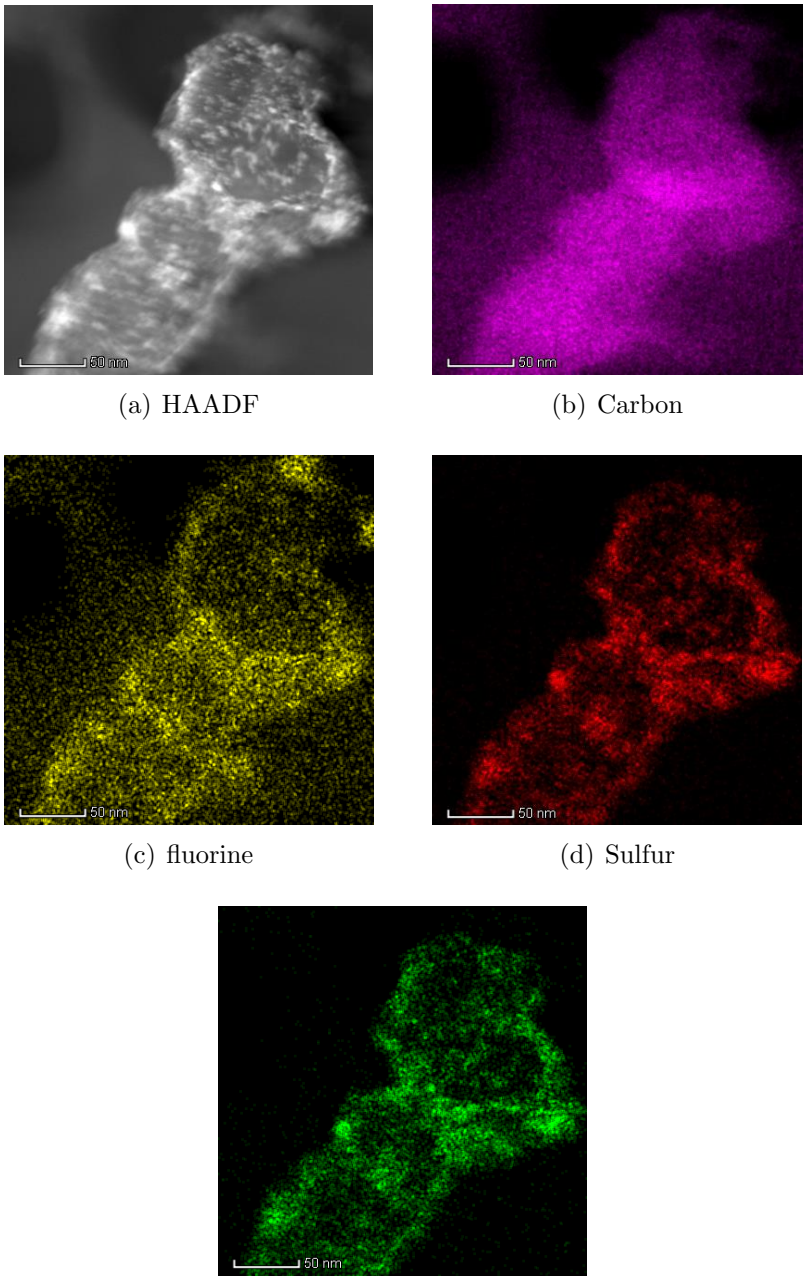

(a) HAADF

(b) Carbon

(c) fluorine

(d) Sulfur

(e) Platinum

Figure 3.4: Analysis of elemental composition and mapping for conventional CL using Energy-Dispersive X-ray (EDX) in conjunction with the STEM. CL details are: CL name ($10V50E$); $0.197\,mgPt/cm^2$; EWPFBI-2; I/C = 0.9.

3.2 Dispersed Nano Structure Thin Films

The conventional CL relies on carbon particles ($50\,nm$) to support the nanoparticles of platinum (2-5 nm), which could dissolve and agglomerate, and that cause reduction in the active surface area [63]. Dispersed Nanostructured thin film (dNSTF) catlaysts are whisker ($40\,nm \times 500\,nm$) comprised of a thermally and chemically stable organic pyrelene red core coated with platinum and ionomer. Figure 3.5 shows a porous cathode electrode in the cross-section view (Figure 3.5(a)) and surface view (Figure 3.5(b)) comprised of whiskers and agglomerates, which consist only carbon and ionomer. This type of CL has achieved an improved oxygen reduction activity and reduced electrochemical corrosion [63–65]. STEM and TEM images are shown in Figure 3.6. Figure 3.6(a) is a HAADF STEM image showing platinum particles that are dispersed on the whiskers. Figures 3.6(b)-3.6(f) are BF TEM images for dNSTF at low and high magnifications showing the geometrical shape of the whisker with

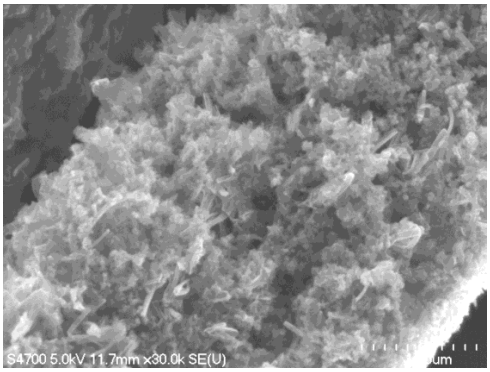

(a) Cross-Section View

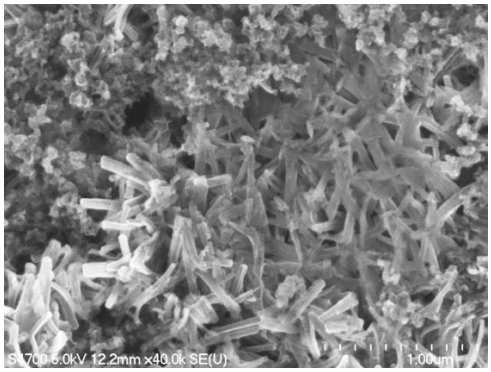

(b) Surface View

Figure 3.5: An SEM images for the dNSTF CL. (a) Cross section view (b) The Surface area shows the whiskers (dNSTF) and the carbon-ionomer agglomerates.

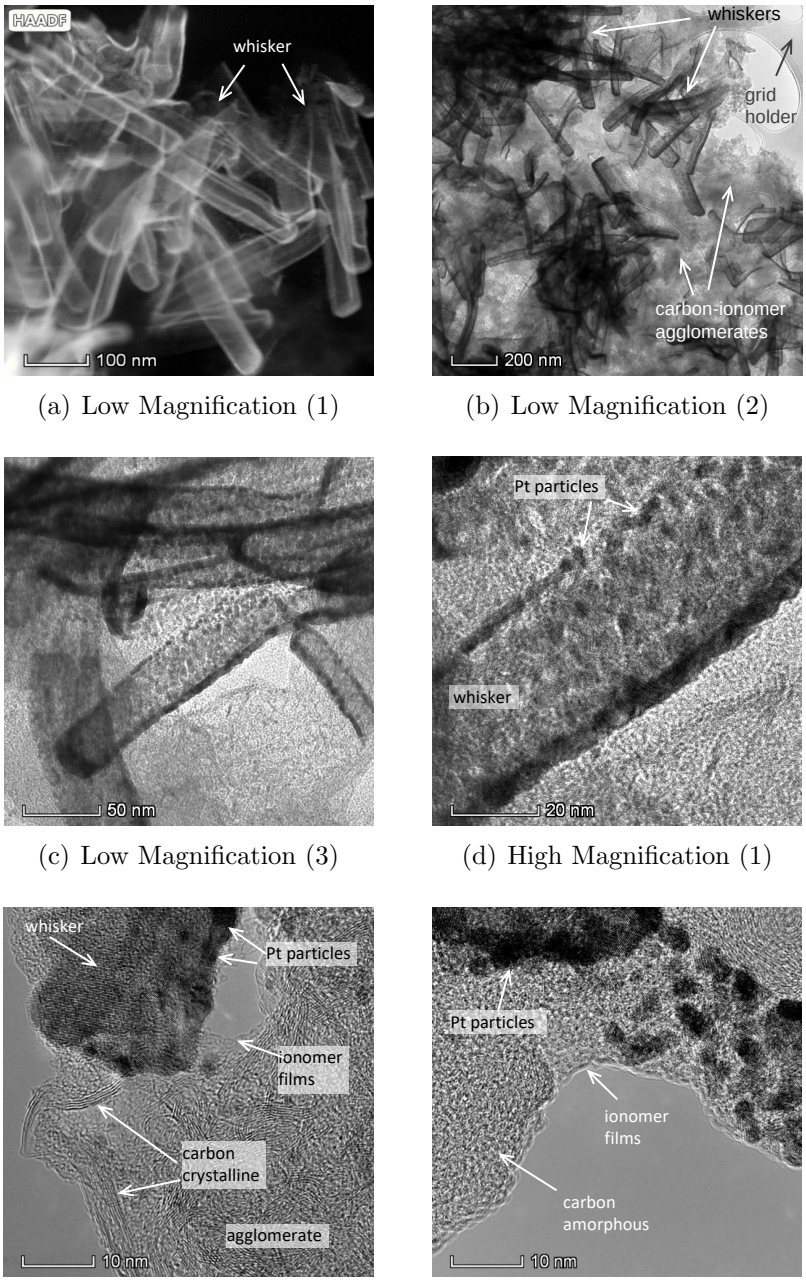

(a) Low Magnification (1)

(b) Low Magnification (2)

(c) Low Magnification (3)

(d) High Magnification (1)

(e) High Magnification (2)

(f) High Magnification (3)

Figure 3.6: (a) A HAADF STEM image for dNSTF CL, which mostly shows the platinum distribution on the whiskers. (b-f) BF TEM images at low and high magnifications show the whiskers, agglomerates, ionomer films, and dispersed platinum. NSTF CL details are: CL name is HSC; EW=PFBI-2; I/C = 0.9; Wh/C= 2.5.

dispersed platinum on the surface. Carbon particles are both in a crystalline (Figure 3.6(e)) and amorphous (Figure 3.6(f)), while thin ionomer films are observed at the edges of the carbon.

Figures 3.7 and 3.8 are EDX analyses for a group and single NSTFs. Carbon and fluorine are distributed on the entire area, which is more likely related to their presence on the whiskers themselves and on the agglomerates in the background. Sulfur and platinum are more concentrated on the whiskers as shown in the Figures *d* and *e* of both 3.7 and 3.8.

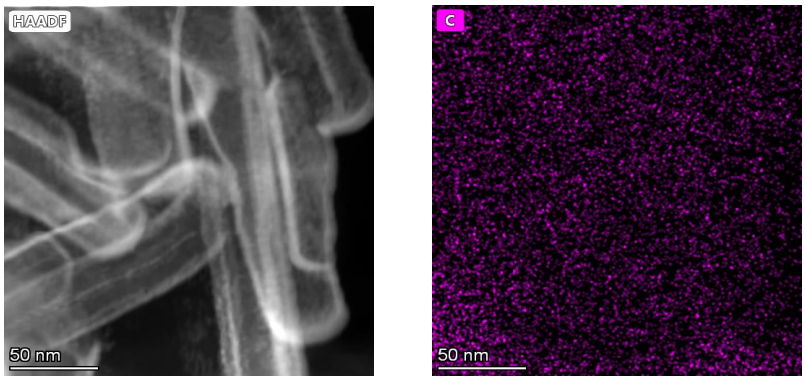

(a) HAADF

(b) Carbon

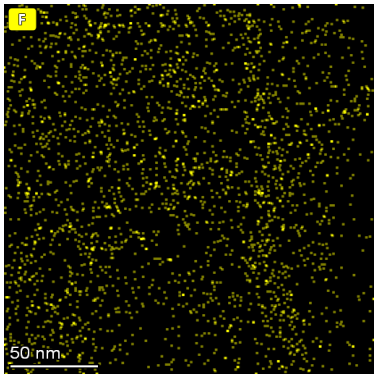

(c) Fluorine

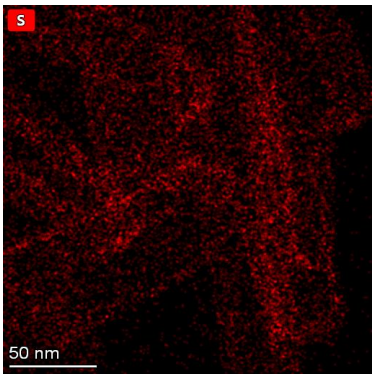

(d) Sulfur

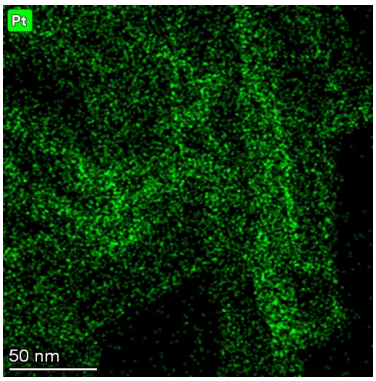

(e) Platinum

Figure 3.7: A HAADF STEM image for dNSTF CL. (b-f) Elemental composition and mapping for dNSTF CL. NSTF CL details are: CL name is HSC; EW=PFBI-2; I/C = 0.9; Wh/C= 2.5.

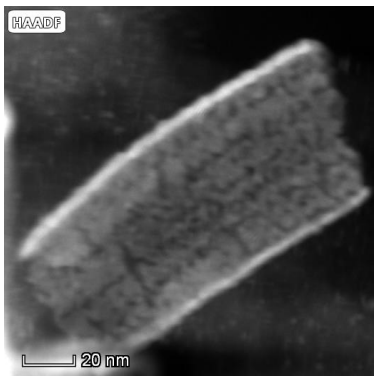

(a) HAADF

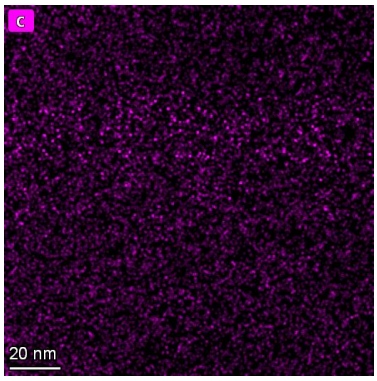

(b) Carbon

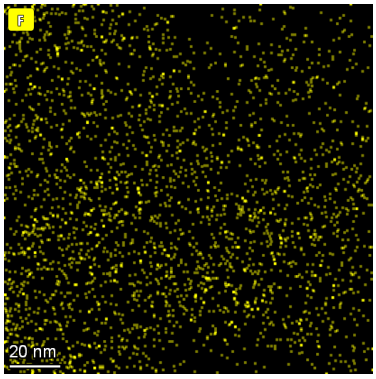

(c) Fluorine

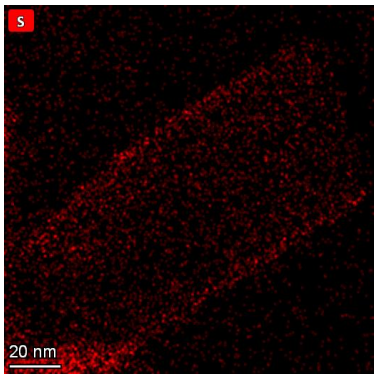

(d) Sulfur

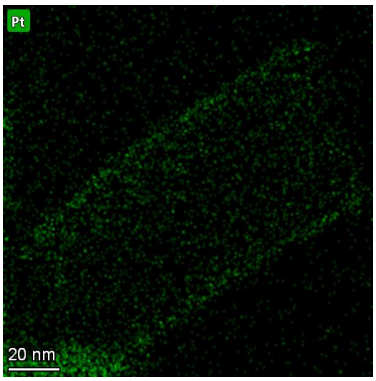

(e) Platinum

Figure 3.8: (a) A HAADF STEM image for a single whisker. (b-e) Elemetal composition and mapping. NSTF CL details are: CL name is HSC; EW=PFBI-2; I/C = 0.9; Wh/C= 2.5.

3.3 I/C and EW Effects on Structure and Morphology

The ionomer to carbon weight ratio, I/C, and the equivalent weight, EW can affect morphology and structure of CL. EW is only related to the ionomer, which is the mass of the backbone polymer to the moles of the proton-conductive side chain (sulphonic acid group). Figure 3.9 shows SEM images of two CLs of different EW, and each set includes CLs at different I/C. All the CLs layers are printed on Kapton layers. Both EW, at I/C = 0.6 appear less porous as compared to higher I/C. The CL of EW = 725 at any I/C are more porous than EW = 825. In addition, the roughness of the surface appears greater for increased porosity.

Equation 3.1 is the relationship between porosity and ionomer ontent. The increase in the ionomer contents, changing I/C, or any changes in its chemistry (EW) leads to significant structural and morphological changes, which can affect the wettability or the mass transport. Additional complexity added to the structure of the CL is that water retention by ionomer films leads to an increase in the solid volume, and that reduces porosity. The next two chapters focus on RH effects on permeability, structure, flow regime transition, and wettability of the CL.

$$\varepsilon \downarrow = \frac{\text{pore volume } \downarrow}{\text{carbon} + \text{ionomer} \uparrow \text{f}(RH \uparrow) + \text{pore volume } \downarrow} \tag{3.1}$$

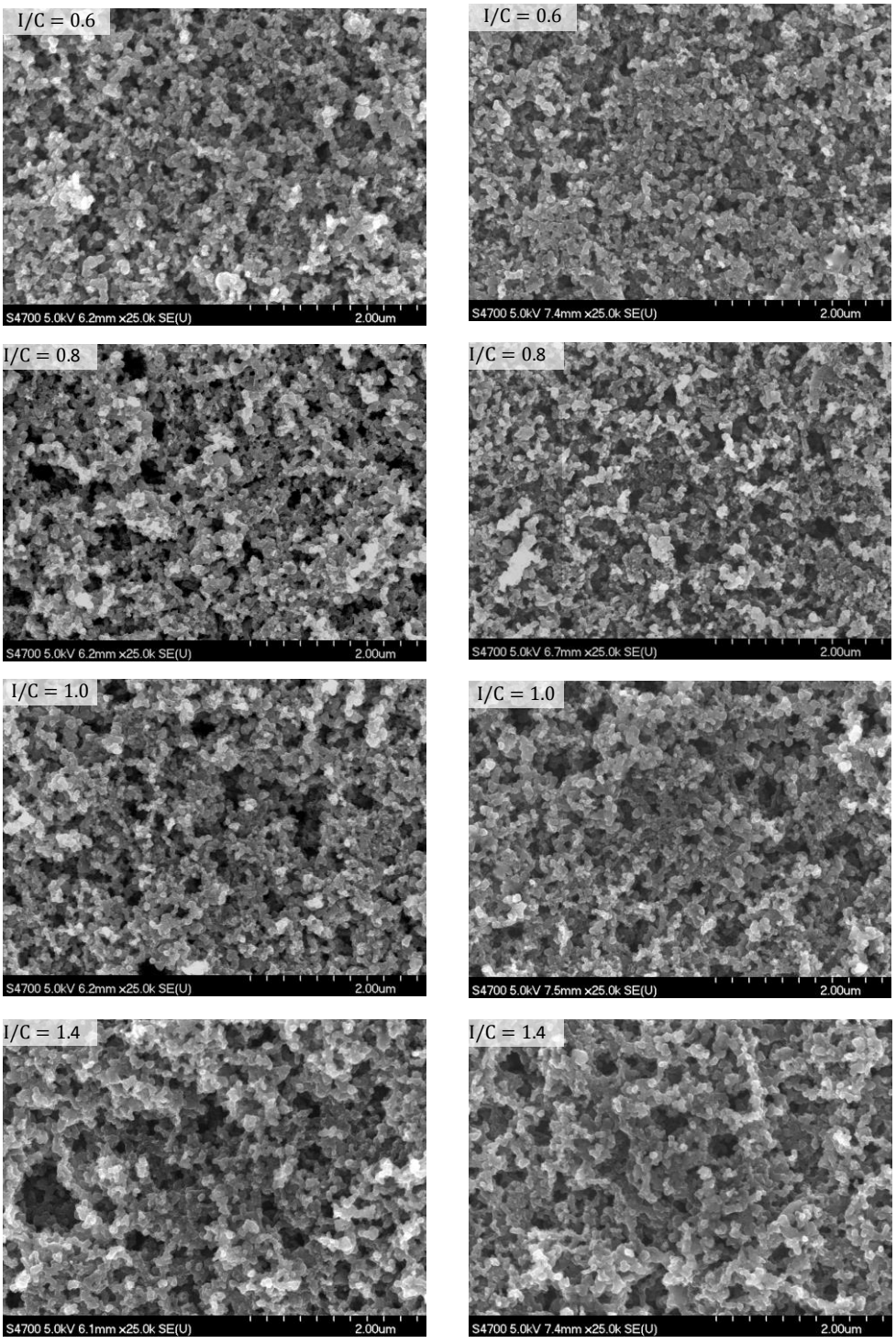

(a) EW = 725 (b) EW = 825

Figure 3.9: An SEM images for the top surface of conventional CLs. (a) CLs of EW = 725 have a different I/C. (b) CLs of EW = 825 have a different I/C.

Chapter 4

Ex-Situ Examination of Mass Transport Resistance in a Fuel Cell Catalyst Layer

Gas/liquid transport in the catalyst layer (CL) is investigated experimentally in terms of percolation pressure and corresponding wetted area. Ionomer films in the CL add complexity because they interact with water and swell, which affects percolation. An ex-situ setup is used to study mass transport in a CL at different injection rates and relative humidity (RH). High injection flow rates force liquid through the bulk of the pores and the dominant force is viscous. At low injection rates capillarity is dominant, liquid flow along the surface roughness of the pores which results in a larger wetted area with lower saturation as compared to high injection rates tests. In the second set of testing the injection rate is fixed and RH is varied. The resistance to gas/liquid flow changes due to ionomer swelling. The result is a significant change

in the permeability of the CL that indicates a limit on reactant transport.

4.1 Introduction

Fuel cells suffer from poor water management which causes a reduction in the performance [26, 66–70]. The water product at the cathode side has a counter effect. It enhances the protonic conductivity of the ionomer films in the CL and the proton exchange membrane (PEM) [71], but an excessive amount of condensed water will block the pores, which are the only paths for oxygen to reach the reaction sites [26, 66]. Figure 4.1 shows an SEM image with a schematic for the conventional CL, which is a thin porous material ($< 15\,\mu m$ thickness) that consists of a heterogeneous micro/nanostructure in which the ionomer films ($4 - 10\,nm$ thick [72, 73]) serve as a binder to the carbon particles to form what is known by agglomerates. The catalysts, usually platinum alloys, are dispersed on the carbon particles. Ionomer and carbon are paths for protons and electrons, respectively. Pores up to $1\,\mu m$ [74] are produced in-between the agglomerates and are known as secondary pores. Each agglomerate by itself is a porous medium that contains mesopores, $\leqslant 30\,nm$ [75], known as primary pores. Both the primary and secondary pores are paths for oxygen and water (vapor or liquid).

The structure of the pores [76] and the pore size distribution [77] are important factors to determine the fuel cell performance [76, 77]. Different fabrication techniques are used to achieve better catalyst layer performance [78]. Porosity and thicknesses of $5\,\mu m$ [79] or $7.5\,\mu m$ [80] were found to improve mass transport. Ionomer content can also affect the structure of the CL, where any increase in the ionomer content reduces

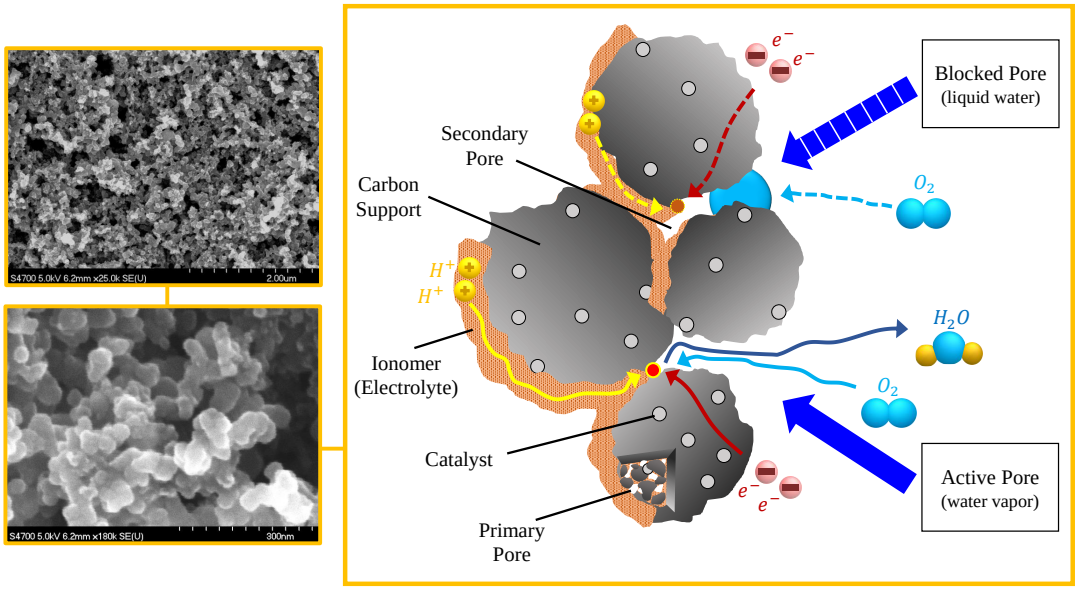

Figure 4.1: An SEM image of the surface of the CL with a structure schematic to show a blocked pore, liquid water prevent oxygen reach Catalyst, and an active (opened) pore, where oxygen can reach the catalyst.

the number of secondary pores. Primary pores, however, are found to be independent of ionomer content [74]. Increasing ionomer content leads to increased proton conductivity and decreased oxygen diffusion, while the reverse is true at low ionomer content [79]. Optimal ionomer content is sought to optimize fuel cell performance [79, 81–83].

The sulfonic acid group in the ionomer interacts with water and it can retain up to 15 molecules of water in the bulk [5]; less for thin films of ionomer [4, 84, 85] when exposed to water vapor. This retention of water in the ionomer thin films causes swelling [86–88] and that adds complexity to the structure and mass transport. Several experimental studies have been carried out to investigate effects of RH on CL performance [30, 71, 89, 90]. Wang et al. [71] experimentally showed that as RH increased the O_2 and H_2O transport resistance increased, while the proton transport

resistance decreased. In addition, as the water is retained by the ionomer films in the CL a structural change occurs. With the RH cycling, agglomerates detach from each other causing growth and propagation of cracks that has a significant impact on the fuel cell performance and durability [30].

Despite these previous studies, the effect of RH on mass transport in a CL is not yet understood. The experimental studies related to the transport are mostly focused on the porous transport layer (PTL), also known as the gas diffusion layer (GDL). This is related to the location of PTL at the flow field which allows a wide area for clear visualization using many in-situ techniques [91–93]. In addition, a stiff porous material like PTL with a relatively large thickness of $200-350\mu m$, ex-situ experiments can be easily achieved [36, 94–98]. CLs are thin, fragile materials that are difficult to handle without a supporting layer. It is usually coated on the membrane, known as catalyst coated membrane (CCM) [99]. The CL is concealed between the PTL and membrane, which limits exploring mass transport with in-situ diagnostics to the through-plane direction [69]. For in-plane studies, part of the PTL must be removed [67]. Rotating disk electrode is another technique that is used to study the kinetics of oxygen reduction reaction [100, 101] and the mass transport of O_2 in term of corrected current density [102].

In this study, gas/liquid transport in the CL is investigated experimentally in terms of time-dependent percolation pressure and wetted area. The experiments are conducted in two different types of testing. The initial tests investigated immiscible displacement in the CL at a range of flow rates when the RH condition remains constant. The second type of tests investigated in the CL in terms of permeability over a range of RH conditioning when the injection rate remained constant.

4.2 Experimental Description

4.2.1 Radial and Uni-directional Flow

Percolation maybe uni-directional (channel) or radial. Uni-directional flow can be in-plane or through-plane, while the radial flow is limited to the in-plane direction [103]. The CL samples are a thin (a few microns thickness) fragile material that can not be tested in the through-plane direction. Even for in-plane direction using channel flow, there are some concerns related to the boundary effect on the fluids flow. In this study, radial flow with a CL sample compacted between two platens and liquid injected in the middle was used for percolation testing of catlayst layers.

4.2.2 Percolation Setup

Figure 4.2 shows a schematic for the percolation setup. The sample is placed between two square platens of Polymethylmethacrylate (PMMA), a transparent material that allows visualization of liquid percolation. An air cylinder, Parker model: TB2MAUVS19, is used to compress the PMMA platens, between which the sample is sandwiched as shown in Figure 4.2. This is a Hele-Shaw arrangement designed to assure fluid percolation throughout the pores of the catlayst layer instead of the sample-platen interface. A stand-alone humidifier was used to bring dry N_2 gas to the required RH, which in turn was passed through the sample prior to the liquid percolation. The condition of the gas N_2 is measured using an accurate RH ($\pm 0.01\%$) and

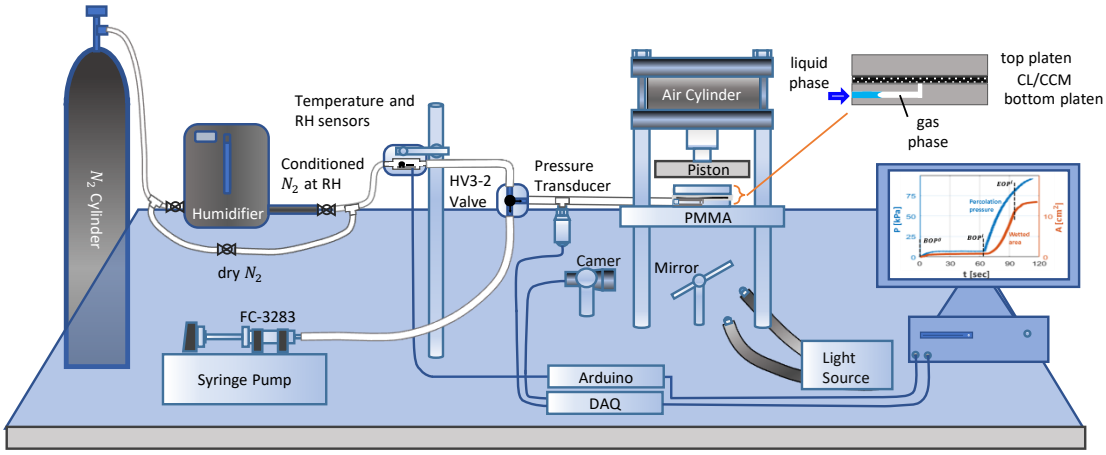

Figure 4.2: Experimental setup using Hele-Shaw flow to test CL of PEMFC.

temperature ($\pm 0.1\,^{\circ}C$) sensors, connected to Mega 2560-R3 board compatible with Arduino. After conditioning the sample with the humidified N_2 for several hours, percolation testing starts by injecting liquid using a syringe pump, Harvard Apparatus model 2274. The test liquid is 3M Fluorinert (FC-3283). injection occurs through $2\,mm$ diameter hole located in the middle of the bottom PMMA plate.

Percolation testing begins by placing the meniscus of the liquid phase at a distance from the sample (top-right of Figure 4.2). The gap between the liquid meniscus and the sample contains gas (air or the conditioned N_2). The syringe pump moves the liquid at a constant rate, then by starts injecting gas at the beginning-of-percolation (BOP^g). The volume of the gas between the meniscus and the sample is sufficient to percolate through the sample until reaching a steady injection pressure. The pressure transducers, Omega PX309-V30G10V, record the percolation pressure during testing. Hamilton three port valve (HV3-2), part number 86728, manages fluid flow from two sources, the humidifier line and the syringe pump line. A CCD camera, Panasonic GP-KS125, is used for imaging. The sample image is reflected by a square mirror

(7.62 cm size) below the sample to the camera. Recorded images are used to estimate the evolution of the wetted area of the liquid during percolation. To enhance image contrast, a gooseneck illuminator is projected on the sample area.

4.2.3 Image Processing

The wetted area, A, of the liquid phase is obtained by imaging the sample during percolation. A reference image of the CL taken before the percolation starts is subtracted from subsequent images. An edge detection algorithm written in Matlab [60] is used to define the liquid front. A threshold value is applied between the reference image and other images so the liquid/gas interface is recognized and then the wetted area is calculated. This process is done for each image to obtain the wetted area, which is synchronized with the percolation pressure. The wetted area curve was used to find the liquid beginning-of-percolation (BOP^l) and the end-of-percolation (EOP^l). In addition, the wetted area with the percolation pressure were used to identify the flow regime, estimate effective saturation, and determine the permeability of the CL.

4.3 Samples Specifications

3M provided two samples of CLs that had different ionomers for this study. The samples properties are shown in Table 5.1, where they are named with respect to the equivalent weight (EW) as EW825 and EW725. EW825 is a CCM; it only has a cathode and the other side of the membrane is supported by a PTFE layer. The second CL (EW725) is printed on a Kapton layer and it does not have dispersed

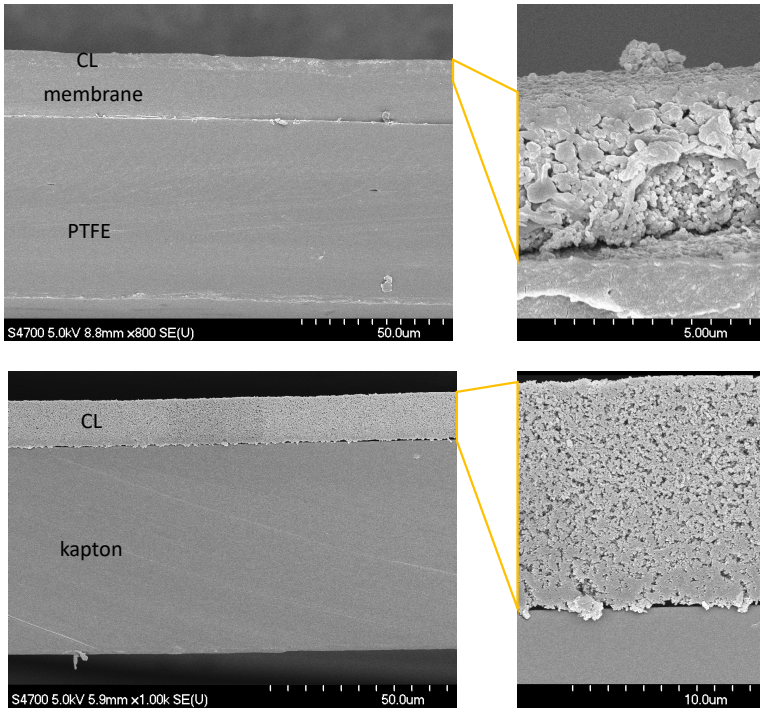

Figure 4.3: The cross section for both CL samples. The top image is for sample EW825, and the bottom one is for EW725. Both CLs are coated with a $6\,nm$ conducting material to avoid charging at the Kapton and PTFE.

platinum particles. The supports for both samples, PTFE and Kapton, are to keep the samples stiff and flat during testing. The thickness of EW825 and EW725 are $4.5\,\mu m$ and $12.5\,\mu m$ respectively, which are determined using SEM imagingas shown in Figure 4.3. The total thickness with other layers $90\,\mu m$ and $72\,\mu m$ for EW825 and EW725, respectively. The EW is different for both samples as well as ionomer-to-carbon ratio, I/C. EW825 was maintained at a constant RH condition and tested at different injection rates. EW725 was tested at different RH conditions and a single injection rate.

Other properties of the CL, such as surface roughness, wettability and water retention, that could affect percolation pressure were investigated. Surface roughness was

Table 4.1
Samples specifications.

Sample	**Pt-Loading** $(mg/cm2)$	**EW**	**I/C**	**Thickness** (μ)
EW825	0.19	825	0.9	90
EW725	no Pt	725	0.8	72

measured for both CLs using a laser surface profiler, COBRA model CB1053, at different RH conditions. Figure 4.4(a) shows no significant changes in the surface roughness, though, there is a difference between the two CLs. The wettability for both samples was measured in terms of contact angle using di-ionized water as shown in Figure 4.4(b). The contact angle is mainly affected by the surface roughness, while the difference between the two CLs is related to the platinum in EW825.

Water can be retained by ionomer films, which can results in rapid changes to the

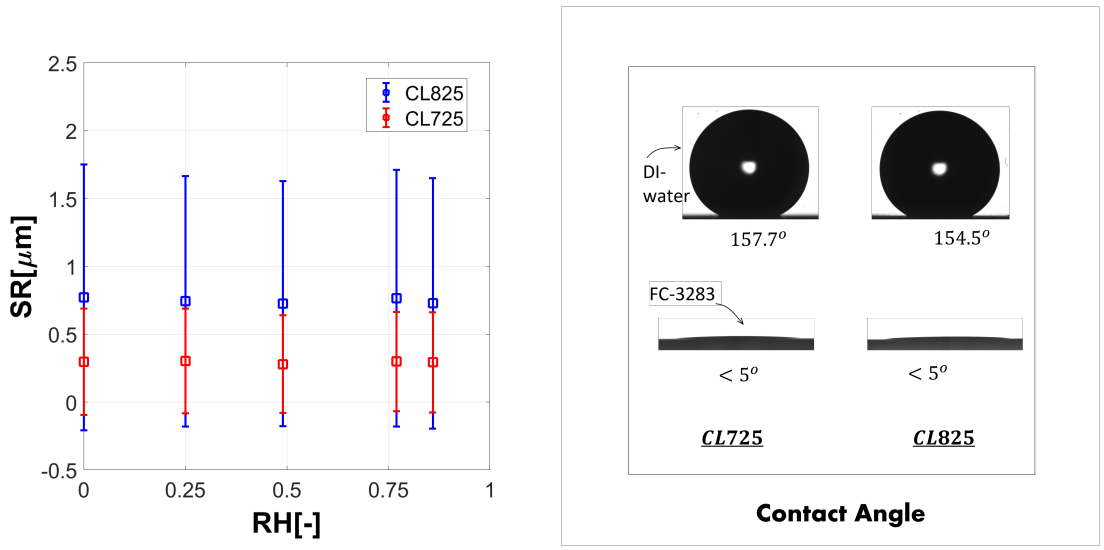

(a) Surface Roughness

(b) Wettability

Figure 4.4: (a) The surface roughness of the two CLs, EW725 and EW825, at different RH conditions. (b) The wettability of the CLs EW725 and EW825 with respect to DI-water and FC-3283.

structure of the CL [90]. Therefore, water was not used as a working fluid. FC-3283 is used instead because it does not interact with ionomer. Also, FC-3283 is a very wetting fluid with a contact angle less than 5° on the surface of both CLs as shown in Figure 4.4(b). This allowed probing of the smallest pores in the structure of the CL to observe any changes when the RH condition changes.

4.4 Sample Conditioning and Testing

The experiments were run in two different types of testing as shown in Table 4.2. The first one is to explore the percolation of air and FC-3283 when testing at a range of injection rates. This testing was performed on the EW825 sample. Between test to test, the CL is maintained at the ambient condition $(22 - 25\,^{\circ}C, 17 - 20\%\,\mathrm{RH})$ for two days to allow the CL to fully dry before the next test. To assure reliable and consistent results, more than three tests were repeated for each injection rate.

The second test of testing was to explore the RH effect on the permeability of the CL using humidified N_2 and FC-3283 as a working fluids, where the injection rate is maintained constant. Sample EW725 is used for this set of testing because it does not include a membrane so that any changes in the CL are only related to the ionomer films in the CL. Before each test, the sample is conditioned to specific RH, while the temperature is uncontrolled and remains in the range of $22 - 25\,^{\circ}C$. The process is done by injecting humidified N_2 for three hours as shown in Figure 4.5.

In both of experiments recorded data included the transient percolation pressure and the images of the wetted area. The transient pressure data included gas injection (air

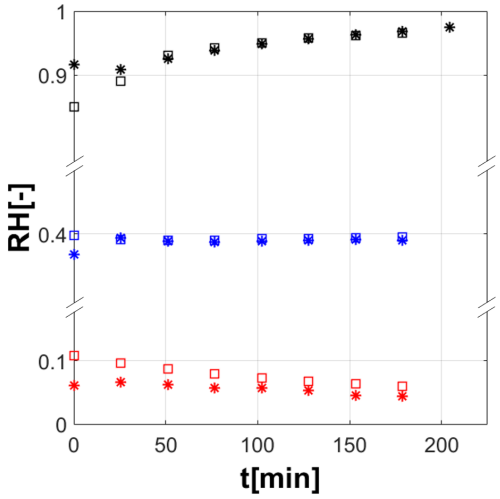

Figure 4.5: Relative humidity of N_2 passing through sample EW725 prior to percolation testing.

or N_2) and FC-3283 injection. As the meniscus of the FC-3283-gas (air or N_2) reaches the CL, the BOP^l of the FC-3283 starts, which also can be identified by a pressure jump. The transient wetted area of the FC-3283 is calculated from the captured images [60, 99]. The EOP^l is only specified for FC-3283 when FC-3283-gas reaches the edge of the sample.

Table 4.2
Conditions of the experimental tests.

	Sample Name	**Size cm^2**	**Conditioning at 22-25 °C**	**Flow Rate mm^3/s**
Flow Rate Effect	EW825	3.81×3.81	leaving the sample at the ambient condition, $(17-20\%\,RH)$	0.525 0.097 0.025 0.0066
RH Effect	EW725	6.35×6.35	$5-7\,\%\,RH$ $25-27\,\%\,RH$ $40-42\,\%\,RH$ $65-96\%\,RH$	0.025

4.5 Effect of Injection Rate on Percolation

Figure 4.6 shows the raw data for each flow rate speed, where the BOP^g, BOP^l, and EOP^l are indicated. The raw data includes air and FC-3283 percolation pressure, while the sub-figures are only for air percolation in which the BOP^g of all tests are overlapped. At a high injection rate, $0.525\,mm^3/s$, the air percolation pressure keeps increasing until reaching a plateau, the maximum steady pressure. As the injection rates decrease, Figure 4.6(b)-4.6(d), the gas maximum pressures decrease too. When FC-3283 starts invading the CL pores, BOP^l, the percolation pressure increases suddenly in a sharper slope than the gas phase (air) because of the high viscous effect of the FC-3283, as shown in Figure 4.6. The relationship between the percolation pressure and the injection rate for FC-3283 is similar to the air , where the pressure increases as the flow rate increases, while the percolation time decreases. All the tests for each injection rate are consistent until reaching the EOP^l, there is a slight change that could be related to the sample boundaries. The consistency in the percolation pressure data provided confidence in the technique.

4.5.1 Liquid Imbibition in The CL

In Figure 4.7(a) and 4.7(b), the liquid percolation pressures and the wetted areas for one test of each flow rate are combined. Only the data in the range of BOP^l-EOP^l are included. Tests at injection rates of $0.025\,mm^3/s$ and $0.0066\,mm^3/s$ show some wicking of the liquid before the sudden jump in the percolation pressure, and that is why the wetted area does not start from zero. Figure 4.8 shows the detected area

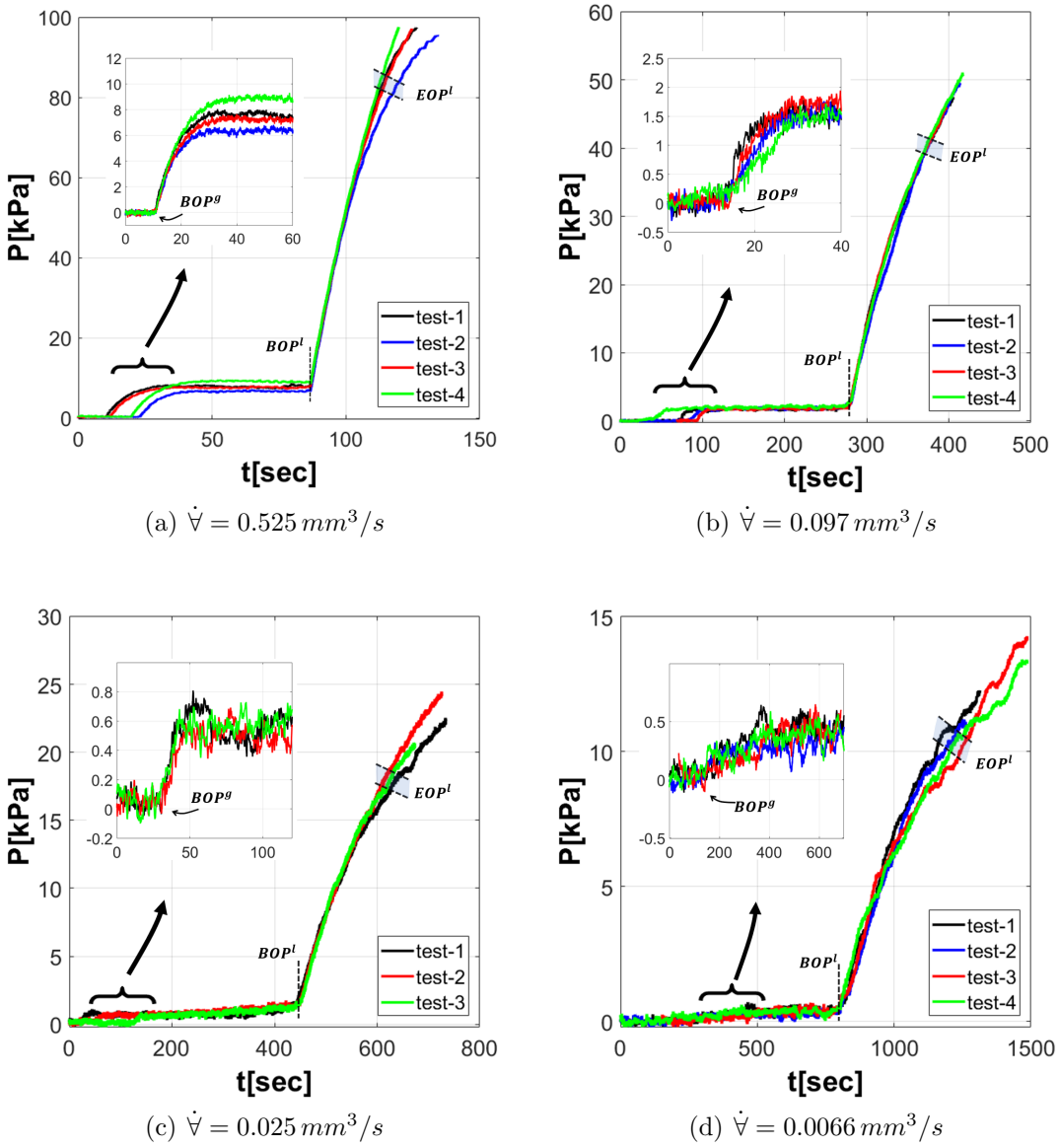

(a) $\dot{\forall} = 0.525\, mm^3/s$

(b) $\dot{\forall} = 0.097\, mm^3/s$

(c) $\dot{\forall} = 0.025\, mm^3/s$

(d) $\dot{\forall} = 0.0066\, mm^3/s$

Figure 4.6: EW825 tested three to four times for each flow rate, to confirm data repeatability when the condition is fixed. The main figures include raw data, gas then liquid percolation pressure, which are shifted to overlap the BOP^l of the repeated tests. The Sub-Figures are the percolation pressure for the gas. The ambient conditions where the tests are conducted: $22 - 25\,^{\circ}C$ and $17 - 20\,\%$.

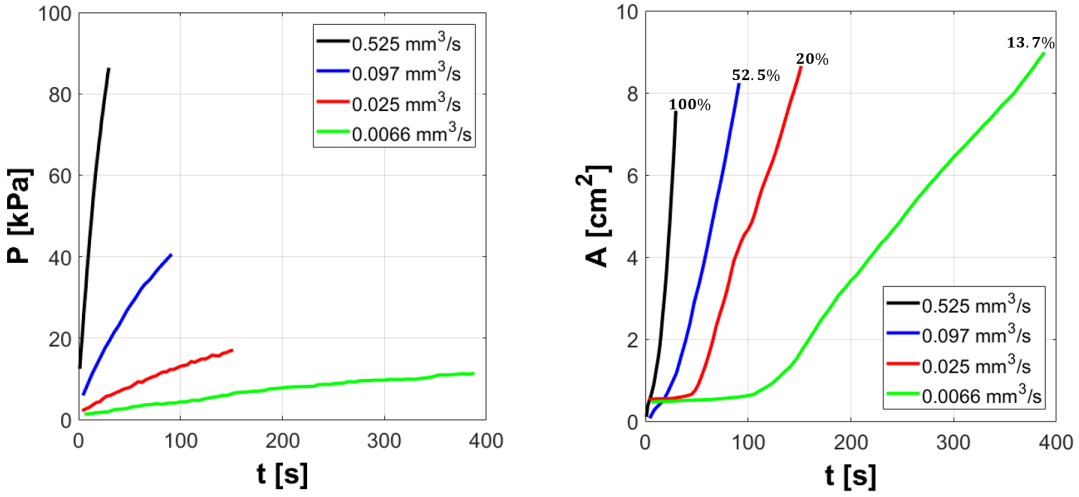

(a) Percolation Pressure

(b) Wetted Area

Figure 4.7: The tests results of EW825 includes the data in the range of BOP^l-EOP^l, where (a) is the percolation pressure at different injection rates, and (b) is the coincided wetted area. The tests condition is $22-25\,^{\circ}C$ and $17\%-20\%$ of RH.

of the liquid EW825 at different times until the end of percolation for each injection rate.

At high injection rates, $0.525\,mm^3/s$ and $0.097\,mm^3/s$, the viscous effect is clearly dominant throughout the entire percolation pressure, as the pressure keeps increasing during the entire test, BOP^l to the EOP^l. This implies that the fluids flow through the bulk of the pores, and the liquid front takes a shape of circle as shown in Figure 4.8(a) and 4.8(b) with a sharp edges compared to lower injection rates. At the lower injection rates, specifically $0.0066\,mm^3/s$, the percolation pressure of FC-3283 shows a preferential flow path in which the pressure levels off at low injection rates as shown in Figure 4.7(a). The captured wetted area is also takes a circular shape, but with a small fingers at the edges as shown in Figure 4.8(c) and 4.8(d). The wetted area for the flow rate test $0.0066\,mm^3/s$ at the EOP^l, as shown in Figure 4.7(b), is higher

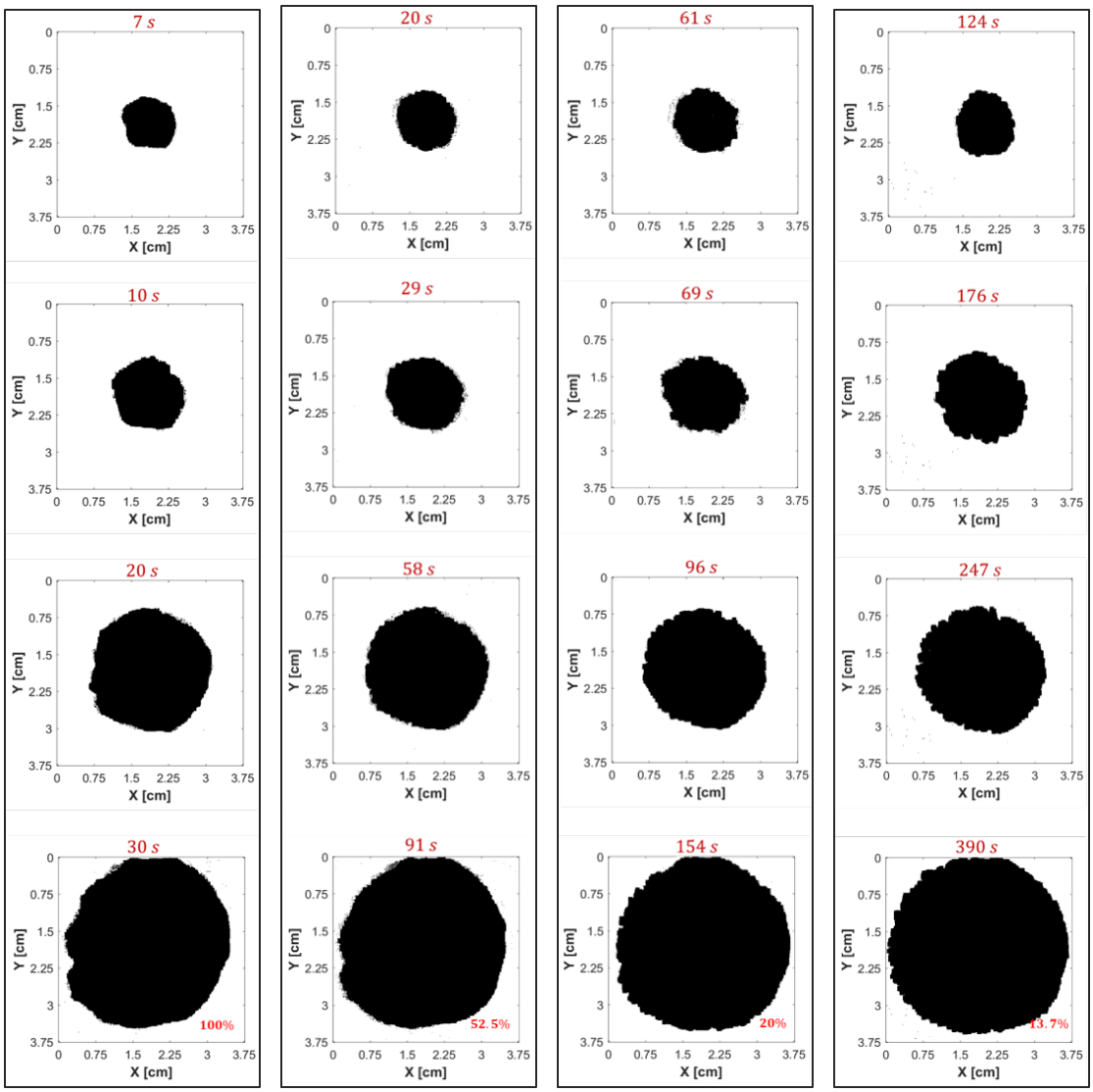

(a) $\dot{\forall} = 0.525\, mm^3/s$ (b) $\dot{\forall} = 0.097\, mm^3/s$ (c) $\dot{\forall} = 0.025\, mm^3/s$ (d) $\dot{\forall} = 0.0066\, mm^3/s$

Figure 4.8: A detected transient wetted area of EW825 at different injection rates.

than other flow rates tests, which is unexpected based on imbibition [59].

4.5.2 Effective Saturation at EOP^l

To understand the discrepancy in the wetted area shown in Figure 4.7(b), the effective saturation for each injection rate is determined with respect to highest flow rate test, $0.525\,mm^3/s$ using equation 4.1 and 4.2. Effective saturation is based on two assumptions, which are, first, assuming no changes in the CL porosity with respect to flow rate. Second, all the permeable pores during the test $0.525\,mm^3/s$ are assumed to be filled with liquid phase in the wetted area calculation.

$$\forall = \dot{\forall} \times t_{EOP^l} \tag{4.1}$$

$$s_e = \frac{(\forall / A_{EOP^l})}{(\forall / A_{EOP^l})_{max}} \tag{4.2}$$

Here $\forall$ is the total injected volume, $\dot{\forall}$ is the injection rate, t_{EOP^l} is the percolation time at the EOP^l, A_{EOP^l} is the wetted area at the end of percolation, and s_e is the effective saturation of the liquid phase. The term $(\forall / A_{EOP^l})$ represents the distribution of liquid volume per unit area at any injection rate. Table 4.3 shows $\forall$ and s_e for each flow rate. At low injection rate, although the captured wetted area is the largest, Low $\forall$ and s_e is obtained. This is back to the heterogeneous structure of the CL which playing a role in the liquid percolation. These calculations assume that FC-3283 is percolating along the surface roughness of the secondary pores, which is constructed from the agglomerate and the binder of of the ionomer films [104, 105]. In addition, the FC-3283 has preferential to flow throughout some pores and leave other pores

with the gas phase (N_2) trapped. For the high injection rate the liquid phase invades most of the pores and high saturation observed, though less wetted area is measured. The calculated s_e values are marked at the end of the corresponding wetted area curves as shown in Figure 4.7(b)

The consistent percolation pressures for each injection rate indicate that there is no significant changes in the structure of the CL [90] when the RH condition remains constant. This observation was necessary for the next type of testing where changes are expected in the gas/liquid percolation pressure for the same injection rate when the CL is conditioned at different RH.

Table 4.3
Liquid saturation calculation at the EOP^l for sample EW825.

flow rate, $\dot{\forall}$ (mm^3/s)	0.525	0.097	0.025	0.0066
t_{EOP^l} (s)	30	91	154	390
A_{EOP^l} (cm^2)	7.7	8.24	9.46	9.15
volume, $\forall(mm^3)$	15.75	8.86	3.84	2.57
effective saturation, s_e (%)	100.0	52.5	20	13.7

4.6 Effect of RH Conditioning on Percolation

EW725 was tested at a constant injection rate of $0.025\,mm^3/s$, but different RH conditioning as shown in Figure 4.5. The results show that increasing RH during the conditioning process leads to a significant increase in the percolation pressure for both N_2 and FC-3283 phases as shown in Figure 4.9. The increase in percolation pressure is due to the retained water vapor by ionomer films. Since the CL is confined between

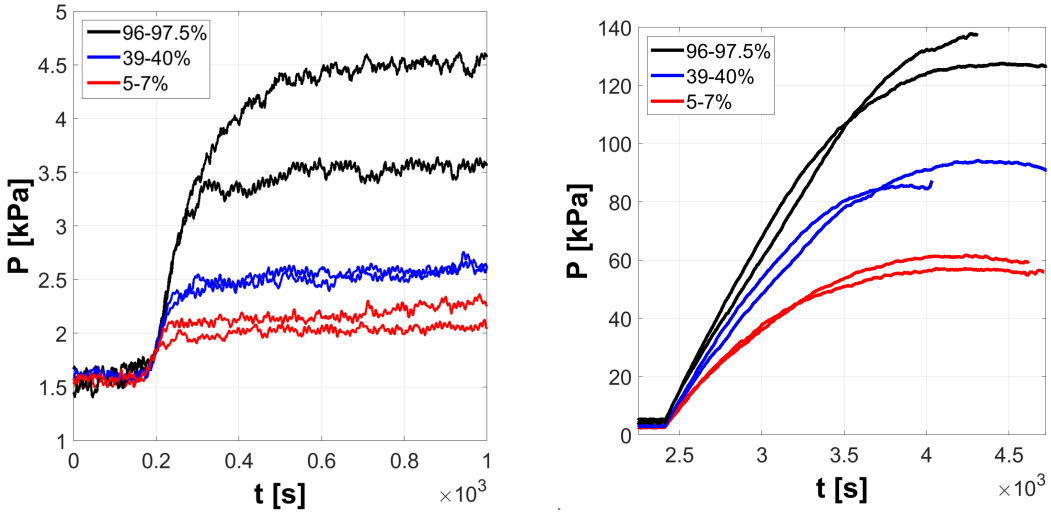

(a) Percolation Pressure of Humidified N_2 (b) Percolation Pressure of FC-3283

Figure 4.9: RH effect on the percolation pressure throughout EW725 for both, (a) gas (N_2) and (b) liquid (FC-3283) at constant injection rate of $0.025\,mm^3/s$, but different RH conditions.

platens, any swelling in the ionomer films is at the expense of mean pore size. The maximum steady pressure of the N_2 and the breakthrough pressure (EOP^l) of the FC-3283 at each RH condition are combined in Figure 4.10(a). The results show that the increase in the percolation pressure is more likely realted to the increase in the water content (λ) and the hygroexpansion ($\Delta L/L$) in the ionomer films [4], which has the same chemistry of the ionmer in the tested sample (EW725), as shown in Figure 4.10(b).

The data of the FC-3283 in the range of BOP^l-EOP^l for pressure and the corresponding wetted area are shown in Figure 4.11. For all tests, there is a continuous increase in the percolation pressure, which means the viscous effect is dominant and FC-3283 percolate through the bulk of the pores. The wetted areas at the EOP^l for the tests of less than 40% RH, as in Figure 4.11(b), show minor variation, while it is higher for the tests of 96% to 97.5% RH. The tests that are conditioned at high RH, 96 to

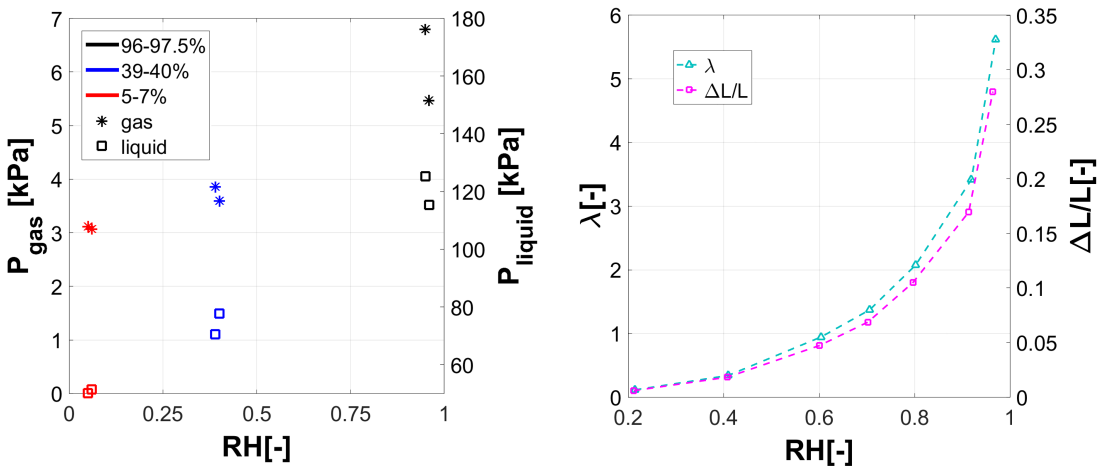

(a) Pressure at EOP^l

(b) Water Content

Figure 4.10: (a) Maximum Percolation pressure of the gas and the pressure of the liquid at the breakthrough, EOP^l. (b) RH effect on the water content(λ) and the hygroexpansion (ΔL/L) of a 15 nm thick PFSA EW725 ionomer [4].

97.5%, show unexpected results of a longer percolation time than other tests which are conditioned at low RH, 5% to 40%, though, in previous testing for a smaller sample size of $3.81 \times 3.81\, cm^2$ the percolation time was less for high RH condition [90]. High RH conditioning results in smaller mean pore sizes as the ionomer films swells. For a constant injection rate, less time is expected for the liquid to reach the EOP^l, yet the results of the current study show the opposite. This is likely related to the sample size, where the resistance to flow increases in the radial direction and that force the liquid to invade most of the neighbor pores instead of the one in the radial direction. In addition, the gas-liquid interface length increases in the radial direction which allows more liquid to evaporate and that could slow down the liquid to reach the EOP^l. The rate of evaporation was measured by flooding EW725 with FC-3283 and left to evaporate. Figure 4.12 shows the evaporation rate, which can

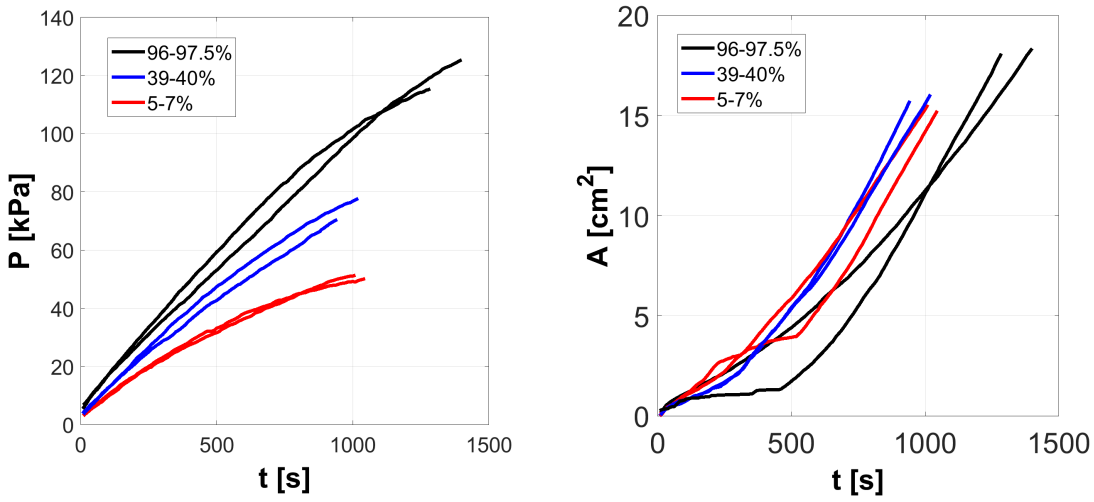

(a) Percolation Pressure

(b) Wetted Area

Figure 4.11: Liquid percolation through EW725 conditioned at different RH in the range of BOP^l to EOP^l. (a) Transient percolation pressure curves. (b) Corresponding wetted area Curves.

become significant when the liquid front is near the edge of the sample.

4.6.1 Permeability and Relative Humidity

Permeability is a measure of a porous medium to transmit fluid, so it is considered a dynamic property that is only characterized by conducting a flow experiment. There are many methods to estimate the permeability, some of them could be used to measure the permeability of the CL. For example, Washburn method estimates the permeability based on spontaneous imbibition flow [106]. The Washburn method is measures effective permeability instead of absolute because the driving force is capillarity, where many pores that offer low capillary force (imbibition) will be left filled with the gas phase. Another method to measure the permeability is the steady

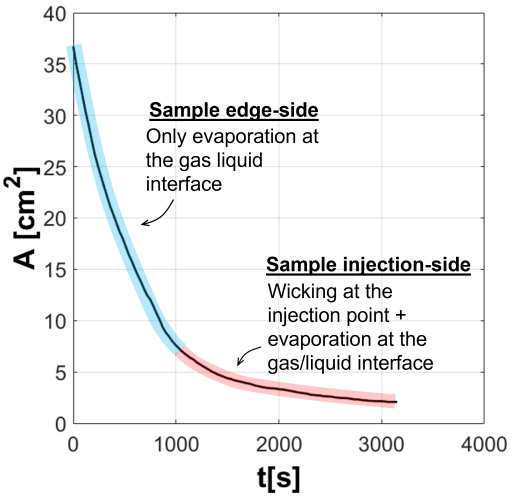

Figure 4.12: Evaporation rate for EW725 conditioned at an RH of 50% and 22 °C. Liquid front retracts into the sample with time.

state method using Darcy equation. The measurement is done at high flow rate (capillarity is negligible) to enforce fluid invation of all permeable pores until reaching a steady state.

In this study, Permeability is determined using steady-state condition for radial flow, equation 4.3,

$$\kappa_{r2} = \frac{\mu \, ln(r_2/r_1) \, \dot{\forall}}{2 \, \pi \, h \, \Delta P} \tag{4.3}$$

where h is the thickness of the catalyst layer, which was measured at 12.5 μm based on SEM imaging (see Figure 4.3). κ_{r_2} is the radial permeability, which measured when the percolation pressure reached to a steady state. ΔP is the pressure difference corresponding to post end-of-percolation (steady), μ is viscosity, and r_1 is the radius of the hole where the liquid injected (1 mm). In case of the gas N_2, r_2 taken as $w/2$,

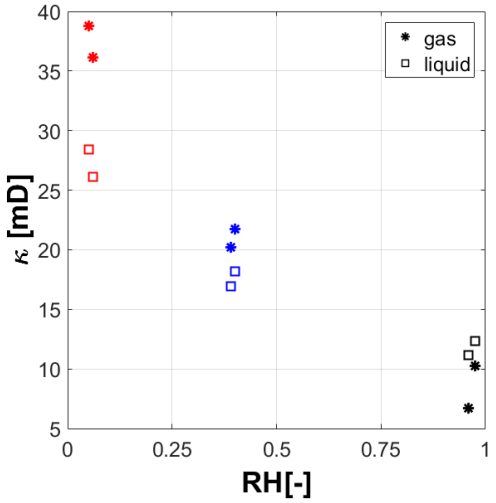

Figure 4.13: The permeability is calculated for sample EW725 based on post end-of-percolation pressure of gas and liquid.

where w is the sample width. For liquid FC-3283 , r_2 estimated based on the wetted area using the formula $r_2 = \sqrt{A/\pi}$. Permeability is calculated based on the steady pressure for both gas and liquid. Figure 4.13 shows that the swelling of ionomer films has a significant impact on flow conductance. As RH increases the radial permeability decreases.

Percolation pressure at post-end-of-percolation testing when pressures are steady increases linearly with RH at constant volumetric flow rates, as shown in Figure 4.14. Equation 4.3 is re-organized as:

$$\Delta P = \underbrace{\frac{\mu \ln(r_2/r_1)\dot{\forall}}{2\pi h}}_{\text{constant wrt RH}} \frac{1}{\kappa_{r_2}} \tag{4.4}$$

All terms in equation 4.4 are constant with respect to relative humidity except for the radial permeability, κ_{r_2}. Therefore, since ΔP increases linearly with RH, the inverse

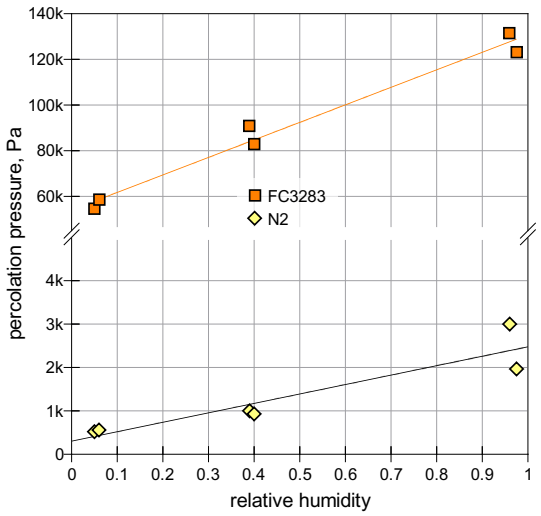

Figure 4.14: Steady percolation pressure at the post end-of-percolation for both gas (N_2) and liquid (FC-3283) versus RH for sample EW725.

of radial permeability must also linearly increase with increasing RH. Expressing this as a linear regression,

$$\frac{1}{\kappa_{r_2}} = \frac{1}{\kappa_0}\left(a_0 + a_1 \mathrm{RH}\right) \qquad \Longleftrightarrow \qquad \kappa_{r_2} = \kappa_0 \left(\frac{1}{a_0 + a_1 \mathrm{RH}}\right) \tag{4.5}$$

where κ_0 is a reference permeability. As shown in Figure 4.13, the minimum value of radial permeability occurs at $RH = 1$. Therefore,

$$\kappa_0 = \kappa_{\min}(a_0 + a_1) = \kappa_{\max} \tag{4.6}$$

Substituting for κ_0,

$$\frac{1}{\kappa_{r_2}} = \frac{1}{\kappa_{\min}} \left(\frac{a_0 + a_1 \, \mathrm{RH}}{a_0 + a_1} \right) \quad \Longleftrightarrow \quad \kappa_{r_2} = \kappa_{\min} \left(\frac{a_0 + a_1}{a_0 + a_1 \, \mathrm{RH}} \right) \tag{4.7}$$

Alternatively,

$$\kappa_{r_2} = \kappa_{\min} \left(\frac{1 + \beta}{1 + \beta \, \mathrm{RH}} \right) \tag{4.8}$$

where $\beta = a_1/a_0$. There are a variety of options for determining the correlation constants. One option is to combine parameters for the left-most expression in equation 4.7 and use linear regression on $1/\kappa_{r_2}$. Another option is to perform a non-linear regression on equation 4.8. Through trial-and-error, the regression with the smallest error with this set of data is the latter (equation 4.8). Both the linear and non-linear regressions are shown in Figure 4.15.

	N_2 (gas)	FC-3283 (liquid)
$\kappa_{\min}$	10.28±0.044	11.17±0.053
β	3.346±0.266	1.65±0.18
$\kappa_{\max}$	44.68	29.6

The data of λ versus RH was extracted from the work of Shrivastava et al. [4] so there is some uncertainty in the values, particularly at low values of RH. Normalizing the extracted data using equation 4.9 results in the linear trend shown in Figure 4.16(a).

$$\left(\frac{\mathrm{RH} - \mathrm{RH}_{\max}}{\lambda - \lambda_{\max}} \right) = a_0 + a_1 \, \mathrm{RH} \tag{4.9}$$

In this process, it is assumed $\mathrm{RH}_{\max} = 1$ and $\lambda_{\max} = 7$. The latter is a rough estimate

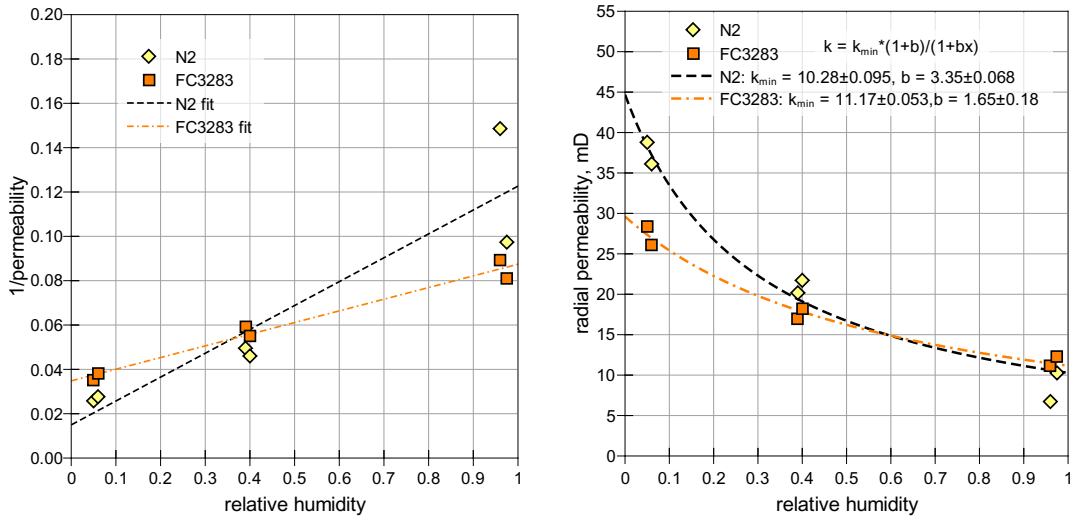

(a) Linear regression of $1/\kappa_{r_2}$.

(b) Nonlinear regression of κ_{r_2}.

Figure 4.15: Linear (eq. 4.7) and nonlinear (eq. 4.8) regressions of relative permeability versus RH.

based on data trends.

The functional form of λ = f(RH) that results in the linear trend shown in Figure 4.16(a) is:

$$\lambda = \frac{\mathrm{RH}}{b_0 + b_1\,\mathrm{RH}} + b_3 \tag{4.10}$$

At RH = 0, λ is presumed to be 0 so that $b_3 = 0$. The relationship between the a-coefficients in the linear regression (eq. 4.9) and the b-coefficients in the functional form (eq. 4.10) is:

$$b_1 = \frac{a_0 a_1}{a_0 + a_1} \quad \text{– and –} \quad b_0 = a_0 - b_1 \tag{4.11}$$

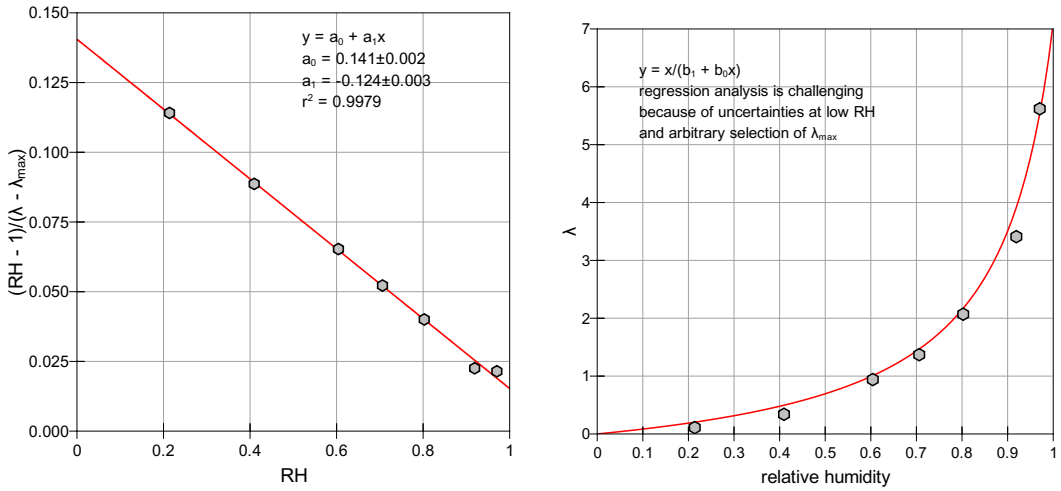

(a) Linear regression of $\frac{\mathrm{RH}-\mathrm{RH}_{\max}}{\lambda-\lambda_{\max}}$.

(b) $\lambda = \mathrm{f}(\mathrm{RH})$.

Figure 4.16: λ and RH for PFSA ionomer film at 30 °C [4]. (a) Linear regression of normalized data. (b) $\lambda = \mathrm{f}(\mathrm{RH})$ data and equation 4.10 with $b_0 = 1.299$ and $b_1 = -1.158$.

linear regression, equation 4.9	functional form, equation 4.10
$a_0 = 0.1405 \pm 0.0018$	$b_0 = 1.299$
$a_1 = -0.1253 \pm 0.0026$	$b_1 = -1.158$
$r^2 = 0.9997$	

Figure 4.16(b) is a plot of equation 4.10 using the b-coefficients that is superimposed on the original data.

A correlation between radial permeability, κ_{r_2} and λ can be derived using the correlations for $\kappa_{r_2} = \mathrm{f}(\mathrm{RH})$ (equation 4.8) and $\mathrm{RH} = \mathrm{f}(\lambda)$ (equation 4.10).

$$\kappa_{r_2} = \kappa_{\min}\,(1+\beta)\left[\frac{1-b_1\lambda}{1-(b_1-\beta b_0)\lambda}\right] \tag{4.12}$$

The resulting expression for N_2 is equation 4.13 and FC-3283 is equation 4.14.

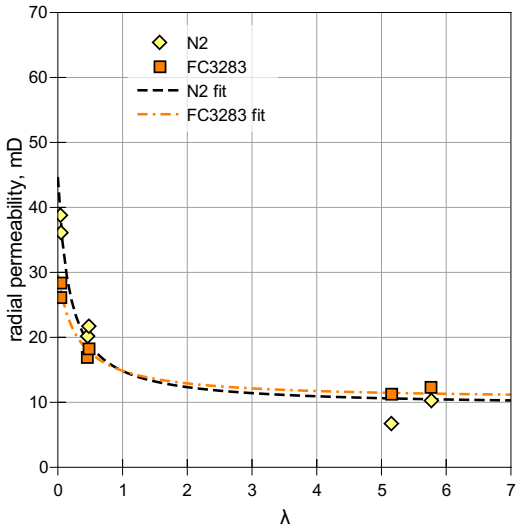

Figure 4.17: Permeability dependency on λ for a catalyst layer with PFSA ionomer.

$$\kappa_{r_2} = 44.7 \left(\frac{1 + 1.16\lambda}{1 + 5.5\lambda} \right) \tag{4.13}$$

$$\kappa_{r_2} = 29.6 \left(\frac{1 + 1.16\lambda}{1 + 3.3\lambda} \right) \tag{4.14}$$

Figure 4.17 plots these two relationships against the original percolation test data showing in Figure 4.15(b). There is a sharp decrease in radial permeability at low values of λ, but κ_{r_2} is relatively insensitive for $\lambda > 3$. This is in contrast to Figure 4.15 in which there is a continuous decrease in κ_{r_2} with increasing RH.

4.7 Conclusions

A Hele-Shaw setup is adapted to study two-phase flow in a thin porous catalyst layer. The consistent results of the percolation tests at constant RH condition provide confidence in the setup and makes a useful tool for testing thin porous materials.

The calculations of effective saturation for the percolation results at constant RH condition suggest that FC-3283 imbibes along the surface of the pores when the flow rate is low (capillarity is dominant) leaving most of the pores filled with the gas phase (high trapped saturation of the gas). As the flow rate increases, FC-3283 invades most of the pores (minimum trapped gas). These flow regimes are likely related to the morphology and roughness of the secondary pore surface.

The permeability calculations at constant flow rate, suggests that there is considerable impacts in the mass transport in the CL as the RH increases. Furthermore, the derived correlation between the permeability and the water content λ shows that the considerable impacts to the mass transport occurs at $\lambda < 3$, and beyond this value, there is no significant change in the permeability. In other words, for $\lambda > 3$ the mass transport in the catalyst layer pores is constant.

Chapter 5

Ionomer Impact on Structure and Wettability of PEM Fuel Cell Catalyst Layer

Percolation testing and contact angle measurements have been used to investigate the role of relative humidity (RH) on structure, mass transport, and wettability of a PEM fuel cell catalyst layer and membrane. Four samples were tested, two catalyst layers and two membranes. Structure and mass transport changes in the catalyst layers resulting from RH changes were studied in terms of percolation pressure. A clear change in the structure between low and high RH conditioning was observed. RH cycling also impacted percolation pressures with an indication of catalyst layer cracking. In addition, RH effect on wettability of both catalyst layers and membranes were studied by measuring contact angles of sessile drops where the results indicates a morphological changes.

5.1 Introduction

Ionomer in the catalyst layer form nano-scale thin films [73, 107] that often have the same chemistry as the much thicker electrolyte membranes, though a distinctive difference in properties such as water uptake and conductivity are observed [4, 108]. The chemical structure of the ionomer consists of hydrophilic sulfonic group clusters that work as a protonic path, which are connected by a side chain to a hydrophobic fluorocarbon backbone that keeps the ionomer both mechanically and chemically stable [31, 109]. Transport properties of the ionomer are affected by hydration [4, 85, 110]. Both thin ($7nm$ [73]) and thick ($> 10\mu m$ [111, 112]) ionomer films interact with vapor to alter the orientation of sulfonic acid side chains [31, 32]. This affects wettability and conductivity in the ionomer films [113, 114].

The ionic domains in the ionomer retains water, where the number of water molecules per sulfonic acid group can reach up to 8 as in ionomer thin films in the catalyst layer [4], and 15 in electrolyte membrane [5, 112] when saturated with vapor. Thus, the pore size distribution of a catalyst layer may be shifted towards a lower average effective radius as the ionomer swells [29, 88]. This will have an impact on reactant transport resistances [67, 69, 71]. Cycling the relative humidity of the catalyst layer results in the absorption/release of water to/from ionomer films, which in turn leads to structural stresses and potential defect (crack) growth [30].

The ionomer films effects on the structure, flow regimes, and wettability are investigated over a range of RH conditions. The structure and flow regime are studied in term of percolation pressure, injected fluid wetted area, and perimeter of fluid-fluid

interface using percolation setup. While the wettability is studied in term of contact angle (CA) measurements using sessile drop method.

5.2 Percolating Testing

This is a summary of percolation test results detailed in chapter 4. Two catalyst layers, as in Table 5.1, with equivalent weights (EW) of 725 and 825 (provided by 3M) were tested over a range of RH conditioning at room temperature ($22 - 25°C$). Samples were conditioned at low (9%) and high (92% to 98%) RH for up to three hours. Pertinent material properties for the catalyst layers are listed in Table 5.2. EW725 and EW825 refer to the catalyst layers with EW of 725 and 825, respectively. The ionomer-to-carbon (I/C) ratio for EW725 and EW825 are 0.8 and 0.9, respectively, and EW725 does not include any platinum catalyst.

Table 5.1
Samples specifications.

Sample	**Pt-Loading** ($mg/cm2$)	**EW**	I/C
EW725	–	725	0.8
EW825	0.19	825	0.9

Table 5.2
The conditions for each test.

Sample	**Size** (cm^2)	**RH Conditioning**	**Flow Rate** $\mathbf{mm^3/s}$
EW725	3.81×3.81	9%	0.0066
EW725		95%	
EW825		9%	
EW825		92%	

5.3 Contact Angle Measurements

Wettability of the catalyst layers EW725 and EW825 as well as electrolyte membranes with the same chemistry and EW, PEM825 and PEM825, respectively, was measured using the sessile drop method. Drop profile images were measured using a long working distance microscope paired with a CCD camera and a uniform backlight as shown in Figure 5.1. Consistent, accurate, and repeatable drop sizes were deposited using a precision threaded syringe (Hamilton 1750TPLT) in which one plunger rotation is equivalent to 5.27 μL.

Catalyst layer and membrane samples were conditioned by first drying in a desiccator for two days. Samples were then placed into a sealed chamber that enclosed the sample platform. Humidified air flowed through the chamber for a minimum of 60 minutes before drop deposition to ensure constant humidity conditions. The exception was

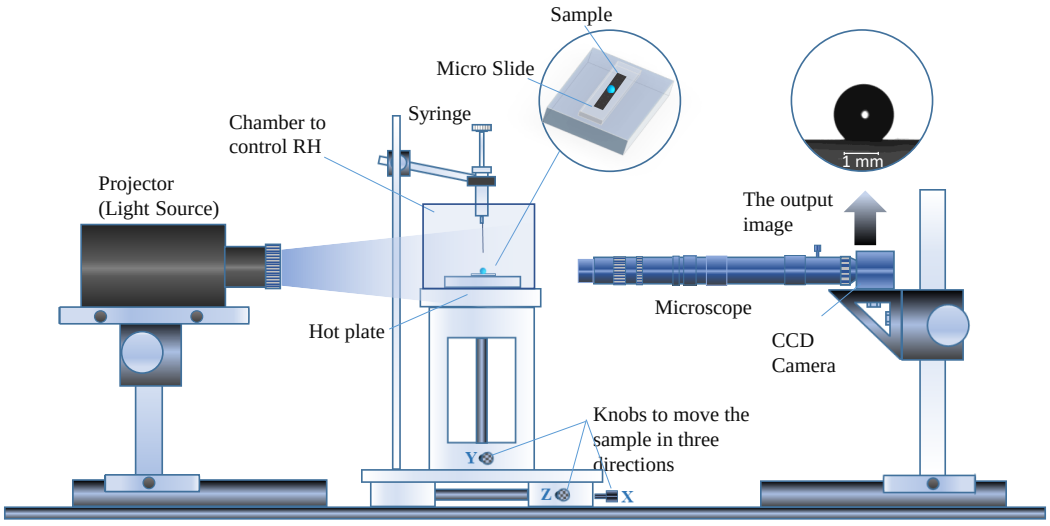

Figure 5.1: Experimental setup of sessile drop method for CA measurements.

the 0% RH samples that did not use conditioned air circulation. RH measurements were the same as for percolation testing (section 4.4). After conditioning, multiple drops of deionized water were placed on the catalyst layer or membrane surface and imaged.

Contact angles were determined by fitting a Laplace curve to the drop profile, then intersecting the curve at the substrate location. The static contact angle is determined by the value of the Laplace curve at the intersection. For each measurement, a minimum of three independent images were captured within 5 seconds to minimize effects of evaporation. The reported contact angle is the average of the three contact angles and uncertainty is related to the standard deviation.

The rough, heterogeneous surfaces of catalyst layers results in a drop size dependence of the measured contact angle [115, 116]. Therefore, drop deposition volume was carefully controlled for consistency with $3.96\,\mu L$ for catalyst layers and $1.32\,\mu L$ for membranes.

5.4 RH Effect on The CL Structure

Table 2 shows the details of the RH conditioning and percolation flow rate for each test. Transient percolation pressure changes dramatically with RH conditioning, indicating structural changes in the catalyst layer. Figure 5.2*a* shows percolation pressure at low (9%) and high (95%) RH conditioning for EW725. The injection rate of FC-3283 was $0.0066\,mm^3/s$ for all tests shown. The percolation pressure curve for EW725 at 9% condition levels off after approximately $2500\,s$, whereas the 95% test exhibits

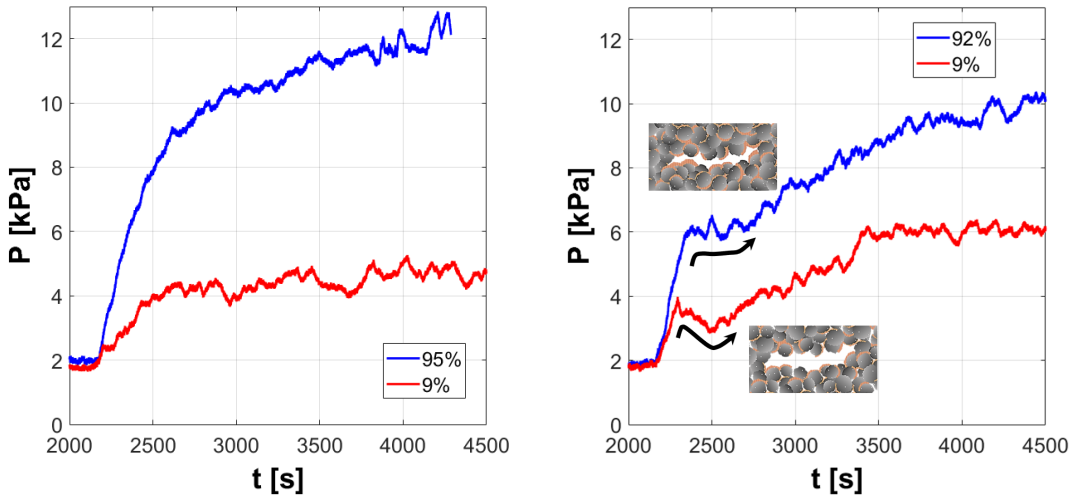

(a) EW725 (b) EW825

Figure 5.2: Percolation pressure at low and high RH conditioning at constant injection rate of $0.0066\,mm3/s$ for (a) EW725 and (b) EW825.

a continuous rise at much higher pressures. The difference in percolation pressure is likely due to ionomer swelling resulting in a smaller average pore size. The result is an increase in mass transport resistance within the catalyst layer at high RH conditioning. A similar effect is observed in EW825, which had a defect (crack) in the catalyst layer. The instant FC-3283 encountered this defect is easily detected in the transient percolation pressure as shown in Figure 5.2*b*. After the defect, or crack, fills, then the pressure curves exhibit a similar trend as for the EW725 sample.

Transient percolation pressure data in Figure 5.2*a* indicates that imbibition changes with RH conditioning. At 9% conditioning, the pressure curves exhibit a classic capillary fingering response and at 95% the pressure curves exhibit a stable displacement response [60]. In stable displacement, viscous effects dominate the advancing liquid front and liquid is invading most, if not all pores. For a fixed flow rate, the injection pressure continuous to increase as the liquid advances. In capillary fingering, at the

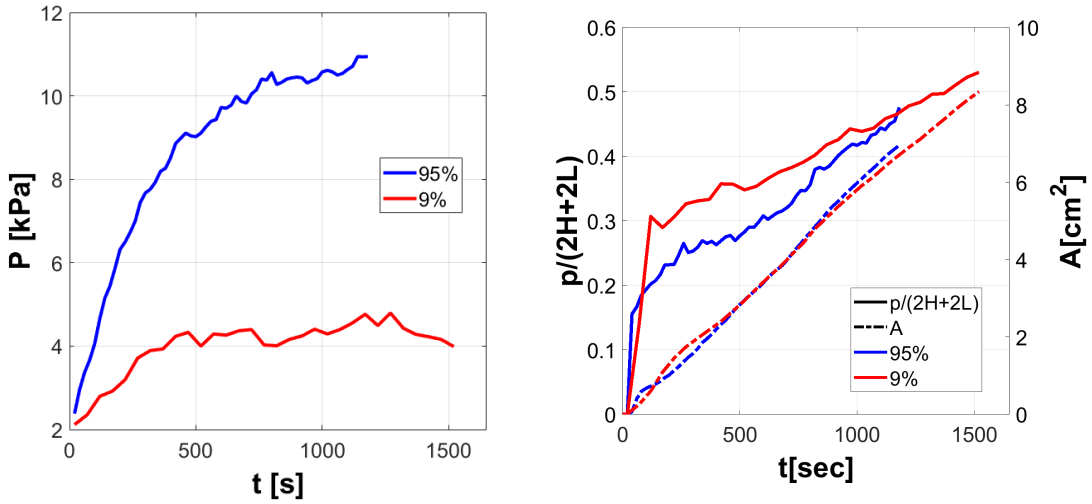

(a) Percolation Pressure (b) Wetted Area and Perimeter

Figure 5.3: The data include the BOP^l until the breakthrough (EOP^l). (a) Transient percolation pressure and (b) scaled wetted area and wetted perimeter for EW725 at an injection rate of $0.0066\,mm^3/s$. The perimeter of the wetted area, p, is scaled by the perimeter of the catalyst layer sample, 2H + 2L.

liquid-gas interface, fingers form at a constant percolation pressure. The stable displacement and capillary fingering response is reinforced in the imaging data. Figure 5.3*a* compares the injection pressure for EW725 at high and low RH conditioning with wetted area and perimeter data for the same tests in Figure 5.3*b*. The wetted area follows the same trend and is the same for high and low RH conditioning, which is expected for a constant rate of injection. The rate that the liquid advanced is not the same, with the 95% RH test ending earlier than the 9% RH test. A percolation test ends when liquid reaches the edge of the catalyst layer sample. The wetted area results are indicative of a smaller average pore size for the high RH sample as compared to the low RH sample. There is less overall void volume in the high RH sample, so at a constant rate of injection the test will end earlier.

The scaled perimeter (perimeter of the projected wetted area divided by perimeter

of sample) in Figure 5.3*b*, like the pressure response, indicates a difference in imbibition flow regime. A dry catalyst layer, such as the 9% RH sample, has a relatively large average pore size that more readily facilitates capillary fingering. In contrast, the relatively smaller average pore size of the wet catalyst layer (95% RH sample), resulting from the hypothesized ionomer swelling, increases the local viscous stresses at the advancing liquid-vapor interface resulting in stable displacement.

The hypothesized shift in average pore size due to ionomer swelling in the catalyst layer is supported by published data on ionomer water uptake. Figure 5.4 shows the water content, λ, of Nafion for thick membranes [5, 6] and for ultrathin ionomer films [4] with similar EW as EW725. As RH is increased, more water retained by hydrophilic sulfonic acid clusters in the ionomer, which results in internal structural changes. As RH decreases, absorbed water is released. Water uptake and release with RH is repeatable, but the cyclic effect on catalyst layer structure might not be.

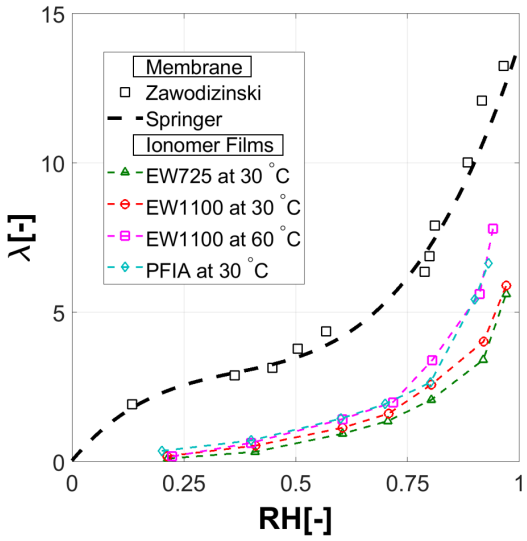

Figure 5.4: RH effect on the water content (λ) in the hydrophilic sulfonic acid side chain clusters for thick nafion membrane[5, 6] and ultra-thin ionomer films [4].

5.5 RH Effect on Wettability

Sessile drop contact angle measurements were conducted on catalyst layers (EW725 and EW825) and membranes (PEM725 and PEM825) for a range of RH conditioning, see Figure 5.5. For both catalyst layer and membrane samples the static contact angle increased then decreased with increasing RH conditioning. The lowest values of contact angle for the catalyst layers occurs at 0% RH conditioning. This is also where there is minimal difference between EW725 and EW825, less than 1° and within the measurement uncertainty.

For both catalyst layers, as RH increases from 0%, there is an immediate difference in static contact angle that can likely be attributed to the dispersed Pt catalyst particles present in the EW825 sample, as shown in Figure 5.5*a*, where the maximum static contact angle that occurs is approximately 50 to 60% RH. As RH is further increased the static contact angle decreases. The difference in the I/C ratio between the two catalyst layers does not appear to have any significant effect since the trends are the same.

Despite good repeatability, changes in static contact angle for the heterogeneous surfaces of these catalyst layers are difficult to explain. Based on preliminary results from laser surface profiling there is no measurable change in surface roughness ($0.29\,\mu m \pm 0.37$ for EW725, and $0.75\,\mu m \pm 0.93$ for EW825) with RH conditioning. Our hypothesis is sulfonic acid side chains become less exposed at the catalyst layer surface as the ionomer films take up additional water as RH conditioning increases. For RH conditions above $50\% - 60\%$, morphological alterations associated with the

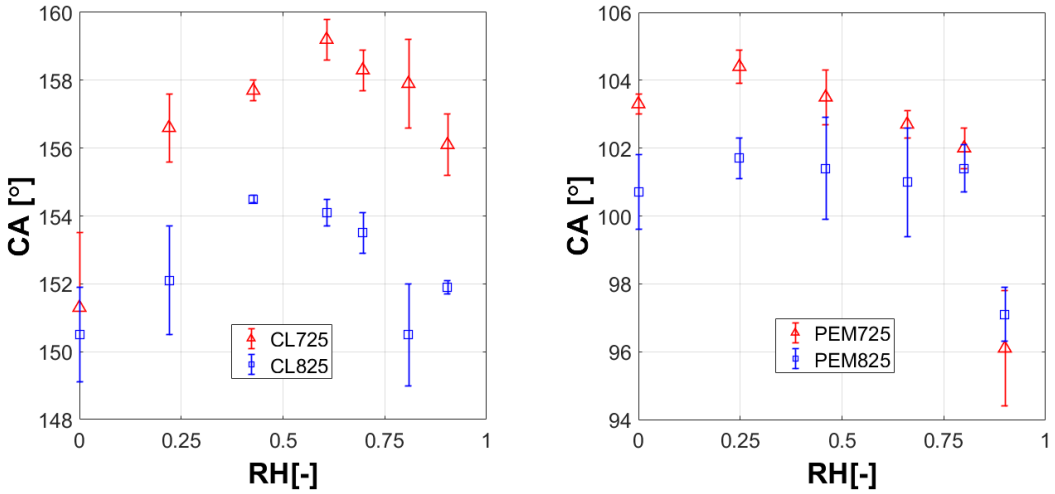

(a) Catalyst Layer

(b) Membrane

Figure 5.5: Static contact angles on (a) catalyst layer samples and (b) membranes for range of RH conditioning.

non-linear increase in water uptake, shown in Figure 5.4, a decreases in the catalyst layer surface hydrophobicity.

Figure 5.5*b* shows the static contact angle measurements for the membrane samples PEM725 and PEM825. The static contact angles are approximately 50° less than those on the catalyst layer. This is largely due to the absence of surface roughness on the membranes so there is no structural component to the contact angle measurement. There is a slight increase in static contact angle with increased RH conditioning from 0% to 25%. Unlike the catalyst layer samples, static contact angles are relatively constant with increased RH conditioning. The exception is at the highest RH of 90% for which an absorbed water film may have begun to form on the membrane surface. PEM725 exhibits overall larger contact angles as compared to PEM825, which was unexpected, though this is consistent with the results of water content in the ionomer

films shown in Figure 5.4. With higher EW there are less sulfonic acid groups (hydrophilic part) and less water content [117] [26]. There is a possibility of changes in the chemical structure orientation in the membrane similar to the observations of Bass et al. [31].

5.6 Conclusions

Changes in mass transport resistance and wettability of catalyst layers and membranes were studied using macroscopic observations of percolation and contact angle testing. Percolation pressure and liquid front dynamics for low and high RH conditioning indicate structural changes are occurring in the catalyst layer samples. These changes are significant enough to alter the imbibition flow regime for the same liquid injection rates. Static contact angle measurements on the catalyst layer membrane surfaces also indicate possible morphological changes.

Chapter 6

Computationally Efficient Model to Calculate Trapped Saturation in Porous Materials

The study of immiscible displacement inside porous media has a broad range of applications such as in oil recovery [13], hydrology [25, 118], and fuel cell technology [36, 53, 119–121]. During the immiscible displacement, a fraction of fluid can disconnect from the bulk volume and become trapped, surrounded by the second fluid, inside a subset of pores. The dimensionless volume of trapped fluid, defined as the ratio of the trapped volume to the total pore volume, is called irreducible or residual saturation depending on whether the trapped phase is wetting or non-wetting to the pore surface, respectively [122]. The importance and interpretation of these saturations vary from application to application. For example, in the oil industry, the interest is to recover the trapped oil in the reservoir, known as secondary oil recovery

[14]. In a fuel cell that operates at 80 °C residual saturation of water in the non-wetting porous transport layer should be minimized to facilitate reactant transport [18].

In this work, fractional flow theory (FFT) is adapted to study immiscible displacement of two-phase flow in a porous medium. The resulting model accurately predicts trapped saturation that occurs during imbibition and drainage of incompressible fluids for any capillary number. It also accurately predicts the fluid-fluid front displacement and critical capillary number at which trapped saturation begins to decrease. The unique aspect of this model is incorporation of a scaling factor, suggested by Médici and Allen [12], that captures the propensity for gas or liquid holdup for any porous media and fluid pair. The resulting simple, computationally efficient model is validated using experimentally measured saturation in Berea sandstone. The model accurately predicts trapped saturation and the critical capillary number for brine displacing oil (incompressible fluids) in Berea sandstone.

6.1 Drainage, Imbibition, and Trapped Saturation

Immiscible fluid displacement is categorized as drainage when the injected fluid is non-wetting to the pore surface, or imbibition when the injected fluid is wetting the pore surface [59]. The pore surface wettability causes a force to appear at the triple contact region between the fluid-fluid-solid interphases which is the capillary force [22]. The other force that appears during immiscible fluids displacement is due to the viscous stresses acting at the solid-fluid interphase, known as viscous force [123]. The relative effect of capillarity to viscous force on an immiscible fluid

displacement is captured by the capillary number, Ca $= \mu_i u_i/\sigma$, where μ_i and u_i are the viscosity and speed of the injected fluid, and σ is the surface tension. An additional dimensionless number used to characterize immiscible displacement is the viscosity ratio, $M = \mu_i/\mu_d$, where μ_d is the viscosity of the displaced fluid. At high Ca, the viscous force dominates over the capillary force and the resulting flow patterns are stable displacement or viscous fingering depending on whether M is greater or less than one, respectively. In contrast, at low Ca, the capillary force is dominant which results in the injected fluid to percolate through a subset of preferential pores that offer low capillary resistance [59, 60]. This flow pattern is called capillary fingering. For drainage capillary fingering, the pores that offer the lowest flow resistance are the largest. This preferential percolation path of the injected fluid can result in a portion of the displaced fluid to be trapped in the porous medium [124]. A thorough discussion of phase drainage diagrams has been published by Primkulov et al. [61].

The trapped saturation can occur due to the balance between the buoyant forces [23] or flow driving force [24]. These are trying to move a fluid while the capillary pressures resist these movements. Each component of capillary pressure, which are interfacial tension, pore size, and wettability can affect trapped saturation. For example, the trapped saturation of the wetting phase decreases with increasing the interfacial tension [125], and as the pores become narrower more gas or liquid can become trapped [23]. As the wettability decreases (uniform increase in the contact angle) there a minor increase in the trapped saturation is observed [126]. In contrast, for gas injection at a low flow rate, decreasing the wettability of the displaced liquid enhances the stability of immiscible invasion of the gas phase and reduces trapped saturation [127–129]. In addition, trapped saturation is effected by the degree of disorder of the pores [130], or the heterogeneity in the pore structure [126]. A porous

medium with a uniform pore size gradient will suppress capillary fingering pattern to stable displacement [131].

Experimental studies have investigated the relationship between capillary number and the resulting trapped saturation. The curve that is used to depict the relationship between capillary pressure and trapped saturation is called capillary desaturation curve (CDC) [132–135]. The CDC curve is obtained for different types of porous media, such as consolidated sandstone. The procedure starts by flooding the sample with oil, then water [9] or gas [8] is injected. Initially, fluid is at a capillary numbers less than 10^{-6} to assure a maximum trapped saturation of oil. Subsequent testing gradually increases the capillary number to establish the critical capillary number at which trapped saturation starts decreasing.

In this study, fractional flow theory is adapted to study the immiscible displacement of two-phase flow in porous media, where both the viscous and capillary effects are included in the formulation. A unique scaling is used to simplify the capillary term and the results in model can be used to estimate trapped saturation and study immiscible displacement of two phase flow in porous media.

6.2 Fractional Flow Theory

FFT model has been applied by many studies [136–140] to simulate the immiscible displacement in oil reservoir together with the continuity equation (Buckley-Leverett equation [7]). The model assumes a one-dimensional system with a uniform properties with two immiscible fluids. The fluids are assumed to be incompressible and each

phase occupies the volume in a pure state, i.e., there is no volume of mixed fluids (no dispersion). One more assumption in these studies is that capillary pressure is neglected. In this study, capillary pressure is considered.

6.2.1 Mass Balance

The starting point for the fractional flow theory is conservation of mass of two immiscible fluids in a porous medium, where the two phases are injected and displaced fluids, indexed with the letters i and d, respectively. Applying a mass balance to the injected fluid through a control volume (Δx, Δy, Δz), and a period of time Δt for the case shown in Figure 6.1.

$$\sum_{k=x,y,z} \Delta t(q_i\rho_i)_k - \sum_{k=x,y,z} \Delta t(q_i\rho_i)_{k+\Delta k} = \Delta x\,\Delta y\,\Delta z\,\varepsilon\left((s_i\,\rho_i)^{t+\Delta t} - (s_i\rho_i)^t\right) \qquad (6.1)$$

where k indicates the axis coordinate (x,y,z), q is the volumetric flow rate, ρ is the density, ε is the porosity of the medium, and s is the phase saturation. By assuming incompressible fluid flow and taking the limits of $\Delta k \to 0$ and $\Delta t \to 0$, equation 6.1

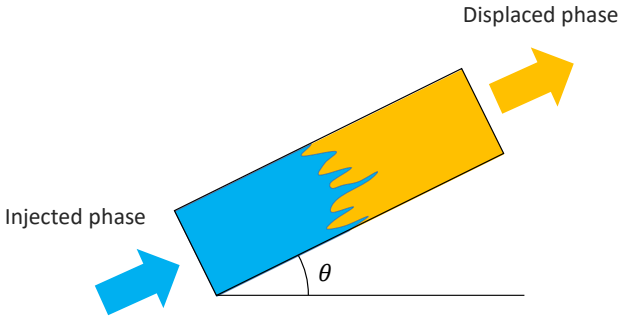

Figure 6.1: Immiscible displacement in a porous medium.

becomes:

$$-\nabla q_i'' = \varepsilon \frac{\partial s_i}{\partial t} \tag{6.2}$$

where q'' is flow rate per unit area.

The flow rate fraction for each phase is obtained by dividing phase flow rate to the total flow rate,

$$f_{i,d} = \frac{q_{i,d}''}{q_T''} \tag{6.3}$$

where the total flow rate, q_T'', at any cross section area in the porous media is given by:

$$q_T'' = q_i'' + q_d'' \tag{6.4}$$

Then, equation 6.4 can be written as:

$$1 = f_i + f_d \tag{6.5}$$

Equations 6.4 and 6.5 indicates that the total saturation for both phases is always equal to one, $s_i + s_d = 1$ [52]. For confined, 1D flow equations 6.2 and 6.3 can be written in terms of flow rate fraction of each phase.

$$-\frac{\partial f_i}{\partial x} = \frac{\varepsilon}{q_T''} \frac{\partial s_i}{\partial t} \tag{6.6}$$

$$-\frac{\partial f_d}{\partial x} = \frac{\varepsilon}{q_T''} \frac{\partial s_d}{\partial t} \tag{6.7}$$

6.2.2 Momentum Balance

The other governing equations are obtained from conservation of momentum, which results in a general Darcy equation for flow rate of each fluid.

$$q_i'' = -\frac{K_{ri}\,\kappa}{\mu_i}\left(\frac{dP_i}{dx} + \rho_i\, g \sin\theta\right) \tag{6.8}$$

$$q_d'' = -\frac{K_{rd}\,\kappa}{\mu_d}\left(\frac{dP_d}{dx} + \rho_d\, g \sin\theta\right) \tag{6.9}$$

Here, K_r is the relative permeability, κ is the absolute permeability, μ is the viscosity, P is the fluid pressure, g is the gravitational acceleration, and θ is the tilt angle relative to gravity as indicated in Figure 6.1.

At the immiscible fluid-fluid interface there is a pressure jump due to capillarity. A force balance is applied to relate the capillary pressure (P_c) with the injected-displaced fluids pressures.

$$P_i - P_d + \alpha P_c = 0 \tag{6.10}$$

where α is the direction of the capillary pressure based on the flow regime, imbibition or drainage. In case of wetting injected fluid (imbibition) the capillary pressure applies in the same direction of the injected fluid pressure, $\alpha = 1$; otherwise, the opposite is right, $\alpha = -1$, where the flow regime is drainage.

To relate the capillary pressure to the pressures of the injected and displaced fluids in the Darcy equations (6.8 and 6.9), the derivative is applied to equation 6.10 with

respect to x-direction,

$$\frac{dP_i}{dx} - \frac{dP_d}{dx} + \alpha \frac{dP_c}{dx} = 0 \tag{6.11}$$

Here, the wettability of each phase is considered constant throughout the porous media; i.e., α is constant.

Combining equations 6.3, 6.5 and 6.9 gives:

$$1 = f_i + \left[-\frac{K_{rd}\,\kappa}{\mu_d\, q''_T} \left(\frac{dP_d}{dx} - \rho_d\, g\, \sin(\theta) \right) \right] \tag{6.12}$$

By substituting equation 6.11 into equation 6.12,

$$1 = f_i + \left[-\frac{K_{rd}\,\kappa}{\mu_d\, q''_T} \left(\frac{dP_i}{dx} + \alpha \frac{dP_c}{dx} - \rho_d\, g\, \sin(\theta) \right) \right] \tag{6.13}$$

Combining equations 6.8 and 6.13 results in:

$$f_i = \frac{1}{1 + \frac{K_{rd}}{K_{ri}} \frac{\mu_i}{\mu_d}} \left[1 + \alpha\, \frac{K_{rd}\,\kappa}{\mu_d\, q''_T}\, \frac{dP_c}{dx} + \frac{K_{rd}\,\kappa}{\mu_d\, q''_T}\, (\rho_d - \rho_i)\, g \sin\theta \right] \tag{6.14}$$

Equation 6.14 is the general form of fractional flow theory. The capillary pressure and gravitational potentials on the right side of equation 6.14 are scaled by viscous effects. The solution to equation 6.14 requires knowledge of relative permeability for both fluid phases and knowledge of the capillary pressure gradient dP_c/dx.

6.3 Viscous Model

The general form of fractional flow, equation 6.14, is often simplified by neglecting gravitational effects ($\theta = 0$) and capillary effects ($\alpha = 0$). This simplified version is referred to as the viscous model.

$$f_i = \frac{1}{1 + \frac{K_{rd}}{K_{ri}} \frac{\mu_i}{\mu_d}} \tag{6.15}$$

Since relative permeabilities of the injected and displaced fluid, K_{ri} and K_{rd}, are functions of saturation [2, 3], the fractional flow function, f_i, is also a function of saturation.

Saturation of the injected fluid, s_i, changes with location (x) and time (t) so that the derivative is:

$$ds_i = \frac{\partial s_i}{\partial x} dx + \frac{\partial s_i}{\partial t} dt \tag{6.16}$$

The viscous model assumes a constant saturation at the moving fluid-fluid interface such that $ds_i|_{\text{front}} = 0$. Combining equations 6.6 and 6.16 provides an expression for the speed of the moving fluid-fluid interface.

$$\int \left. \frac{dx}{dt} \right|_{\text{front}} dt = \frac{q''_T}{\varepsilon} \frac{df_i}{ds_i} \int dt \tag{6.17}$$

Equation 6.17 shows that the front advance speed, dx/dt, depends on the derivative of fractional flow function with respect to saturation. By integrating, the front location (x) at any time (t) is obtained.

$$x = \frac{q''_T}{\varepsilon} \frac{d}{ds_i} \left(\frac{1}{1 + \frac{K_{rd}}{K_{ri}} \frac{\mu_i}{\mu_d}} \right) \Delta t \tag{6.18}$$

Equations 6.15, 6.17, and 6.18 solve for the flow rate fraction, fluid-fluid interface speed, and interface location, respectively, provided relative permeabilities (K_{ri}, K_{rd}) are known.

6.3.1 Relative Permeability Correlations

There are numerous correlations for relative permeability in which the working fluids are water (brine), non-aqueous liquid phase (NALP) (such as oil), and gas. In general, water is a wetting phase and gas is a non-wetting phase while NALP wettability depends on the second fluid wettability [3, 10]. This study deals with two flow regimes, drainage and imbibition. All correlations will be written in terms of the injected fluid saturation regardless to the wettability.

Brooks and Corey [2] derived a generalized empirical relationship for relative permeability based on a characteristic constant related to the pore-size distribution, ξ.

$$Kr_i = {s_e}^{(2+3\xi)/\xi} \tag{6.19}$$

$$Kr_d = (1 - s_e)^2(1 - s_e{}^{(2+\xi)/\xi}) \tag{6.20}$$

s_e is the effective saturation which is related to s_i by equation 6.21:

$$s_e = \frac{s_i - s_r}{1 - s_r} \tag{6.21}$$

where s_r is the residual saturation. s_r represents the end-point of the relative permeability curves that is estimated using steady state method at high injection rate so as to eliminate boundary effects due capillary discontinuity [141] and obtain a specific value of s_r [142]. Relative permeabilities are considered independent of fluid-flow rate [143–145].

A generalized correlation of the relative permeabilities were applicable for three-phase flow also derived by Parker et al. [3]. These correlations can be reduced to two-phase flow [3, 58] as:

$$Kr_i = s_e^{1/2}[1 - (1 - s_e^{1/m})^m]^2 \tag{6.22}$$

$$Kr_d = (1 - s_e)^{1/2}(1 - s_i{}^{1/m})^{2m} \tag{6.23}$$

where the parameter m is restricted to the range $0 < m < 1$.

The Brooks-Corey correlations (equations 6.19-6.21) are used to illustrate a typical dependency between relative permeability and saturation in Figure 6.2. In this

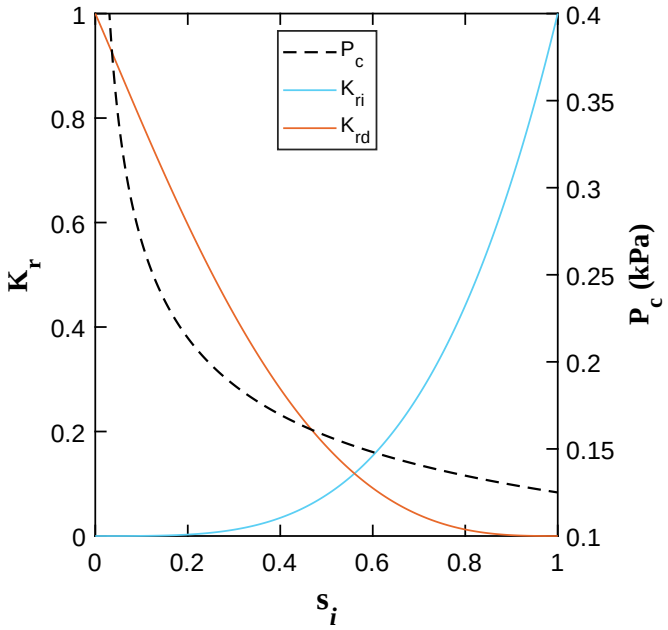

Figure 6.2: Relative permeabilities and capillary pressure dependence on saturation based on Brooks-Corey correlations [2] with $\xi = 3$, $s_r = 0$ and $P_b = 0.125\,kPa$.

analysis the value of ξ and s_r are assumed to be 3 and 0, respectively. However, the analysis described here are not limited to Brooks-Corey correlations or the assumed values of ξ and s_r. For drainage, where the injected fluid is the non-wetting phase, the correlations are rewritten in terms of the non-wetting phase saturation with $s_i = 1 - s_d$.

6.3.2 Viscous Model Results and Interpretation

The fractional flow function and its derivative are solved using parameters listed in Table 6.1 and the Brooks-Corey correlations (equations 6.19 and 6.20) with $\xi = 3$ and $s_r = 0$. Figure 6.3(b) shows the solution of equation 6.18 where the impossible

Table 6.1
Parameters values are assumed to apply the fractional flow model.

Constant	Value
absolute permeability (κ)	$500\, mDarcy$
injected fluid viscosity (μ_i)	$0.01\, Pa.s$
displaced fluid viscosity (μ_d)	$0.01, 0.001, 5.10^{-5}\, Pa.s$
porosity (ε)	0.3
surface tension (σ)	$0.025[N/m]$
mean pore size ($\bar{r}$)	$10\, \mu m$
$\Delta\rho$	$100\, kg/m^3$

situation of two saturation at each location is resolved by identifying the saturation at the front. This is done by drawing a tangent line from the initial condition to the curve of f_i satisfy the slope $(df_i/ds_i)_{\text{front}}$ in equation 6.24, then $(s_i)_{front}$ is identified as shown in Figure 6.3(a) [146]. Another method to define the front location is by applying a mass balance between areas, ahead of the front (A_1, part of it is not shown in Figure 6.3(b)) and behind the front (A_2) [7].

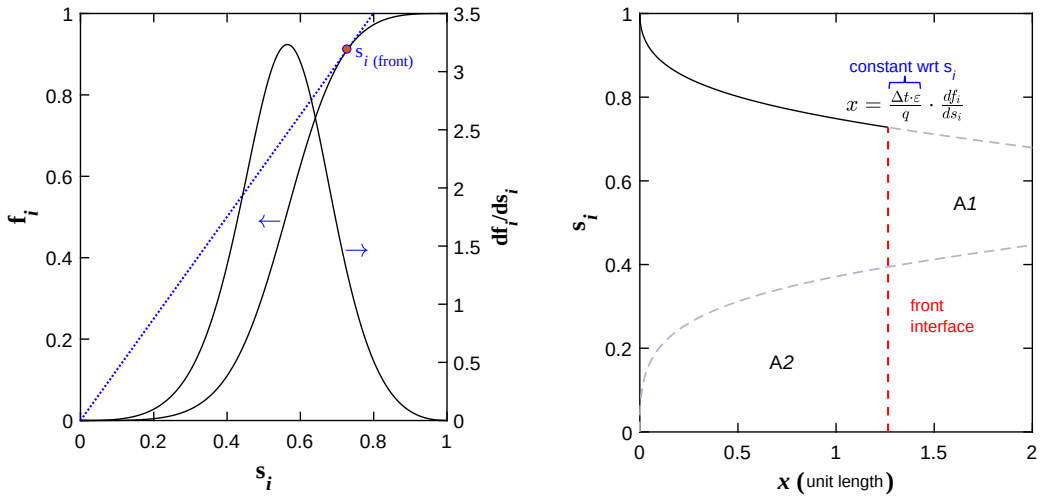

(a) Fractional Flow Rate (b) Interface Location

Figure 6.3: (a) Viscous model and its derivative using the Brooks-Corey correlation for relative permeabilities with $\xi = 3$ and $s_r = 0$. (b) The solution of fluid-fluid interface is calculated using equation 6.18, the Buckley-Leverett solution [7].

$$\left.\frac{df_i}{ds_i}\right|_{\text{front}} = \frac{f_{i,\text{front}} - f_{i,\text{initial}}}{s_{i,\text{front}} - s_{i,\text{initial}}} \tag{6.24}$$

where $s_{i,\text{initial}} = 0$ and $f_{i,\text{initial}} = 0$. Both methods, shown in Figure 6.3, compute the fluid-fluid front saturation as 0.72. Neither method compute the trapped saturation behind th emoving front has ever been used to.

6.4 Viscous-Capillary Model

Trapped saturation can be calculated by including the capillary pressure gradient. Neglecting any hydrostatic effects ($\theta = 0$) in equation 6.14 results in the viscous-capillary model.

$$f_i = \frac{1}{1 + \frac{K_{rd}}{K_{ri}}\frac{\mu_i}{\mu_d}} \left(1 + \alpha \, \frac{K_{rd}\,\kappa}{\mu_d\, q''_T} \, \frac{dP_c}{dx}\right) \tag{6.25}$$

The solution of viscous-capillary model, equation 6.25, requires correlations for relative permeabilities, $K_{r,i,j}$, and the capillary pressure, P_c. Including the non-linear capillary term in fractional flow function adds more mathematical complexity.

Combining equations 6.6 and 6.25 gives,

$$\frac{\partial s_i}{\partial t} = -\frac{q''_T}{\varepsilon}\frac{\partial}{\partial x}\left(\frac{1}{1 + \frac{K_{rd}}{K_{ri}}\frac{\mu_i}{\mu_d}} \left(1 + \alpha \frac{K_{rd}\,\kappa}{\mu_d\, q''_T} \, \frac{dP_c}{dx}\right)\right) \tag{6.26}$$

Equation 6.26 is a parabolic, nonlinear partial differential equation of a second order. The complexity arises from the capillary term, which has excluded the development

of exact analytical solutions and is the main cause of the instabilities in numerical models. A variety of methods have been used to solve equation 6.26, which has been used to caculate waterflood at low Ca and validate the solutions of numerical models [58, 147–151]. None of the previous solutions show the possibility to calculate trapped saturation [8, 9].

The dP_c/dx is the spatial derivative of the capillary pressure. It can be estimated using equation 6.27, which is obtained by combining equation 6.8, 6.9 and 6.11.

$$\alpha \frac{dP_c}{dx} = \frac{q_i'' \mu_i}{K_{ri} \kappa} - \frac{q_d'' \mu_d}{K_{rd} \kappa} \tag{6.27}$$

Equation 6.27, however, is only valid for an arbitrary flow rate ratio of the two phases and can not be applied to equation 6.25, which considers variable flow rate fractions for each phase.

Capillary pressure depends upon saturation, surface tension, mean pore size, and wettability; all of which may vary with position in the porous media. Therefore, the capillary pressure gradient becomes:

$$\frac{dP_c}{dx} = \frac{\partial P_c}{\partial s_i}\frac{\partial s_i}{\partial x} + \frac{\partial P_c}{\partial \sigma}\frac{\partial \sigma}{\partial x} + \frac{\partial P_c}{\partial \bar{r}}\frac{\partial \bar{r}}{\partial x} + \frac{\partial P_c}{\partial \alpha}\frac{\partial \alpha}{\partial x} \tag{6.28}$$

For this study, surface tension (σ), mean pore size ($\bar{r}$) and wettability (α) are considered to be constant throughout the porous media. Therefore, dP_c/dx can be written as:

$$\frac{dP_c}{dx} = \frac{\partial P_c}{\partial s_i}\frac{\partial s_i}{\partial x} \tag{6.29}$$

6.4.1 Capillary Pressure Correlations

Capillary pressure correlations are available in terms of saturation and this is a standard porous media characterization test. The capillary pressure correlation suggested by Leverett [52] converts pressure data to a general curve (the interfacial curvature) which is known as Leverett J-function. The Leverett J-function is used to extrapolate the capillary pressure data for other porous medium based on two-phase flow and the porous medium properties [52].

$$J = \frac{P_c}{\sigma}\sqrt{\frac{\kappa}{\varepsilon}} \tag{6.30}$$

where Leverett J-function is obtained using the regression analysis to the interfacial curvature and a correlation is developed in term of fluid saturation.

Brooks and Corey [2] developed a correlation for the capillary pressure that depends on two constants related to the porous medium: ξ and P_b, the bubble point pressure, as shown in Figure 6.2.

$$P_c = P_b\, s_e^{-1/\xi}; \tag{6.31}$$

Alternatively, Parker et al. [3] developed correlation for the capillary pressure as:

$$P_c = P_b \left(s_e^{-1/m} - 1 \right)^{1-m} \tag{6.32}$$

Leverett J-function and Brooks-Corey correlation are used in these analyses to illustrate $P_c = \mathrm{f}(s_i)$. Other capillary pressure correlations can be used in the fractional flow function model.

6.4.2 Saturation Gradient

In equation 6.29, ds_i/dx is the spatial dependency of saturation, which could be estimated from combining equation 6.29 and 6.27 to give equation 6.33, but it is also applied for a constant flow rate ratio [57].

$$\frac{ds_i}{dx} = \left(\frac{q_i'' \, \mu_i}{K_{ri} \, \kappa} - \frac{q_d'' \, \mu_d}{K_{rd} \, \kappa} \right) \frac{1}{\alpha \, \frac{dP_c}{ds_i}} \tag{6.33}$$

Mamghaderi et al. [152] attempted to resolve $\partial P_c / \partial s_i$ by approximating $\partial s_i / \partial x$ as:

$$\frac{ds_i}{dx} = \left(\frac{ds_i}{d \ln x} \right)_{x=L} \frac{1}{L} \tag{6.34}$$

where L is the length of the porous medium. This approximation estimates the saturation at breakthrough ($x = L$) where the relationship between s_i and $\ln x$ does

not change with time. For this study, ds_i/dx is the spatial derivative of saturation at the fluid-fluid interface as opposed to breakthrough.

6.4.3 Scaling the Saturation Gradient and Interpretation

The derivative ds_i/dx represents the slope of the discrete change in saturation, $\Delta s_i/\Delta x$, which can be approximated as $-1/\psi$ since the maximum change in saturation has a magnitude of one. The minus sign is to show the decrease in saturation in the flow direction and ψ is length scale that depends on the porous medium and the two phases properties. This simplification makes equation 6.25 a function of saturation and solution is easily obtained.

The length scale ψ is equivalent to that determined for transition from capillary fingering to stable displacement in drainage and imbibition by Médici and Allen [12].

$$\psi = \left(\frac{4}{3}\pi\bar{r}^3\right)^{1/3} \mathrm{Su} \tag{6.35}$$

The right side of equation 6.35 includes two parts, a characteristic pore size, $\sqrt[3]{4\pi\bar{r}^3/3}$, where $\bar{r}$ is the mean pore size, and the Suratman number, Su.

$$\mathrm{Su} = \frac{|\rho_i - \rho_d|\,\sigma\,\bar{r}}{\mu_i^2} \tag{6.36}$$

Here ρ is the density, σ is the surface tension, and μ_i is the viscosity of the injected

fluid. The Suratman number is dimensionless and can be thought of as a damping ratio on fluid-fluid front instabilities. Underdamped immiscible displacement have small viscous effects relative to inertial ($\Delta\rho$) and capillary (σ) effects and results in a small Suratman number. These conditions facilitate fingering instabilities and subsequent holdup (trapping) of the displaced fluid. A large Suratman number indicates viscous dominated flow that in the limit results in stable displacement and no trapping of the displaced phase.

Using this scaling the capillary pressure gradient becomes:

$$\frac{dP_c}{dx} = \frac{-1}{\psi}\frac{dP_c}{ds_i} \tag{6.37}$$

and the viscous-capillary fractional flow function becomes:

$$f_i = \frac{1}{1 + \frac{K_{rd}}{K_{ri}}\frac{\mu_i}{\mu_d}}\left(1 - \frac{K_{rd}\,\kappa}{\mu_d q''_T}\frac{\alpha}{\psi}\frac{dP_c}{ds_i}\right) \tag{6.38}$$

This scaling of the saturation gradient makes the fractional flow function of the viscous-capillary model as simple as the viscous model. The same assumption of a constant saturation at the front, $(ds_i)|_{\text{front}} = 0$, can be considered for the viscous-capillary model subsequently,

$$x|_{\text{front}} = \frac{q''_T \Delta t}{\varepsilon}\frac{d}{ds_i}\left(\frac{1}{1 + \frac{K_{rd}}{K_{ri}}\frac{\mu_i}{\mu_d}}\left(1 - \frac{K_{rd}\,\kappa}{\mu_d\, q''_T}\frac{\alpha}{\psi}\,\frac{dP_c}{ds_i}\right)\right) \tag{6.39}$$

Non-dimensional front position $x^* = x/L$ and time $t^* = \Delta t\, q''_T/L$, where L is the length of percolation path results in a simple expression that allows for comparison for front location under different times and wettabilities.

$$x^* = \frac{t^*}{\varepsilon}\frac{d}{ds_i}\left(\frac{1}{1+\frac{K_{rd}}{K_{ri}}\frac{\mu_i}{\mu_d}}\left(1-\frac{K_{rd}\,\kappa}{\mu_d\, q''_T}\frac{\alpha}{\psi}\frac{dP_c}{ds_i}\right)\right) \tag{6.40}$$

6.4.4 Viscous-Capillary Model Results and Interpretation

The results of the fractional flow function for both viscous model (f_i^v) in equation 6.38 and the viscous-capillary model (f_i^{vc}) in equation 6.15 are shown in Figure 6.4(a) using the Brooks and Corey [2] correlations. The viscous-capillary model (f_i^{vc}) is shifted to the left of the viscous model (f_i^v), due to capillarity. The results of both models are qualitatively similar to the analytical solution developed by Schmid et al. [150].

To compare the derivative of fractional flow function for viscous model (df_i^v/ds_i) in equation 6.15 and viscous-capillary model (df_i^{vc}/ds_i) in equation 6.38, the same flow rate and fluids properties in Table 6.1 are applied. Figure 6.4(b) shows a clear deviation from the df_i^v/ds_i due to the capillary term. From the viscous model solution in equation 6.18, shown in Figure 6.3(b), the term $q''_T\Delta t/\varepsilon$ is constant with respect to saturation. In other words, the solution to obtain the saturation (s_i) at any distance (x) is the result of the term $q''_T\Delta t/\varepsilon$ times df_i/ds_i as shown in Figure 6.3(b). This means that the negative part in the plot of the df_i^{vc}/ds_i in Figure 6.4(b) can not be a solution. Therefore, the negative part indicates the limit of fluid displacement and is considered trapped saturation, $s_o = 1 - s_i$ at $df_i/ds_i = 0$. For this example, the trapped saturation is $s_o = 0.33$.

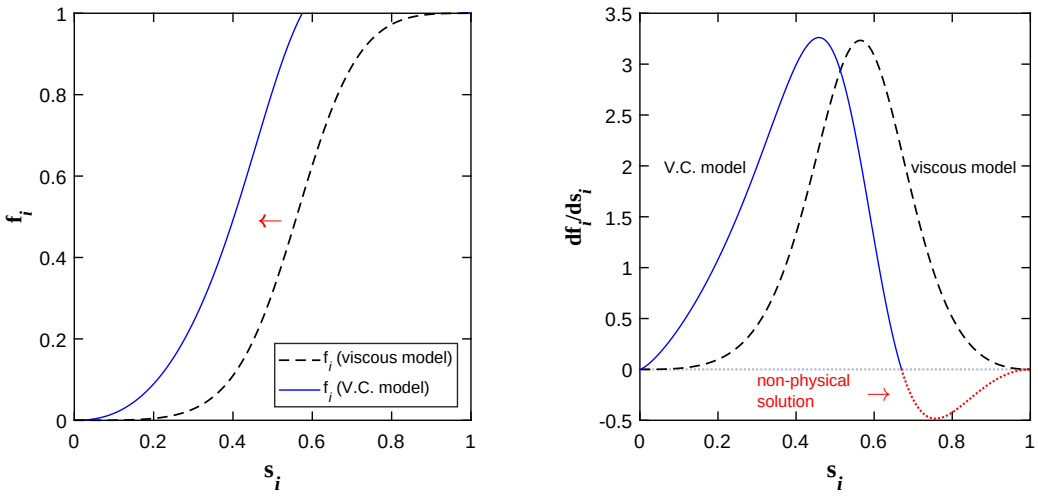

(a) f_i^v-f_i^{vc} (b) df_i^v/ds_i-df_i^{vc}/ds_i

Figure 6.4: Comparison between the solutions of the viscous model and viscous capillary model for (a) fractional flow function and (b) derivative of fractional flow function. The applied capillary number, viscosity ratio, mean pore size, Suratman number and the results in length scale are: $Ca = 5.6 \cdot 10^{-5}$, $M = 1$, $\bar{r} = 10\,\mu m$, Su $= 0.25$ and $\psi = 4.03 \cdot 10^{-6}\,m$, respectively.

Figure 6.5(a) shows the fractional flow function solutions versus saturation at different flow rates for both f_i^v and f_i^{vc}. For both imbibition and drainage, as the flow rate decreases, the solution of f_i^{vc} deviates from f_i^v and exceeds the maximum possible value of 1, which is not physical. At high flow rates where the viscous force is dominant the two solutions, f_i^v and f_i^{vc}, become identical. A similar result can be observed for the derivative of the fractional flow function, as shown in Figure 6.5(b). At high flow rate the viscous effect is dominant and both solutions, df_i^v/ds_i and df_i^{vc}/ds_i, are identical. The viscous force diminishes at low flow rates, and the capillary term in equation 6.38 has a dominant effect, which causes the deviation.

The solution of df_i^{vc}/ds_i in Figure 6.5(b) is part of equation 6.39, which specifies the position of the fluid-fluid interface. x in equation 6.39 is the expansion of df_i^{vc}/ds_i by the constant q_T''/ε at any time step Δt. This means the negative part of df_i^{vc}/ds_i also

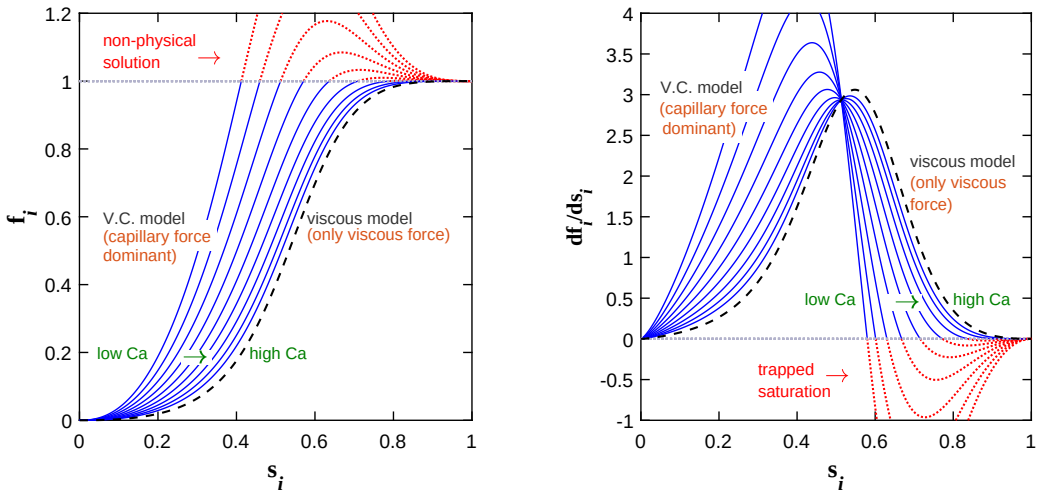

(a) Fractional Flow Function

(b) Derivative of Fractional Flow Function

Figure 6.5: The results of the viscous-capillary model shows the effect of capillary numbers on (a) fractional flow function and (b) the derivative. The applied capillary numbers, viscosity ratio, mean pore size, Suratman number and the results in length scale are: $Ca = 2.58 \cdot 10^{-5} - 3.25\,10^{-4}$, $M = 1$, $\bar{r} = 10\,\mu m$, Su $= 0.25$ and $\psi = 4.03 \cdot 10^{-6}\,m$, respectively.

leads to a negative part in the solution of x, which represents an impossible physical situation that contradicts the boundary condition at the inlet, $s_i = 1$. As a consequence, only the positive part of the curve is considered to be of physical relevance. This condition imposes a limit on the maximum level of the saturation that can be reached to invade the displaced fluid for a particular flow rate. This limiting value of the maximum saturation is representative of what is normally referred to as intrinsic trapped saturation. The intrinsic trapped saturation is the result of the injected fluid preferential percolation path on pores with the least interface displacement resistance. This preferential percolation path leaves some of the high interface resistance pores filled with the displaced fluid. Since the interface displacement resistance depends on the local interface velocity, the intrinsic trapped saturation depends on the capillary

number. At a low capillary number this displaced fluid remains trapped. Increasing the capillary number causes increasing effects resulting in a reduced volume of displaced fluid left trapped.

The intrinsic trapped saturations are calculated based on Figure 6.5(b). To obtain the capillary desaturation curve, CDC, the trapped saturations values (s_o) are gathered with the correspondence capillary numbers (Ca) as shown in Figure 6.6(a). The maximum intrinsic trapped saturation of the displaced phase, s_o, occurs at low capillary numbers (less than 10^{-6}). As the Ca increases, the injected fluid starts invading some of the pores still filled with the displaced fluid phase, reducing the intrinsic trapped saturation. The capillary number at which an increase in the flow rate starts decreasing the intrinsic trapped saturation is known as the critical capillary number. Once the critical capillary number is reached, any increase in the flow rate will result in a decrease of the intrinsic trapped saturation. The difference in intrinsic trapped saturations between imbibition and drainage for the same value of M is due to switching the correlations in the governing equations based on the injected and displaced fluids. This changes the mobility term (K_r/μ) in fractional flow function. Although the capillary hysteresis has an effect, it is not considered in these correlations for simplicity. In addition, the model shows the maximum trapped saturation at a different viscosity ratios, M. An increase in M, decreases the maximum intrinsic trapped saturation as shown in Figure 6.6(a).

There have been many studies that investigated trapped saturations experimentally [8, 9, 124]. Trapped saturation in sandstone for oil and gas with respect to the injected-displaced fluids pairs: brine-oil, brine-gas, and oil-gas are shown in Figure 6.6(b), where the same trend of the experimental data [8, 9] is predicted by the

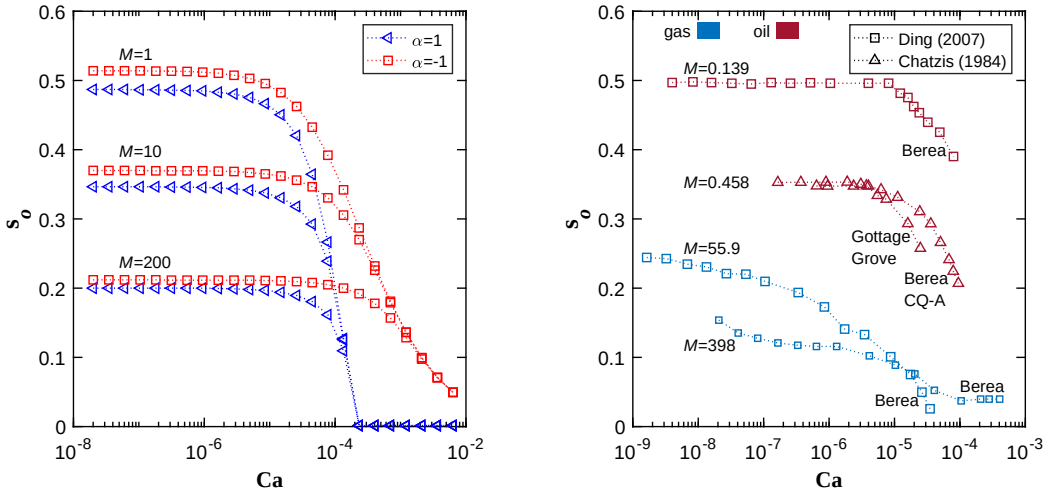

(a) Model Results

(b) Experimental Results

Figure 6.6: (a) Intrinsic trapped saturations predicted by the viscous-capillary model for drainage ($\alpha = -1$) and imbibition ($\alpha = 1$) at a different viscosity ratios (M) and capillary numbers (Ca). The applied mean pore size, Suratman number and the results in length scale are: $\bar{r} = 10\,\mu m$, Su $= 0.25$ and $\psi = 4.03 \cdot 10^{-6}\,m$, respectively.(b) The trapped saturations are estimated experimentally for many sandstones, at a range of Ca and M [8, 9].

viscous-capillary model. For the trapped saturations of the gas phase, the critical capillary number is not clear due to the compressibility of the gas during injection, or the dissolvability in the injected liquid phase, which is brine [8]. The FFT model assumes that the fluids are incompressible.

Equation 6.40 is solved for both viscous model ($\alpha = 0$) and viscous-capillary model ($\alpha = \pm 1$) as shown in Figure 6.7. The transient fluid-fluid interface profile is calculated for a fixed capillary number of $Ca = 10^{-5}$ at different dimensionless times. The physical mechanism that originates the intrinsic trapped saturations is also responsible for the increase in the value of the immiscible fluid-fluid front displacement for both flow regimes, imbibition (as shown in Figure 6.7(a)) and drainage (as shown

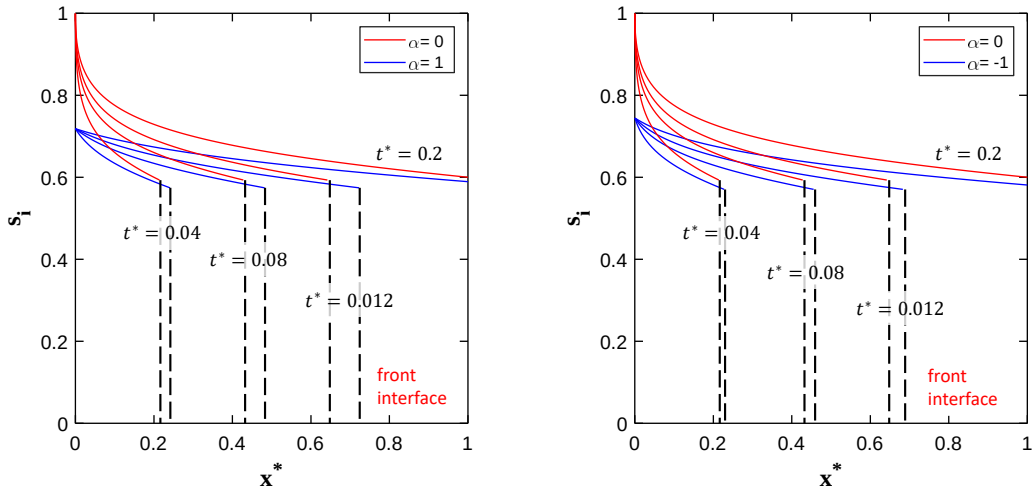

(a) Imbibition

(b) Drainage

Figure 6.7: The transient interfaces of the immiscible fluids are calculated at different dimensionless times. The solution based on Leveret J-function for capillary pressure (equations 2.18 and 6.30) and Brooks-Corey correlations (equations 6.19 and 6.20) for relative permeabilities. The applied capillary number and viscosity ratio are $Ca = 1 \cdot 10^{-6}$ and $M = 1$, respectively. (a) Wetting injected fluid, (b) Non-wetting injected fluid. Red lines indicate the viscous model, and blue lines indicate the viscous-capillary model predictions.

in Figure 6.7(b). For the same amount of injected fluid volume, in case of viscous-capillary model ($\alpha = \pm 1$), the front displacement will reach further into the porous medium when compared to the viscous model solution ($\alpha = 0$). Therefore, these simulations show the dominant effect of the capillary forces at low capillary number which have not been captured by previous models.

6.4.5 Validation of the Viscous-Capillary Model

The residual saturations of Berea sandstone have been reported for both oil and gas for which brine is the injected fluid [8]. Relative permeability and capillary

pressure in terms of fluid saturation have also been reported for Berea sandstone [10, 11]. The data from these publications were extracted from the published figures using Grabit™2016 (The Mathworks, Inc). Regression analyses were completed on the extracted to obtain correlations of relative permeabilities and capillary pressure as shown in Figure 6.8 and Figure 6.9, respectively. The regression coefficients are listed in Table 6.2. There is some uncertainty when extracting the data from figures. However, it does not affect the reliability of the correlations. Correlations for capillary pressure are adapted from [2] and relative permeabilities are adapted from [1].

$$P_c = P_b \, s_{e,id}^{-1/m_{id}}; \tag{6.41}$$

$$Kr_i = s_i^2 {s_{e,i}}^{m_i} \tag{6.42}$$

$$Kr_d = (1 - s_{e,d})^{m_d} \tag{6.43}$$

where $s_{e,id}$, $s_{e,i}$ and $s_{e,d}$ are giving by the following relations:

$$s_{e,id} = \frac{s_i - 0.15}{1 - 0.15} \tag{6.44}$$

$$s_{e,i} = \frac{s_i - s_{rd}}{1 - s_{ri}} \tag{6.45}$$

$$s_{e,d} = \frac{s_i - s_{ri}}{1 - s_{ri} - s_{rd}} \tag{6.46}$$

The parameters related to the porous medium are the mean pore size ($\bar{r}$), the porosity (ε) and absolute permeability (κ). The parameters related to fluid properties are viscosities of the injected (μ_i) and displaced (μ_d) fluids, densities of the injected (ρ_i) and displaced (ρ_d) fluids, and the surface tension (σ). Properties not available in Ding et al. [8] were obtained from Bera et al. [153], Shi et al. [154] for the same sandstone

and fluid pairs as shown in Table 6.2.

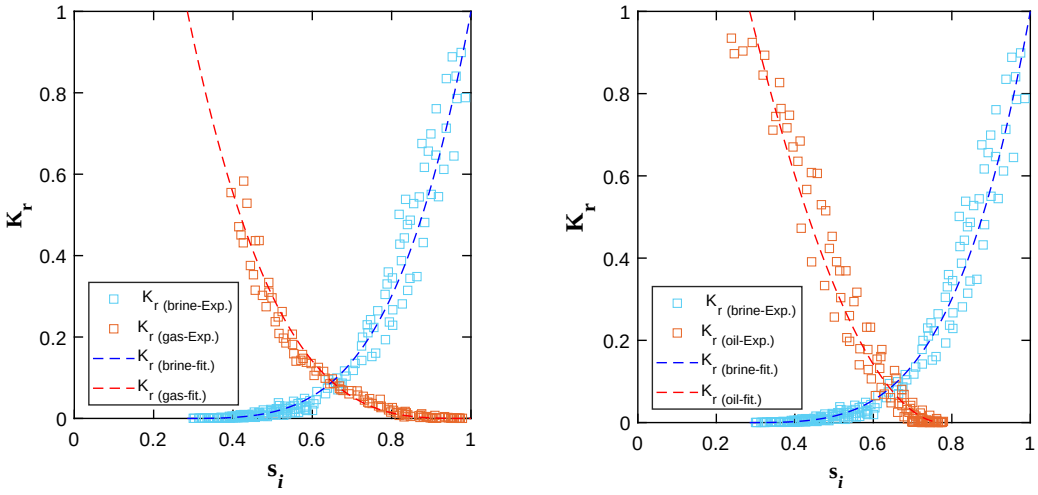

(a) Brine-Air (b) Brine-Oil

Figure 6.8: Experimental data of the relative permeabilities for brine-gas (a) and bine-oil (b) conducted on Berea sandstone [10]. The dashed lines are the fitting curves of the relative permeability correlations.

Data from Ding et al. [8] of intrinsic trapped saturation, s_o for brine displacing air in Berea sandstone are shown in Figure 6.10(a). The maximum intrinsic trapped saturation of air (displaced fluid) is 0.244 which occurs at a capillary number of $1.63 \cdot 10^{-9}$. When $Ca = 3.5 \cdot 10^{-5}$, the intrinsic trapped saturation of air is reduced to 0.025. Despite air being compressible, the viscous-capillary model predicts these limits remarkably well. Brine displacing air at room temperature has a Suratman number of $Su = 492.15$ which in Berea sandstone results in a saturation length scale of $\psi = 5.33 \cdot 10^{-3}\, m$. The corresponding gradient in the capillary pressure expansion is $ds/dx = -1.87 \cdot 10^{2}\, m^{-1}$.

Intrinsic trapped saturation data for oil in brine displacing oil in Berea sandstone [8] are shown in Figure 6.10(b). The viscous-capillary model matches the overall intrinsic

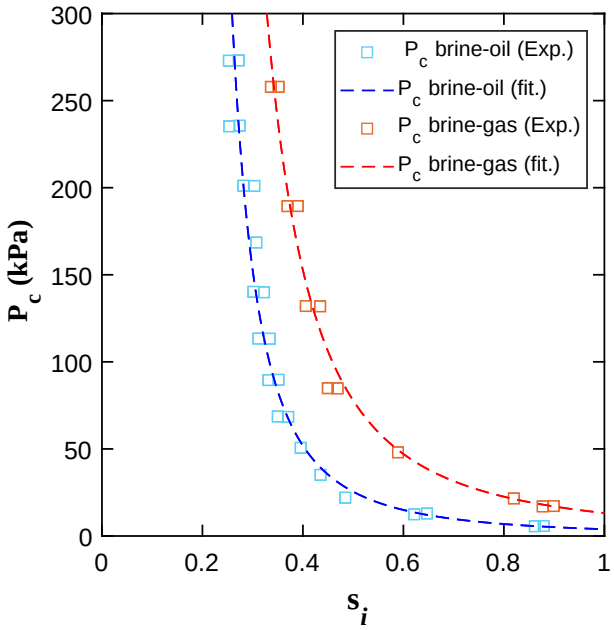

Figure 6.9: Experimental data of the capillary pressure conducted on Berea sandstone [11]. The dashed lines are the fitting curves of the capillary pressure correlations.

trapped saturation trend by Ding et al. [8] using the correlations shown in Figures 6.8(b) and 6.9. The viscous-capillary model accurately predicted the maximum intrinsic trapped saturation of oil ($s_o = 0.497$), which occurs at a capillary number of $4 \cdot 10^{-9}$. The critical capillary number of $Ca = 8.1 \cdot 10^{-6}$ is also captured. Even the gradual and then rapid decrease in the intrinsic trapped saturation after reaching critical capillary number are same. The Suratman number, $Su = 46.96$, results in a length scale of $\psi = 5.08 \cdot 10^{-4}\, m$, where the corresponding gradient in the capillary pressure expansion is $ds/dx = -1.96 \cdot 10^{3}\, m^{-1}$.

There is an increase in maximum trapped saturation of oil as compared to air due to many factors but this is due to decrease in the viscosity of the displaced fluid which reduces the viscosity ratio from $M = 55.9$ to $M = 0.139$. The Suratman

Table 6.2
Constants and correlation coefficients for viscous-capillary model.

Constant	brine displacing air	brine displacing oil
$\kappa\,(mD)$	400 [8]	400 [8]
$\mu_{i,b}\,(mPa.s)$	1 [8]	1 [8]
$\mu_{d,g}\,(mPa.s)$	0.017	− − −
$\mu_{d,o}\,(mPa.s)$	− − −	7.2 [8]
ε	24.01% [8]	24.01% [8]
$\sigma\,(mN/m)$	72.53 [8]	35 [153]
$\rho_{i,b}\,(kg/m^3)$	1010.9 [8]	1010.9 [8]
$\rho_{d,g}\,(kg/m^3)$	1.16	− − −
$\rho_{d,o}\,(kg/m^3)$	− − −	811.2 [8]
$\bar{r}\,(\mu m)$	6.72 [154]	6.72 [154]
Su	492.15	46.96
$\psi\,(m)$	$5.33 \cdot 10^{-3}$	$5.08 \cdot 10^{-4}$
s_{rb}	0.285	0.285
s_{rg}	0	− − −
s_{ro}	− − −	0.225
m_{bg}	0.5	− − −
m_{bo}	− − −	0.473
m_b	2.3	2.3
m_g	3.37	− − −
m_o	− − −	1.9

number is an order of magnitude larger for brine displacing air, compared to brine displacing oil. This means the dynamics at the interface are more stable for brine-air than brine-oil. In other words, the displacement is more stable and that leads to less maximum trapped saturation. The same explanation can be used to clarify the minimum intrinsic trapped saturation for both air and oil show in Figure 6.10(a).

6.5 Conclusions

A unique length scale is used to simplify the capillary term in the fractional flow theory model. The simplification makes the viscous-capillary model as simple as the

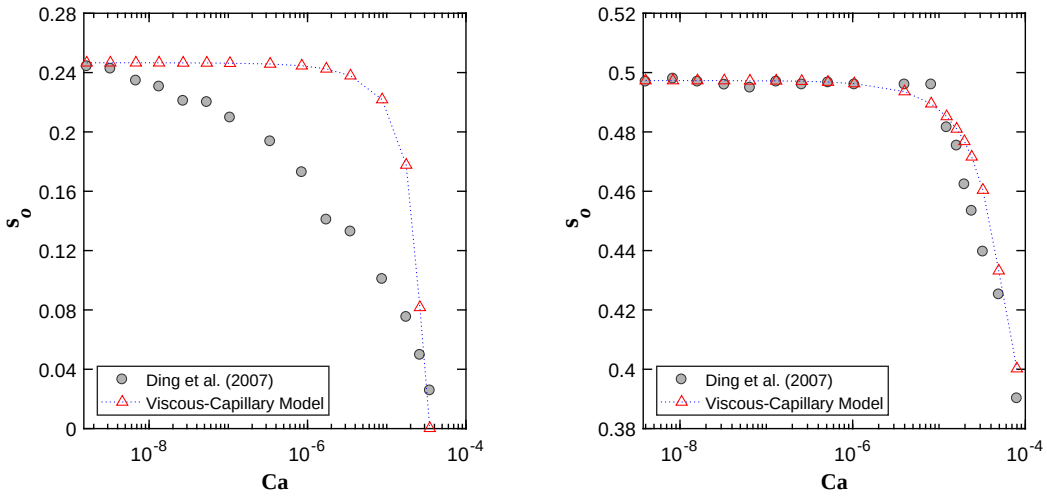

(a) Brine-Air

(b) Brine-Oil

Figure 6.10: The predicted trapped saturation by viscous-capillary model for (a) air and (b) oil compared to the experimental data by Ding et al. [8].

viscous model. The uniqueness of the results in model arises from the capability to estimate trapped saturation accurately at any capillary number and viscosity ratio. Furthermore, the model can be used to evaluate other models that ignore the capillary effect, like the viscous model, or to validate the numerical models.

Chapter 7

Conclusion and Recommendations

Experimental and theoretical methods were used to study the immiscible displacement of two-phase flow in porous media. In the experimental part, a Hele-Shaw setup is adapted to study liquid FC-3283 and air percolation in porous catalyst layers of PEM fuel cell. The irregular structure of a catalyst layer, which is designed to facilitate reactant transport to catalyst sites, has roughness at the pores surfaces as observed by SEM and TEM that affects mass transport. At a fixed RH condition, when flow rates are low the liquid percolates along the surface roughness of the pores leaving most of the pores filled with the gas phase (high trapped saturation of the gas). As the flow rate increases, FC-3283 flows through the bulk of the pores, where most of the pores are invaded (minimum trapped gas). These two flow regimes, flow along the surface roughness or through the bulk of the pores are related to whether capillary or viscous effects are dominated on the flow behavior. Catalyst layer conductance relative to mass transport was measured in terms of permeability at different RH conditions and fixed flow rate. The permeability decreases as RH increases due to ionomer

swelling. A correlation of permeability relationship to water content has been derived and it indicates that low ionomer water content ($\lambda < 3$) significantly improves mass transport through the pores of the catalyst layer. Above $\lambda = 3$ there is little change in permeability, which remains at the minimum value. Percolation pressure and liquid front dynamics for low and high RH conditioning indicate structural changes are occurring in the catalyst layer. These changes are significant enough to alter the imbibition flow regime for the same liquid injection rates. Static contact angle was also measured at different RH conditions. The measurements on the catalyst layers and membranes surfaces indicate possible morphological changes.

The theoretical study adapted fractional flow theory to calculate trapped saturation of a displaced fluid in a porous media. Both viscous and capillary effects are included in the formulation. A unique length scale, based on the Suratman number and characteristic pore size, enabled the viscous-capillary formulation to easily solved and validated against published test data. The uniqueness of the results in this model come from the ability to calculate trapped saturation accurately at any capillary number and viscosity ratio and, therefore, can be used to obtain capillary desaturation curves with the minimal inputs and computational cost.

Scholarly contributions from this work are summarized below:

1. An ex-situ technique to characterize reactant transport in fuel cell catalyst layers has been developed. This technique, based on a Hele-Shaw configuration, provides repeatable results for gas and liquid permeability in extremely thin ($< 15\,\mu$m) porous materials.

2. This technique was used to study how relative humidity affects mass/reactant

transport in fuel cell catalyst layers. The results indicate that there is a critical value of RH ($\approx 50\%$) corresponding to a critical ionomer water content ($\lambda \approx 3$) above which mass transport resistance is at a maximum value.

3. A computationally efficient model for immiscible displacement has been developed that can, for the first time, accurately calculate trapped saturation for any porous media. This model is based on fractional flow theory and integrates a unique length scale to capture the saturation gradient at the moving fluid-fluid front. The length scale incorporates the Suratman number, which characterizes the degree of damping of interface instabilities that lead to trapped saturation.

7.1 Recommendations

The efforts presented herein can be extended. The following is a list of tasks that can be further pursued:

1. Use the Hele-Shaw technique to develop a new transient method to estimate relative permeability for two-phase flow in thin porous material. The method depends on the transient percolation pressure and the correspondence wetted area. This method can be also used to create relative permeability curves in low gravity conditions, where there is no need for weighing the sample to determine saturation.

2. The percolation analysis in this study is related to two types of catalyst layers. The ionomer to carbon ratio (I/C) and the equivalent weight (EW) could affect the mass transport. This technique can be used to study a wider range of a

catalyst layer structure, morphology and chemistry.

3. The fractional flow model could be extended to study immiscible displacement in porous media other than sandstone. Applications include the following:

   (a) product water drainage and holdup porous transport layers, microporous layers, and catalyst layers of PEM fuel cells at various temperatures and relative humidity, and

   (b) liquid holdup in packed bed reactors in normal and low-gravity environments. There is a lack of predictive capability with existing computational models and tools that prevents robust design of packed bed reactors for space applications.

References

[1] M Dong and FAL Dullien. A new model for immiscible displacement in porous media. *Transport in Porous media*, 27(2):185–204, 1997.

[2] R Brooks and T Corey. Hydrau uc properties of porous media. *Hydrology Papers, Colorado State University*, 24, 1964.

[3] JC Parker, RJ Lenhard, and T Kuppusamy. A parametric model for constitutive properties governing multiphase flow in porous media. *Water Resources Research*, 23(4):618–624, 1987.

[4] Udit N Shrivastava, Helmut Fritzsche, and Kunal Karan. Interfacial and bulk water in ultrathin films of nafion, 3m pfsa, and 3m pfia ionomers on a polycrystalline platinum surface. *Macromolecules*, 51(23):9839–9849, 2018.

[5] Thomas A Zawodzinski Jr, Michal Neeman, Laurel O Sillerud, and Shimshon Gottesfeld. Determination of water diffusion coefficients in perfluorosulfonate ionomeric membranes. *The Journal of Physical Chemistry*, 95(15):6040–6044, 1991.

[6] Thomas E Springer, TA Zawodzinski, and Shimshon Gottesfeld. Polymer electrolyte fuel cell model. *Journal of the electrochemical society*, 138(8):2334, 1991.

[7] Se E Buckley, MCi Leverett, et al. Mechanism of fluid displacement in sands. *Transactions of the AIME*, 146(01):107–116, 1942.

[8] M Ding, A Kantzas, et al. Capillary number correlations for gas-liquid systems. *Journal of Canadian Petroleum Technology*, 46(02), 2007.

[9] Ioannis Chatzis, Norman R Morrow, et al. Correlation of capillary number relationships for sandstone. *Society of Petroleum Engineers Journal*, 24(05): 555–562, 1984.

[10] MJ Oak et al. Three-phase relative permeability of water-wet berea. In *SPE/-DOE Enhanced Oil Recovery Symposium*. Society of Petroleum Engineers, 1990.

[11] MJ Oak, LE Baker, and DC Thomas. Three-phase relative permeability of berea sandstone. *Journal of Petroleum Technology*, 42(08):1054–1061, 1990.

[12] Ezequiel F Médici and Jeffrey S Allen. A quantitative technique to compare experimental observations and numerical simulations of percolation in thin porous materials. *Transport in Porous Media*, 115(3):435–447, 2016.

[13] Larry W Lake, Russell T Johns, William R Rossen, and Gary A Pope. Fundamentals of enhanced oil recovery. 2014.

[14] Mark Adamski, Victor Kremesec, and Randall J Charbeneau. Residual saturation: What is it? how is it measured? how should we use it? In *Proceedings of the Petroleum Hydrocarbons and Organic Chemicals in Ground Water: Prevention, Assessment, and Remediation, 20th Conference and exposition, Costa mesa, CA*, 2003.

[15] James W Mercer and Robert M Cohen. A review of immiscible fluids in the subsurface: Properties, models, characterization and remediation. *Journal of Contaminant Hydrology*, 6(2):107–163, 1990.

[16] JH Langwaldt and JA Puhakka. On-site biological remediation of contaminated groundwater: a review. *Environmental pollution*, 107(2):187–197, 2000.

[17] Y Ouyang, Dilip Shinde, RS Mansell, and W Harris. Colloid-enhanced transport of chemicals in subsurface environments: A review. *Critical Reviews in Environmental Science and Technology*, 26(2):189–204, 1996.

[18] Hui Li, Yanghua Tang, Zhenwei Wang, Zheng Shi, Shaohong Wu, Datong Song, Jianlu Zhang, Khalid Fatih, Jiujun Zhang, Haijiang Wang, et al. *Journal of Power Sources*, 178(1):103–117, 2008.

[19] Seung-Gon Kim and Sang-Joon Lee. A review on experimental evaluation of water management in a polymer electrolyte fuel cell using x-ray imaging technique. *Journal of power sources*, 230:101–108, 2013.

[20] Sabri Ergun and Ao Ao Orning. Fluid flow through randomly packed columns and fluidized beds. *Industrial & Engineering Chemistry*, 41(6):1179–1184, 1949.

[21] Brian Joseph Motil. *Gas-liquid two-phase flow through packed bed reactors in microgravity*. PhD thesis, Case Western Reserve University, 2006.

[22] Pierre-Gilles De Gennes. Wetting: statics and dynamics. *Reviews of modern physics*, 57(3):827, 1985.

[23] Bernard P Tissot and Dietrich H Welte. *Petroleum formation and occurrence*. Springer Science & Business Media, 2013.

[24] Abhijit Y Dandekar. *Petroleum reservoir rock and fluid properties*. CRC press, 2013.

[25] Jacob Bear. *Dynamics of fluids in porous media*. Courier Corporation, 2013.

[26] PA Chuang, A Turhan, AK Heller, JS Brenizer, TA Trabold, and MM Mench. The nature of flooding and drying in polymer electrolyte fuel cells. In *International Conference on Fuel Cell Science, Engineering and Technology*, volume 37645, pages 31–37, 2005.

[27] Mehdi Mortazavi and Kazuya Tajiri. Two-phase flow pressure drop in flow channels of proton exchange membrane fuel cells: Review of experimental approaches. *Renewable and Sustainable Energy Reviews*, 45:296–317, 2015.

[28] A Bazylak. Liquid water visualization in pem fuel cells: A review. *International journal of hydrogen energy*, 34(9):3845–3857, 2009.

[29] Ahmet Kusoglu, Douglas Kushner, Devproshad K Paul, Kunal Karan, Michael A Hickner, and Adam Z Weber. Impact of substrate and processing on confinement of nafion thin films. *Advanced Functional Materials*, 24(30): 4763–4774, 2014.

[30] Yafei Chang, Jing Liu, Ruitao Li, Jian Zhao, Yanzhou Qin, Junfeng Zhang, Yan Yin, and Xianguo Li. Effect of humidity and thermal cycling on the catalyst layer structural changes in polymer electrolyte membrane fuel cells. *Energy Conversion and Management*, 189:24–32, 2019.

[31] Maria Bass, Amir Berman, Amarjeet Singh, Oleg Konovalov, and Viatcheslav Freger. Surface-induced micelle orientation in nafion films. *Macromolecules*, 44 (8):2893–2899, 2011.

[32] Trung Van Nguyen, Minh Vu Nguyen, Guangyu Lin, Nanxia Rao, Xin Xie, and Da-Ming Zhu. Characterization of surface ionic activity of proton conductive membranes by conductive atomic force microscopy. *Electrochemical and Solid State Letters*, 9(2):A88, 2005.

[33] Takahiro Suzuki, Shohji Tsushima, and Shuichiro Hirai. Fabrication and performance evaluation of structurally-controlled pemfc catalyst layers by blending platinum-supported and stand-alone carbon black. *Journal of power sources*, 233:269–276, 2013.

[34] DH Welte and PB Tissot. *Petroleum formation and occurrence*. Springer, 1984.

[35] Aimy Bazylak, David Sinton, and Ned Djilali. Dynamic water transport and droplet emergence in pemfc gas diffusion layers. *Journal of Power Sources*, 176 (1):240–246, 2008.

[36] Iryna V Zenyuk, Dilworth Y Parkinson, Gisuk Hwang, and Adam Z Weber. Probing water distribution in compressed fuel-cell gas-diffusion layers using x-ray computed tomography. *Electrochemistry Communications*, 53:24–28, 2015.

[37] Norman Epstein. On tortuosity and the tortuosity factor in flow and diffusion through porous media. *Chemical engineering science*, 44(3):777–779, 1989.

[38] FAL Dullien. Porous media-fluid transport and pore structure–academic press. *New York*, 98, 1979.

[39] Yudong Yuan, Nima Gholizadeh Doonechaly, and Sheik Rahman. An analytical model of apparent gas permeability for tight porous media. *Transport in porous media*, 111(1):193–214, 2016.

[40] Fateme Shamsi, Saeid Norouzi-Apourvari, and Saeed Jafari. The effect of morphological and topological characteristics on effective diffusivity and permeability of dual-structural-scale synthetic porous medium. *Transport in Porous Media*, 136(2):657–676, 2021.

[41] FAL Dullien and GK Dhawan. Characterization of pore structure by a combination of quantitative photomicrography and mercury porosimetry. *Journal of Colloid and Interface Science*, 47(2):337–349, 1974.

[42] Fereidoun Rezanezhad, William L Quinton, Jonathan S Price, David Elrick, TR Elliot, and Richard J Heck. Examining the effect of pore size distribution and shape on flow through unsaturated peat using computed tomography. *Hydrology and Earth System Sciences*, 13(10):1993–2002, 2009.

[43] John R Nimmo. Porosity and pore size distribution. *Encyclopedia of Soils in the Environment*, 3(1):295–303, 2004.

[44] Chang Sun Kong, Do-Young Kim, Han-Kyu Lee, Yong-Gun Shul, and Tae-Hee Lee. Influence of pore-size distribution of diffusion layer on mass-transport problems of proton exchange membrane fuel cells. *Journal of Power Sources*, 108(1-2):185–191, 2002.

[45] Ml C Leverett. Flow of oil-water mixtures through unconsolidated sands. *Transactions of the AIME*, 132(01):149–171, 1939.

[46] Antonio Costa. Permeability-porosity relationship: A reexamination of the kozeny-carman equation based on a fractal pore-space geometry assumption. *Geophysical research letters*, 33(2), 2006.

[47] Frank D Masch and Kleber J Denny. Grain size distribution and its effect on the permeability of unconsolidated sands. *Water Resources Research*, 2(4):665–677, 1966.

[48] Philip Crosbie Carman. Fluid flow through granular beds. *Trans. Inst. Chem. Eng.*, 15:150–166, 1937.

[49] Raphael Schulz, Nadja Ray, Simon Zech, Andreas Rupp, and Peter Knabner. Beyond kozeny–carman: predicting the permeability in porous media. *Transport in Porous Media*, 130(2):487–512, 2019.

[50] Tomas Rosén, Jens Eller, Jinfen Kang, Nikolaos I Prasianakis, John Mantzaras, and Felix N Büchi. Saturation dependent effective transport properties of pefc gas diffusion layers. *Journal of The Electrochemical Society*, 159(9):F536–F544, 2012.

[51] Jaoudat Touma and Michel Vauclin. Experimental and numerical analysis of two-phase infiltration in a partially saturated soil. *Transport in porous media*, 1(1):27–55, 1986.

[52] MoC Leverett. Capillary behavior in porous solids. *Transactions of the AIME*, 142(01):152–169, 1941.

[53] Jeff T Gostick, Marios A Ioannidis, Michael W Fowler, and Mark D Pritzker. Direct measurement of the capillary pressure characteristics of water–air–gas diffusion layer systems for pem fuel cells. *Electrochemistry Communications*, 10 (10):1520–1523, 2008.

[54] Kent S Udell. Heat transfer in porous media considering phase change and capillarity—the heat pipe effect. *International Journal of Heat and Mass Transfer*, 28(2):485–495, 1985.

[55] IS Hussaini and CY Wang. Measurement of relative permeability of fuel cell diffusion media. *Journal of Power Sources*, 195(12):3830–3840, 2010.

[56] EF Johnson, DP Bossler, and VO Bossler. Calculation of relative permeability from displacement experiments. *Transactions of the AIME*, 216(01):370–372, 1959.

[57] JG Richardson, JK Kerver, JA Hafford, JS Osoba, et al. Laboratory determination of relative permeability. *Journal of Petroleum Technology*, 4(08):187–196, 1952.

[58] David B McWhorter and Daniel K Sunada. Exact integral solutions for two-phase flow. *Water Resources Research*, 26(3):399–413, 1990.

[59] Roland Lenormand. Liquids in porous media. *Journal of Physics: Condensed Matter*, 2(S):SA79, 1990.

[60] EF Medici and JS Allen. Existence of the phase drainage diagram in proton exchange membrane fuel cell fibrous diffusion media. *Journal of Power Sources*, 191(2):417–427, 2009.

[61] Bauyrzhan K. Primkulov, Amir A. Pahlavan, Xiaojing Fu, Benzhong Zhao, Christopher W. MacMinn, and Ruben Juanes. Wettability and lenormand's diagram. *Journal of Fluid Mechanics*, 923:A34, 2021. doi: 10.1017/jfm.2021.579.

[62] Pucheng Pei and Huicui Chen. Main factors affecting the lifetime of proton exchange membrane fuel cells in vehicle applications: A review. *Applied Energy*, 125:60–75, 2014.

[63] Mark K Debe, Alison Schmoeckel, Susan Hendricks, George Vernstrom, Greg Haugen, and Radoslav Atanasoski. Durability aspects of nanostructured thin film catalysts for pem fuel cells. *ECS Transactions*, 1(8):51, 2006.

[64] Mark K Debe. Nanostructured thin film electrocatalysts for pem fuel cells-a tutorial on the fundamental characteristics and practical properties of nstf catalysts. *Ecs Transactions*, 45(2):47, 2012.

[65] Vincent Lee, Viatcheslav Berejnov, Marcia West, Sumit Kundu, Darija Susac, Jürgen Stumper, Radoslav T Atanasoski, Mark Debe, and Adam P Hitchcock. Scanning transmission x-ray microscopy of nano structured thin film catalysts for proton-exchange-membrane fuel cells. *Journal of Power Sources*, 263:163–174, 2014.

[66] Phengxay Deevanhxay, Takashi Sasabe, Shohji Tsushima, and Shuichiro Hirai. Effect of liquid water distribution in gas diffusion media with and without microporous layer on pem fuel cell performance. *Electrochemistry Communications*, 34:239–241, 2013.

[67] Feng-Yuan Zhang, Dusan Spernjak, Ajay K Prasad, and Suresh G Advani. In situ characterization of the catalyst layer in a polymer electrolyte membrane fuel cell. *Journal of The Electrochemical Society*, 154(11):B1152, 2007.

[68] J Lee, J Hinebaugh, and A Bazylak. Synchrotron x-ray radiographic investigations of liquid water transport behavior in a pemfc with mpl-coated gdls. *Journal of power sources*, 227:123–130, 2013.

[69] Phengxay Deevanhxay, Takashi Sasabe, Shohji Tsushima, and Shuichiro Hirai. In situ diagnostic of liquid water distribution in cathode catalyst layer in an operating pemfc by high-resolution soft x-ray radiography. *Electrochemistry communications*, 22:33–36, 2012.

[70] Kyu-Jin Lee, Jung Ho Kang, and Jin Hyun Nam. Liquid water distribution in hydrophobic gas-diffusion layers with interconnect rib geometry: An invasion-percolation pore network analysis. *international journal of hydrogen energy*, 39 (12):6646–6656, 2014.

[71] Guanxiong Wang, Luigi Osmieri, Andrew G Star, Jason Pfeilsticker, and Kenneth C Neyerlin. Elucidating the role of ionomer in the performance of platinum group metal-free catalyst layer via in situ electrochemical diagnostics. *Journal of The Electrochemical Society*, 167(4):044519, 2020.

[72] Karren More, Rod Borup, and Kimberly Reeves. Identifying contributing degradation phenomena in pem fuel cell membrane electride assemblies via electron microscopy. *ECS Transactions*, 3(1):717, 2006.

[73] M Lopez-Haro, L Guétaz, T Printemps, A Morin, S Escribano, P-H Jouneau, P Bayle-Guillemaud, F Chandezon, and G Gebel. Three-dimensional analysis of nafion layers in fuel cell electrodes. *Nature communications*, 5(1):1–6, 2014.

[74] Makoto Uchida, Yuko Aoyama, Nobuo Eda, and Akira Ohta. Investigation of the microstructure in the catalyst layer and effects of both perfluorosulfonate ionomer and ptfe-loaded carbon on the catalyst layer of polymer electrolyte fuel cells. *Journal of the Electrochemical Society*, 142(12):4143, 1995.

[75] Firat C Cetinbas, Rajesh K Ahluwalia, Nancy N Kariuki, and Deborah J Myers. Agglomerates in polymer electrolyte fuel cell electrodes: Part i. structural characterization. *Journal of The Electrochemical Society*, 165(13):F1051, 2018.

[76] Y-G Yoon, G-G Park, T-H Yang, J-N Han, W-Y Lee, and C-S Kim. Effect of pore structure of catalyst layer in a pemfc on its performance. *International Journal of Hydrogen Energy*, 28(6):657–662, 2003.

[77] Tatyana Soboleva, Kourosh Malek, Zhong Xie, Titichai Navessin, and Steven Holdcroft. Pemfc catalyst layers: the role of micropores and mesopores on water sorption and fuel cell activity. *ACS applied materials & interfaces*, 3(6): 1827–1837, 2011.

[78] Doo Sung Hwang, Chi Hoon Park, Sung Chul Yi, and Young Moo Lee. Optimal catalyst layer structure of polymer electrolyte membrane fuel cell. *International journal of hydrogen energy*, 36(16):9876–9885, 2011.

[79] Ai Suzuki, Unal Sen, Tatsuya Hattori, Ryuji Miura, Ryo Nagumo, Hideyuki Tsuboi, Nozomu Hatakeyama, Akira Endou, Hiromitsu Takaba, Mark C Williams, et al. Ionomer content in the catalyst layer of polymer electrolyte membrane fuel cell (pemfc): Effects on diffusion and performance. *International Journal of Hydrogen Energy*, 36(3):2221–2229, 2011.

[80] MB Sassin, Y Garsany, RW Atkinson III, RME Hjelm, and KE Swider-Lyons. Understanding the interplay between cathode catalyst layer porosity and thickness on transport limitations en route to high-performance pemfcs. *International Journal of Hydrogen Energy*, 44(31):16944–16955, 2019.

[81] VaA Paganin, EaA Ticianelli, and ER Gonzalez. Development and electrochemical studies of gas diffusion electrodes for polymer electrolyte fuel cells. *Journal of Applied Electrochemistry*, 26(3):297–304, 1996.

[82] E Antolini, L Giorgi, A Pozio, and E Passalacqua. Influence of nafion loading in the catalyst layer of gas-diffusion electrodes for pefc. *Journal of Power Sources*, 77(2):136–142, 1999.

[83] E Passalacqua, F Lufrano, G Squadrito, A Patti, and L Giorgi. Nafion content in the catalyst layer of polymer electrolyte fuel cells: effects on structure and performance. *Electrochimica Acta*, 46(6):799–805, 2001.

[84] Hyun Ki Shim, Devproshad K Paul, and Kunal Karan. Resolving the contradiction between anomalously high water uptake and low conductivity of nanothin nafion films on sio2 substrate. *Macromolecules*, 48(22):8394–8397, 2015.

[85] Udit N Shrivastava, Kota Suetsugu, Shusaku Nagano, Helmut Fritzsche, Yuki Nagao, and Kunal Karan. Cross-correlated humidity-dependent structural evolution of nafion thin films confined on a platinum substrate. *Soft Matter*, 16(5): 1190–1200, 2020.

[86] G Gebel, P Aldebert, and M Pineri. Swelling study of perfluorosulphonated ionomer membranes. *Polymer*, 34(2):333–339, 1993.

[87] JA Elliott, S Hanna, AMS Elliott, and GE Cooley. The swelling behaviour of perfluorinated ionomer membranes in ethanol/water mixtures. *Polymer*, 42(5): 2251–2253, 2001.

[88] Shahab Bayani Ahangar, Kishan Bellur, Ezequiel Medici, Kazuya Tajiri, Jeffrey S Allen, and Chang Kyoung Choi. Optical properties and swelling of thin film perfluorinated sulfonic-acid ionomer. *ECS Transactions*, 92(8):197, 2019.

[89] Hiroshi Iden and Atsushi Ohma. An in situ technique for analyzing ionomer coverage in catalyst layers. *Journal of Electroanalytical Chemistry*, 693:34–41, 2013.

[90] Karrar Alofari, Ezequiel Me, Kazuya Tajiri, Jeffrey Allen, et al. Ionomer films impact on the structure, flow regime, and the wettability of the catalyst layer of pemfc. In *E3S Web of Conferences*, volume 334, page 04019. EDP Sciences, 2022.

[91] J Hinebaugh, J Lee, C Mascarenhas, and A Bazylak. Quantifying percolation events in pem fuel cell using synchrotron radiography. *Electrochimica Acta*, 184: 417–426, 2015.

[92] H Markötter, R Alink, J Haußmann, K Dittmann, Tobias Arlt, F Wieder, C Tötzke, M Klages, C Reiter, Heinrich Riesemeier, et al. Visualization of the water distribution in perforated gas diffusion layers by means of synchrotron x-ray radiography. *International Journal of Hydrogen Energy*, 37(9):7757–7761, 2012.

[93] Christoph Hartnig, Ingo Manke, Robert Kuhn, Sebastian Kleinau, Jürgen Goebbels, and John Banhart. High-resolution in-plane investigation of the water evolution and transport in pem fuel cells. *Journal of Power Sources*, 188 (2):468–474, 2009.

[94] A Bazylak, D Sinton, Z-S Liu, and N Djilali. Effect of compression on liquid water transport and microstructure of pemfc gas diffusion layers. *Journal of Power Sources*, 163(2):784–792, 2007.

[95] Bin Gao, Tammo S Steenhuis, Yunati Zevi, J-Yves Parlange, Robert N Carter, and Thomas A Trabold. Visualization of unstable water flow in a fuel cell gas diffusion layer. *Journal of Power Sources*, 190(2):493–498, 2009.

[96] S Litster, D Sinton, and N Djilali. Ex situ visualization of liquid water transport in pem fuel cell gas diffusion layers. *Journal of Power Sources*, 154(1):95–105, 2006.

[97] Jeff T Gostick, Marios A Ioannidis, Michael W Fowler, and Mark D Pritzker. Wettability and capillary behavior of fibrous gas diffusion media for polymer electrolyte membrane fuel cells. *Journal of Power Sources*, 194(1):433–444, 2009.

[98] Mehdi Mortazavi, Anthony D Santamaria, Vedang Chauhan, Jingru Z Benner, Mahbod Heidari, and Ezequiel F Médici. Effect of pem fuel cell porous media compression on in-plane transport phenomena. *Journal of Power Sources Advances*, 1:100001, 2020.

[99] Karrar Takleef Alofari, Ezequiel Medici, Kazuya Tajiri, and Jeffrey S Allen. Percolation behavior in catalytic porous material. *ECS Transactions*, 92(8):71, 2019.

[100] FHB Lima, J Zhang, MH Shao, K Sasaki, MB Vukmirovic, a EA Ticianelli, and RR Adzic. Catalytic activity- d-band center correlation for the o2 reduction reaction on platinum in alkaline solutions. *The Journal of Physical Chemistry C*, 111(1):404–410, 2007.

[101] UA Paulus, TJ Schmidt, HA Gasteiger, and RJ Behm. Oxygen reduction on a high-surface area pt/vulcan carbon catalyst: a thin-film rotating ring-disk electrode study. *Journal of Electroanalytical Chemistry*, 495(2):134–145, 2001.

[102] Jin Suntivich, Hubert A Gasteiger, Naoaki Yabuuchi, and Yang Shao-Horn. Electrocatalytic measurement methodology of oxide catalysts using a thin-film rotating disk electrode. *Journal of The Electrochemical Society*, 157(8):B1263, 2010.

[103] Sanjay Sharma and Dennis A Siginer. Permeability measurement methods in porous media of fiber reinforced composites. *Applied Mechanics Reviews*, 63(2), 2010.

[104] Roland Lenormand and Cesar Zarcone. Role of roughness and edges during imbibition in square capillaries. In *SPE annual technical conference and exhibition*. OnePetro, 1984.

[105] Zhonghao Sun, Ayaz Mehmani, and Carlos Torres-Verdín. Subpore-scale trapping mechanisms following imbibition: A microfluidics investigation of surface roughness effects. *Water Resources Research*, 57(2):e2020WR028324, 2021.

[106] Kewen Li, Danfeng Zhang, Huiyuan Bian, Chao Meng, and Yanan Yang. Criteria for applying the lucas-washburn law. *Scientific reports*, 5(1):1–7, 2015.

[107] Devproshad K Paul, Kunal Karan, Aristides Docoslis, Javier B Giorgi, and Joshua Pearce. Characteristics of self-assembled ultrathin nafion films. *Macromolecules*, 46(9):3461–3475, 2013.

[108] Devproshad K Paul, Richard McCreery, and Kunal Karan. Proton transport property in supported nafion nanothin films by electrochemical impedance spectroscopy. *Journal of the electrochemical society*, 161(14):F1395, 2014.

[109] Adam Z Weber and John Newman. Transport in polymer-electrolyte membranes: Ii. mathematical model. *Journal of the Electrochemical Society*, 151(2): A311, 2004.

[110] Huu-Dat Nguyen, Regis Porihel, Jean-Blaise Brubach, Emilie Planes, Priscillia Soudant, Patrick Judeinstein, Lionel Porcar, Sandrine Lyonnard, and Cristina Iojoiu. Perfluorosulfonyl imide versus perfluorosulfonic acid ionomers in proton-exchange membrane fuel cells at low relative humidity. *ChemSusChem*, 13(3): 590–600, 2020.

[111] Timothy D Gierke, GE Munn, and FCd Wilson. The morphology in nafion perfluorinated membrane products, as determined by wide-and small-angle x-ray studies. *Journal of Polymer Science: Polymer Physics Edition*, 19(11): 1687–1704, 1981.

[112] Qinggang He, Ahmet Kusoglu, Ivan T Lucas, Kyle Clark, Adam Z Weber, and Robert Kostecki. Correlating humidity-dependent ionically conductive surface area with transport phenomena in proton-exchange membranes. *The Journal of Physical Chemistry B*, 115(40):11650–11657, 2011.

[113] Devproshad K Paul and Kunal Karan. Conductivity and wettability changes of ultrathin nafion films subjected to thermal annealing and liquid water exposure. *The Journal of Physical Chemistry C*, 118(4):1828–1835, 2014.

[114] Maria Bass, Amir Berman, Amarjeet Singh, Oleg Konovalov, and Viatcheslav Freger. Surface structure of nafion in vapor and liquid. *The Journal of Physical Chemistry B*, 114(11):3784–3790, 2010.

[115] XL Wang, WK Wang, ZG Qu, GF Ren, and HC Wang. Surface roughness dominated wettability of carbon fiber in gas diffusion layer materials revealed by molecular dynamics simulations. *International Journal of Hydrogen Energy*, 2021.

[116] Jaroslaw Drelich and Jan D Miller. The effect of solid surface heterogeneity and roughness on the contact angle/drop (bubble) size relationship. *Journal of colloid and interface science*, 164(1):252–259, 1994.

[117] Nagappan Ramaswamy, Swami Kumaraguru, Roland Koestner, Timothy Fuller, Wenbin Gu, Nancy Kariuki, Deborah Myers, Peter J Dudenas, and Ahmet Kusoglu. Editors' choice—ionomer side chain length and equivalent weight impact on high current density transport resistances in pemfc cathodes. *Journal of The Electrochemical Society*, 168(2):024518, 2021.

[118] Francis AL Dullien. *Porous media: fluid transport and pore structure*. Academic press, 2012.

[119] Matthew M Mench. *Fuel cell engines*. John Wiley & Sons, 2008.

[120] ChungHyuk Lee, Benzhong Zhao, Rami Abouatallah, Rainey Wang, and Aimy Bazylak. Compressible-gas invasion into liquid-saturated porous media: Application to polymer-electrolyte-membrane electrolyzers. *Physical Review Applied*, 11(5):054029, 2019.

[121] Felix N Büchi, Reto Flückiger, Denis Tehlar, Federica Marone, and Marco Stampanoni. *ECS Transactions*, 16(2):587–592, 2008.

[122] Nick P Valenti, RM Valenti, and LF Koederitz. A unified theory on residual oil saturation and irreducible water saturation. In *SPE Annual Technical Conference and Exhibition*. OnePetro, 2002.

[123] Huina Li, Chongxun Pan, and Cass T Miller. Pore-scale investigation of viscous coupling effects for two-phase flow in porous media. *Physical Review E*, 72(2): 026705, 2005.

[124] NR Morrow and B Songkran. Effect of viscous and buoyancy forces on non-wetting phase trapping in porous media. In *Surface phenomena in enhanced oil recovery*, pages 387–411. Springer, 1981.

[125] Avery H Demond and Paul V Roberts. Effect of interfacial forces on two-phase capillary pressure—saturation relationships. *Water Resources Research*, 27(3): 423–437, 1991.

[126] Norman R Morrow. Irreducible wetting-phase saturations in porous media. *Chemical Engineering Science*, 25(11):1799–1815, 1970.

[127] JP Stokes, DA Weitz, Jerry P Gollub, A Dougherty, MO Robbins, PM Chaikin, and HM Lindsay. Interfacial stability of immiscible displacement in a porous medium. *Physical review letters*, 57(14):1718, 1986.

[128] Ran Holtzman and Enrico Segre. Wettability stabilizes fluid invasion into porous media via nonlocal, cooperative pore filling. *Physical review letters*, 115(16): 164501, 2015.

[129] Mathias Trojer, Michael L Szulczewski, and Ruben Juanes. Stabilizing fluid-fluid displacements in porous media through wettability alteration. *Physical Review Applied*, 3(5):054008, 2015.

[130] Ran Holtzman. Effects of pore-scale disorder on fluid displacement in partially-wettable porous media. *Scientific reports*, 6:36221, 2016.

[131] Nancy B Lu, Christopher A Browne, Daniel B Amchin, Janine K Nunes, and Sujit S Datta. Controlling capillary fingering using pore size gradients in disordered media. *Physical Review Fluids*, 4(8):084303, 2019.

[132] Seung-Woo Jeong. Evaluation of the use of capillary numbers for quantifying the removal of dnapl trapped in a porous medium by surfactant and surfactant foam floods. *Journal of colloid and interface science*, 282(1):182–187, 2005.

[133] Hu Guo, Ma Dou, Wang Hanqing, Fuyong Wang, Gu Yuanyuan, Zhaoyan Yu, Wang Yansheng, and Yiqiang Li. Proper use of capillary number in chemical flooding. *Journal of Chemistry*, 2017, 2017.

[134] Amaar Siyal, Khurshed Rahimov, Waleed AlAmeri, and Emad W Al-Shalabi. Recent advances in capillary desaturation curves for sandstone and carbonate reservoirs. In *Abu Dhabi International Petroleum Exhibition & Conference*. OnePetro, 2021.

[135] Mariam Shakeel, Aida Samanova, Peyman Pourafshary, and Muhammad Rehan Hashmet. Capillary desaturation tendency of hybrid engineered water-based chemical enhanced oil recovery methods. *Energies*, 14(14):4368, 2021.

[136] Gary A Pope. The application of fractional flow theory to enhanced oil recovery. *Society of Petroleum Engineers Journal*, 20(03):191–205, 1980.

[137] Mark P Walsh and Larry W Lake. Applying fractional flow theory to solvent flooding and chase fluids. *Journal of Petroleum Science and Engineering*, 2(4): 281–303, 1989.

[138] Kegang Ling. Fractional flow in radial flow systems: a study for peripheral waterflood. *Journal of Petroleum Exploration and Production Technology*, 6(3): 441–450, 2016.

[139] Khwaja Naweed Seddiqi, Zabihullah Mahdi, and Shigeo Honma. Experimental and graphical investigation on oil recovery by buckley-leveret theory. *World Academy of Science, Engineering and Technology, International Journal of Environmental, Chemical, Ecological, Geological and Geophysical Engineering*, 11 (1):64–73, 2017.

[140] Lei Ding, Qianhui Wu, Lei Zhang, and Dominique Guérillot. Application of fractional flow theory for analytical modeling of surfactant flooding, polymer flooding, and surfactant/polymer flooding for chemical enhanced oil recovery. *Water*, 12(8):2195, 2020.

[141] JG Richardson. The calculation of waterflood recovery from steady-state relative permeability data. *Journal of petroleum technology*, 9(05):64–66, 1957.

[142] Gu Sun Jeong, Seil Ki, Dae Sung Lee, and Ilsik Jang. Effect of the flow rate on the relative permeability curve in the co2 and brine system for co2 sequestration. *Sustainability*, 13(3):1543, 2021.

[143] JS Osoba, JG Richardson, JK Kerver, JA Hafford, and PM Blair. Laboratory measurements of relative permeability. *Journal of Petroleum Technology*, 3(02): 47–56, 1951.

[144] CR Sandberg, LS Gournay, and RF Sippel. The effect of fluid-flow rate and viscosity on laboratory determinations of oil-water relative permeabilities. *Transactions of the AIME*, 213(01):36–43, 1958.

[145] Amir Hossein Alizadeh, Alireza Keshavarz, and Manouchehr Haghighi. Flow rate effect on two-phase relative permeability in iranian carbonate rocks. In *SPE Middle East oil and gas show and conference*. OnePetro, 2007.

[146] Henry J Welge. A simplified method for computing oil recovery by gas or water drive. *Journal of Petroleum Technology*, 4(04):91–98, 1952.

[147] Zhong-Xiang Chen et al. Some invariant solutions to two-phase fluid displacement problems including capillary effect (includes associated papers 18744 and 19037). *SPE reservoir engineering*, 3(02):691–700, 1988.

[148] Francisco Javier Rosado-Vazquez, Edgar Rene Rangel-German, et al. Analytical model for vertical oil/water displacement under combined viscous, capillary, and gravity effects. In *SPE Western Regional/AAPG Pacific Section/GSA Cordilleran Section Joint Meeting*. Society of Petroleum Engineers, 2006.

[149] DW Ruth and JK Arthur. A revised analytic solution to the linear displacement problem including capillary pressure effects. *Transport in Porous Media*, 86(3): 881–894, 2011.

[150] Karen S Schmid, Nayef Alyafei, Sebastian Geiger, Martin J Blunt, et al. Analytical solutions for spontaneous imbibition: Fractional-flow theory and experimental analysis. *SPE Journal*, 2016.

[151] Zhong Zheng and Jerome A Neufeld. Self-similar dynamics of two-phase flows injected into a confined porous layer. *Journal of Fluid Mechanics*, 877:882–921, 2019.

[152] Azadeh Mamghaderi, Behzad Rostami, and Seyed Hamed Tabatabaie. A novel approach to measuring water and oil relative permeabilities in two-phase fluid flow in porous media. *Iranian Journal of Oil and Gas Science and Technology*, 7(2):14–34, 2018.

[153] Achinta Bera, Keka Ojha, Ajay Mandal, and T Kumar. Interfacial tension and phase behavior of surfactant-brine–oil system. *Colloids and surfaces a: physicochemical and engineering aspects*, 383(1-3):114–119, 2011.

[154] Ji-Quan Shi, Ziqiu Xue, and Sevket Durucan. Supercritical co2 core flooding and imbibition in berea sandstone—ct imaging and numerical simulation. *Energy Procedia*, 4:5001–5008, 2011.

[155] Peter Berg, Keith Promislow, Jean St Pierre, Jürgen Stumper, and Brian Wetton. Water management in pem fuel cells. *Journal of the Electrochemical Society*, 151(3):A341, 2004.

[156] Mohamed El Hannach, Joël Pauchet, and Marc Prat. Pore network modeling: application to multiphase transport inside the cathode catalyst layer of proton exchange membrane fuel cell. *Electrochimica Acta*, 56(28):10796–10808, 2011.

[157] Michael Eikerling. Water management in cathode catalyst layers of pem fuel cells: a structure-based model. *Journal of The Electrochemical Society*, 153(3): E58, 2006.

[158] Sabri Ergun. Fluid flow through packed columns. *Chem. Eng. Prog.*, 48:89–94, 1952.

[159] Bauyrzhan K Primkulov, Amir A Pahlavan, Xiaojing Fu, Benzhong Zhao, Christopher W MacMinn, and Ruben Juanes. Wettability and lenormand's diagram. *Journal of Fluid Mechanics*, 923, 2021.

[160] M-R Lee, H-Y Lee, S-D Yim, C-S Kim, Y-G Shul, A Kucernak, and D Shin. Effects of ionomer carbon ratio and ionomer dispersity on the performance and durability of meas. *Fuel cells*, 18(2):129–136, 2018.

[161] Yuxiu Liu, Chunxin Ji, Wenbin Gu, Daniel R Baker, Jacob Jorne, and Hubert A Gasteiger. Proton conduction in pem fuel cell cathodes: effects of electrode thickness and ionomer equivalent weight. *Journal of The Electrochemical Society*, 157(8):B1154, 2010.

[162] H Markötter, I Manke, Ph Krüger, Tobias Arlt, J Haussmann, M Klages, Heinrich Riesemeier, Ch Hartnig, J Scholta, and J Banhart. Investigation of 3d water transport paths in gas diffusion layers by combined in-situ synchrotron x-ray radiography and tomography. *Electrochemistry Communications*, 13(9): 1001–1004, 2011.

[163] Sang-Joon Lee, Seung-Gon Kim, Gu-Gon Park, and Chang-Soo Kim. Quantitative visualization of temporal water evolution in an operating polymer electrolyte fuel cell. *International journal of hydrogen energy*, 35(19):10457–10463, 2010.

[164] Curtis Marr and Xianguo Li. Composition and performance modelling of catalyst layer in a proton exchange membrane fuel cell. *Journal of Power Sources*, 77(1):17–27, 1999.

[165] Torsten Berning, DM Lu, and N Djilali. Three-dimensional computational analysis of transport phenomena in a pem fuel cell. *Journal of power sources*, 106 (1-2):284–294, 2002.

[166] AA Kulikovsky. Quasi-3d modeling of water transport in polymer electrolyte fuel cells. *Journal of the Electrochemical Society*, 150(11):A1432, 2003.

[167] Ugur Pasaogullari and Chao-Yang Wang. Two-phase modeling and flooding prediction of polymer electrolyte fuel cells. *Journal of the Electrochemical Society*, 152(2):A380, 2005.

[168] Dilip Natarajan and Trung Van Nguyen. A two-dimensional, two-phase, multicomponent, transient model for the cathode of a proton exchange membrane fuel cell using conventional gas distributors. *Journal of the Electrochemical Society*, 148(12):A1324, 2001.

[169] M Eikerling, AS Ioselevich, and AA Kornyshev. How good are the electrodes we use in pefc? *Fuel Cells*, 4(3):131–140, 2004.

[170] Ugur Pasaogullari and CY Wang. Liquid water transport in gas diffusion layer of polymer electrolyte fuel cells. *Journal of the electrochemical society*, 151(3): A399, 2004.

[171] Adam Z Weber, Robert M Darling, and John Newman. Modeling two-phase behavior in pefcs. *Journal of the Electrochemical Society*, 151(10):A1715, 2004.

[172] Makoto Uchida, Yuko Fukuoka, Yasushi Sugawara, Nobuo Eda, and Akira Ohta. Effects of microstructure of carbon support in the catalyst layer on the performance of polymer-electrolyte fuel cells. *Journal of the Electrochemical Society*, 143(7):2245, 1996.

[173] Lei Xing, Mohamed Mamlouk, and Keith Scott. A two dimensional agglomerate model for a proton exchange membrane fuel cell. *Energy*, 61:196–210, 2013.

[174] Lei Xing. An agglomerate model for pem fuel cells operated with non-precious carbon-based orr catalysts. *Chemical Engineering Science*, 179:198–213, 2018.

[175] Firat C Cetinbas, Rajesh K Ahluwalia, Nancy N Kariuki, and Deborah J Myers. Agglomerates in polymer electrolyte fuel cell electrodes: Part i. structural characterization. *Journal of The Electrochemical Society*, 165(13):F1051, 2018.

[176] Firat C Cetinbas and Rajesh K Ahluwalia. Agglomerates in polymer electrolyte fuel cell electrodes: Part ii. transport characterization. *Journal of The Electrochemical Society*, 165(13):F1059, 2018.

[177] Shian Li, Jinliang Yuan, Gongnan Xie, and Bengt Sundén. Effects of agglomerate model parameters on transport characterization and performance of pem fuel cells. *International Journal of Hydrogen Energy*, 43(17):8451–8463, 2018.

[178] Rakel Wreland Lindström, Katrin Kortsdottir, Maria Wesselmark, Alejandro Oyarce, Carina Lagergren, and Göran Lindbergh. Active area determination of porous pt electrodes used in polymer electrolyte fuel cells: Temperature and humidity effects. *Journal of the Electrochemical Society*, 157(12):B1795, 2010.

[179] EF Médici and JS Allen. *Physics of Fluids*, 23(12):122107, 2011.

[180] Reto Flückiger, Federica Marone, Marco Stampanoni, Alexander Wokaun, and Felix N Büchi. *Electrochimica Acta*, 56(5):2254–2262, 2011.

[181] Kyle J Lange, Pang-Chieh Sui, and Ned Djilali. *Journal of The Electrochemical Society*, 157(10):B1434–B1442, 2010.

[182] Firat C Cetinbas, Rajesh K Ahluwalia, Nancy Kariuki, Vincent De Andrade, Dash Fongalland, Linda Smith, Jonathan Sharman, Paulo Ferreira, Somaye Rasouli, and Deborah J Myers. *Journal of Power Sources*, 344:62–73, 2017.

[183] NA Siddique and Fuqiang Liu. *Electrochimica Acta*, 55(19):5357–5366, 2010.

[184] Yudai Ogata, Daisuke Kawaguchi, Norifumi L Yamada, and Keiji Tanaka. *ACS Macro Letters*, 2(10):856–859, 2013.

[185] Scott A Eastman, Sangcheol Kim, Kirt A Page, Brandon W Rowe, Shuhui Kang, Christopher L Soles, and Kevin G Yager. *Macromolecules*, 45(19):7920–7930, 2012.

[186] Puneet K Sinha and Chao-Yang Wang. *Electrochimica Acta*, 52(28):7936–7945, 2007.

[187] James Hinebaugh, Zachary Fishman, and A Bazylak. *Journal of The Electrochemical Society*, 157(11):B1651–B1657, 2010.

[188] Ugur Pasaogullari and Chao-Yang Wang. *Electrochimica Acta*, 49(25):4359–4369, 2004.

[189] Feng-Yuan Zhang, Suresh G Advani, Ajay K Prasad, Mary E Boggs, Shawn P Sullivan, and Thomas P Beebe Jr. *Electrochimica Acta*, 54(16):4025–4030, 2009.

[190] Partha P Mukherjee and Chao-Yang Wang. *Journal of the Electrochemical Society*, 153(5):A840–A849, 2006.

[191] Christoph Ziegler, Simon Thiele, and Roland Zengerle. *Journal of Power Sources*, 196(4):2094–2097, 2011.

[192] Alessandro Ferrara, Pierpaolo Polverino, and Cesare Pianese. Analytical calculation of electrolyte water content of a proton exchange membrane fuel cell for on-board modelling applications. *Journal of Power Sources*, 390:197–207, 2018.

[193] Miguel A Modestino, Ahmet Kusoglu, Alexander Hexemer, Adam Z Weber, and Rachel A Segalman. Controlling nafion structure and properties via wetting interactions. *Macromolecules*, 45(11):4681–4688, 2012.

[194] Sangcheol Kim, Joseph A Dura, Kirt A Page, Brandon W Rowe, Kevin G Yager, Hae-Jeong Lee, and Christopher L Soles. Surface-induced nanostructure and water transport of thin proton-conducting polymer films. *Macromolecules*, 46 (14):5630–5637, 2013.

[195] Miguel A Modestino, Devproshad K Paul, Shudipto Dishari, Stephanie A Petrina, Frances I Allen, Michael A Hickner, Kunal Karan, Rachel A Segalman, and Adam Z Weber. Self-assembly and transport limitations in confined nafion films. *Macromolecules*, 46(3):867–873, 2013.

[196] James T Hinatsu, Minoru Mizuhata, and Hiroyasu Takenaka. Water uptake of perfluorosulfonic acid membranes from liquid water and water vapor. *Journal of the Electrochemical Society*, 141(6):1493, 1994.

[197] Yohei Chikashige, Yoshiki Chikyu, Kenji Miyatake, and Masahiro Watanabe. Poly (arylene ether) ionomers containing sulfofluorenyl groups for fuel cell applications. *Macromolecules*, 38(16):7121–7126, 2005.

[198] Martin J Blunt and Harvey Scher. Pore-level modeling of wetting. *Physical Review E*, 52(6):6387, 1995.

[199] Viet Hoai Nguyen, Adrian P Sheppard, Mark A Knackstedt, and W Val Pinczewski. The effect of displacement rate on imbibition relative permeability and residual saturation. *Journal of Petroleum Science and Engineering*, 52 (1-4):54–70, 2006.

[200] George N Constantinides and Alkiviades C Payatakes. Effects of precursor wetting films in immiscible displacement through porous media. *Transport in porous media*, 38(3):291–317, 2000.

[201] MoC Leverett, WB Lewis, et al. Steady flow of gas-oil-water mixtures through unconsolidated sands. *Transactions of the AIME*, 142(01):107–116, 1941.

[202] Abdul Jamil Nazari, Ahmad Fahim Nasiry, and Shigeo Honma. Effect of fractional flow curves on the recovery of different types of oil in petroleum reservoirs. *Proc. Schl. Eng. Tokai Univ., Ser E*, 41:53–58, 2016.

[203] AS Odeh, BJ Dotson, et al. A method for reducing the rate effect on oil and water relative permeabilities calculated from dynamic displacement data. *Journal of petroleum technology*, 37(11):2–051, 1985.

[204] Serhat Akin, MR Demiral, et al. Effect of flow rate on imbibition three-phase relative permeabilities and capillary pressures. In *SPE Annual Technical Conference and Exhibition*. Society of Petroleum Engineers, 1997.

[205] GA Virnovsky, KO Vatne, SM Skjaeveland, A Lohne, et al. Implementation of multirate technique to measure relative permeabilities accounting. In *SPE Annual Technical Conference and Exhibition*. Society of Petroleum Engineers, 1998.

[206] YC Yortsos, AS Fokas, et al. An analytical solution for linear waterflood including the effects of capillary pressure. *Society of Petroleum Engineers Journal*, 23 (01):115–124, 1983.

[207] Chiu-Yen Kao, Alexander Kurganov, Zhuolin Qu, and Ying Wang. A fast explicit operator splitting method for modified buckley–leverett equations. *Journal of Scientific Computing*, 64(3):837–857, 2015.

[208] Hong Zhang and Paul Andries Zegeling. A numerical study of two-phase flow models with dynamic capillary pressure and hysteresis. *Transport in Porous Media*, 116(2):825–846, 2017.

[209] J-C Bacri, C Leygnac, and D Salin. Evidence of capillary hyperdiffusion in two-phase fluid flows. *Journal de Physique Lettres*, 46(11):467–473, 1985.

[210] Mingzhe Dong, Jun Zhou, et al. Characterization of waterflood saturation profile histories by the 'complete'capillary number. *Transport in porous media*, 31(2):213–237, 1998.

[211] KS Schmid and S Geiger. Universal scaling of spontaneous imbibition for arbitrary petrophysical properties: Water-wet and mixed-wet states and handy's conjecture. *Journal of Petroleum Science and Engineering*, 101:44–61, 2013.

[212] FJ Fayers, JW Sheldon, et al. The effect of capillary pressure and gravity on two-phase fluid flow in a porous medium. 1959.

[213] TS Ramakrishnan, D Wilkinson, and MM Dias. Effect of capillary pressure on the approach to residual saturation. *Transport in porous media*, 3(1):51–79, 1988.

[214] K Spayd and M Shearer. The buckley–leverett equation with dynamic capillary pressure. *SIAM Journal on Applied Mathematics*, 71(4):1088–1108, 2011.

[215] Ying Wang and Chiu-Yen Kao. Central schemes for the modified buckley–leverett equation. *Journal of Computational Science*, 4(1):12–23, 2013.

[216] Jincai Chang, Yanis C Yortsos, et al. Effect of capillary heterogeneity on buckley-leverett displacement. *SPE reservoir engineering*, 7(02):285–293, 1992.

[217] Harry A Deans. Method of determining fluid saturations in reservoirs, November 30 1971. US Patent 3,623,842.

[218] V Joekar-Niasar, F Doster, RT Armstrong, D Wildenschild, and MA Celia. Trapping and hysteresis in two-phase flow in porous media: A pore-network study. *Water Resources Research*, 49(7):4244–4256, 2013.

[219] Nilava Sen. Suratman number in bubble-to-slug flow pattern transition under microgravity. *Acta Astronautica*, 65(3-4):423–428, 2009.